

THE ISOBARIC MULTIPLY MASS EQUATION AND f_t VALUE OF THE
 $0^+ \rightarrow 0^+$ FERMI TRANSITION IN ^{32}Ar : TWO TESTS OF ISOSPIN
SYMMETRY BREAKING

A Dissertation

Submitted to the Graduate School
of the University of Notre Dame
in Partial Fulfillment of the Requirements
for the Degree of

Doctor of Philosophy

by

Smarajit Triambak

Alejandro García, Director

Umesh Garg, Director

Graduate Program in Physics

Notre Dame, Indiana

July 2007

© Copyright by
Smarajit Triambak
2007
All Rights Reserved

THE ISOBARIC MULTIPLY MASS EQUATION AND ft VALUE OF THE
 $0^+ \rightarrow 0^+$ FERMI TRANSITION IN ^{32}Ar : TWO TESTS OF ISOSPIN
SYMMETRY BREAKING

Abstract

by

Smarajit Triambak

This dissertation describes two high-precision measurements concerning isospin symmetry breaking in nuclei.

1. We determined, with unprecedented accuracy and precision, the excitation energy of the lowest $T = 2, J^\pi = 0^+$ state in ^{32}S using the $^{31}\text{P}(p, \gamma)$ reaction. This excitation energy, together with the ground state mass of ^{32}S , provides the most stringent test of the isobaric multiplet mass equation (IMME) for the $A = 32, T = 2$ multiplet. We observe a significant disagreement with the IMME and investigate the possibility of isospin mixing with nearby 0^+ levels to cause such an effect. In addition, as byproducts of this work, we present a precise determination of the relative γ -branches and an upper limit on the isospin violating branch from the lowest $T = 2$ state in ^{32}S .
2. We obtained the superallowed branch for the $0^+ \rightarrow 0^+$ Fermi decay of ^{32}Ar . This involved precise determinations of the beta-delayed proton and γ branches. The γ -ray detection efficiency calibration was done using precisely determined γ -ray yields from the daughter ^{32}Cl nucleus from another independent measurement using a fast tape-transport system at Texas

A&M University. This superallowed branch, along with previously determined half-life and Q_{EC} value measurements, provides the ft value for the decay. On comparison with the ft values of nine previously measured $T = 1 \rightarrow T = 1$ Fermi transitions, this provides a useful check of calculated isospin breaking corrections, which, in the case of ^{32}Ar , is ≈ 3 times larger than the nine measured cases. The calculated corrections for nuclear β decays play an important role in determining V_{ud} , the first element of the CKM matrix.

To my parents

CONTENTS

FIGURES	vi
TABLES	x
ACKNOWLEDGMENTS	xi
CHAPTER 1: INTRODUCTION	1
CHAPTER 2: THE ISOBARIC MULTIPLYET MASS EQUATION AND ITS RELEVANCE	4
2.1 Isospin in nuclear physics: charge independence of nuclear forces	4
2.2 Isospin symmetry violation, isobaric multiplets and the IMME	7
2.3 Experimental tests of the isobaric multiplet mass equation	10
CHAPTER 3: MASS OF THE LOWEST $T = 2$ STATE IN ^{32}S : TESTING THE IMME	13
3.1 Introduction	13
3.2 Experimental details	14
3.2.1 Target preparation	14
3.2.2 Apparatus	15
3.3 Energy calibration	18
3.4 Data Analysis	21
3.5 Systematic Effects	24
3.5.1 Gain Drifts	24
3.5.2 ADC nonlinearities	27
3.5.3 Doppler effects	27
3.5.4 The field-increment effect	31
3.5.5 Nonresonant background	34
3.6 Results and Discussion	34
3.6.1 Excitation energy of the $T = 2$ state	34
3.6.2 Relative gamma branches from the $T = 2$ state	37

3.6.3	Isospin violating γ decays	37
3.6.4	A test of the IMME	39
3.6.5	Isospin mixing with other 0^+ levels	42
3.7	Conclusions	43
CHAPTER 4: $0^+ \rightarrow 0^+$ FERMI DECAYS: PROBES TO TEST THE STANDARD MODEL		44
4.1	The standard electroweak model for quarks and leptons and CKM unitarity	44
4.2	Methods to extract the value of V_{ud}	48
4.2.1	Superallowed Fermi decays	48
4.2.1.1	The CVC hypothesis	50
4.2.1.2	Isospin symmetry breaking corrections	52
4.2.1.3	Radiative corrections	53
4.2.1.4	The corrected ft value	54
4.2.1.5	Experimental tests of the CVC hypothesis	55
4.2.1.6	Determination of V_{ud} from superallowed Fermi decays	56
4.2.2	Neutron and pion decays	56
4.3	Present status of CKM unitarity	57
4.4	The beta decay of ^{32}Ar	59
4.5	^{32}Ar superallowed decay: What needs to be known?	61
CHAPTER 5: DELAYED GAMMA YIELDS FROM ^{32}Cl BETA DECAY		63
5.1	Introduction	63
5.2	Experimental details	65
5.2.1	The MARS spectrometer: Beam production	65
5.2.2	The fast tape-transport system: Data acquisition	67
5.3	Data analysis	69
5.3.1	Efficiency Calibration	70
5.3.2	Determination of the γ -yields	73
5.4	Preliminary Results	75
5.5	Other systematic effects	77
CHAPTER 6: SUPERALLOWED BRANCH FOR ^{32}Ar BETA DECAY		79
6.1	Experimental Setup	79
6.2	Determination of the number of implanted ^{32}Ar ions	82
6.2.1	Ion identification	82
6.2.2	Number of implanted ions	86
6.3	Beta-delayed proton branches	88
6.3.1	Delayed proton spectra	88
6.3.2	Delayed proton transitions feeding the ^{31}S first excited state	92
6.3.3	Delayed proton branches following the superallowed decay	92

6.4	Beta-delayed γ branches	94
6.4.1	Gamma ray efficiencies	94
6.4.2	Gamma decays of the ^{32}Cl isobaric analog state	102
6.5	ft value of the superallowed decay	106
6.5.1	Widths and branches for γ -decays of the $T = 2$ state	110
CHAPTER 7: CONCLUSIONS AND FUTURE DIRECTIONS		112
APPENDIX A: DESCRIPTION OF THE LINESHAPE FUNCTION TO FIT GAMMA PEAKS		114
A.1	Normalization	117
A.2	General functional form	117
A.3	Binned Data	118
BIBLIOGRAPHY		119

FIGURES

3.1	Allowed γ decays of the lowest $T = 2$ state in ^{32}S	14
3.2	Target ladder with water cooling. Dimensions are in inches	16
3.3	Bellows and flange arrangement for target ladder. Dimensions are in inches	17
3.4	Schematic of electronics setup. Spec Amp = Spectroscopy Amplifier, TFA = Timing Filter Amplifier	18
3.5	Top view of the experimental setup used for the $^{31}\text{P}(p, \gamma)$ data at $\theta_\gamma = 90^\circ$	19
3.6	Top view of the experimental setup used for the $^{31}\text{P}(p, \gamma)$ data at $\theta_\gamma = 0^\circ$	19
3.7	$^{31}\text{P}(p, \gamma)$ spectrum from the 0° experiment. The ^{32}S lines and some ^{56}Co calibration peaks are labeled. The 9.8 MeV γ ray is mainly from direct capture.	20
3.8	Top view of the experimental setup for the $^{35}\text{Cl}(n, \gamma)$ calibration used in the $\theta_\gamma = \pm 90^\circ$ measurement.	21
3.9	Calibration lines with detector positioned at 90° to the beam.	22
3.10	Line-shape of γ peak. The contribution of each parameter is shown.	23
3.11	Fits to the most intense de-excitation gamma-rays from the $T = 2$ state.	24
3.12	Centroid of the 2598 keV ^{56}Co γ peak as a function of time.	25
3.13	Gain shift correction applied to the data. The left panel shows the fit before correction, with $\chi^2/\nu = 3.99$. The right panel shows the data the corresponding fit after correction, with a much improved χ^2/ν of 1.09.	25
3.14	Nonlinearity of the ADC. The points show centroids of $^{35}\text{Cl}(n, \gamma)$ and ^{56}Co calibration lines. Pronounced differences are seen between the observed positions and a linear fit to the region between 2015 keV and 8578 keV.	26

3.15	Detector geometry used for simulations. The dimensions of the crystal are obtained from the manufacturers. We make conservative estimates on the uncertainties.	28
3.16	Shifts in apparent γ -ray energies with changes in the incident γ -ray angle. The y-axis shows the difference in the inferred Doppler-shift-corrected γ energies from $^{35}\text{Cl}(n, \gamma)$ at two extreme angles (incident along the axis of the co-axial detector and approximately normal to the detector axis).	32
3.17	Energies of the 3.9 and 8.1 MeV γ peaks versus proton energy in the lab frame. For comparison the γ_1 data is shown (which corresponds to transitions to the first excited state at 2.2 MeV). The γ_1 data shows a non-resonant behavior as expected.	33
3.18	Top panel: Excitation function of 3922-keV γ yield. Bottom panel: Excitation function of γ_1 yield (this includes the single escape peak for additional statistics). The continuous line shows the upper limit described in the text.	38
3.19	Difference between measured mass excesses and IMME fit for the $A = 32, T = 2$ quintet in keV.	41
4.1	The experimental data needed to measure the ft value for a super-allowed transition	50
4.2	Corrected ft values for the most precisely measured $T = 1$ super-allowed beta emitters.	55
4.3	V_{ud} from the three different methods. The contribution of the uncertainties are shown.	58
4.4	Predicted coulomb corrections for a number of superallowed decays using the Hartree Fock calculations of Ref. [51]	60
4.5	Simplified decay scheme of ^{32}Ar . The delayed proton emission and some of the levels that γ decay are shown.	62
5.1	Decay scheme of ^{32}Cl . The beta branches are from Ref. [66].	64
5.2	Schematic layout of the Cyclotron Institute laboratory.	65
5.3	Schematic layout of the MARS recoil spectrometer.	66
5.4	Ion identification using the first strip detector. The only significant contaminant is ^{30}S	67
5.5	The fast tape-transport system at TAMU for precision measurements.	68
5.6	Delayed γ -ray spectrum following ^{32}Cl decay in coincidence with β particles.	69

5.7	γ -ray detection efficiencies and the corresponding polynomial fit. . .	71
5.8	Decay scheme of the ^{30}S contaminant.	73
6.1	Simplified decay scheme of ^{32}Ar	80
6.2	Top plus downstream views of the detector setup. The top view does not show the top and bottom Ge detectors.	81
6.3	E_1 vs. TOF_1 spectrum from a single run. Top: 3d spectrum where the ^{32}Ar group has been truncated to show the other groups more clearly. Bottom: vertical projection showing Region 3.1 (<i>good</i> region), which contains the main ^{32}Ar group, and Region 3.2 (<i>buffer</i> region), which contained mostly ambiguous ions.	83
6.4	E_3 vs. E_2 spectrum of events shown in Figure 6.3. Region 4.1 was defined to show that these events arise from a high-energy tail of the beam (see text and Figure 6.6) and used to define Region 6.1; the larger Region 4.2 is used in conjunction with Region 6.1 to ensure all high-energy tail events are labelled <i>ambiguous</i>	84
6.5	$E3$ vs. $E2$ showing only events on Region 3.1 in Figure 6.3. Region 5.1 contains <i>good</i> ^{32}Ar ions and contains 61 times more events than Region 5.2. Region 5.2 is exclusive of Region 5.1 and contains <i>ambiguous</i> ions.	84
6.6	E_1 versus TOF_1 spectrum of events in Region 4.1 of Figure 6.4. Once defined, events that were in both Region 6.1 and Region 4.2 were labelled <i>ambiguous</i> to avoid high-energy tails in the beam profile.	85
6.7	Left panel: singles delayed proton spectrum in D_3 (histogram) along with the corresponding R-matrix fit (solid line). The long high-energy tails are due to β summing. The filled curve corresponds to proton emission following the superallowed transition and the dashed is the β background. Right panel: same as the left, but gated by $E_\gamma = 1249$ keV. In this case, proton emission following the superallowed transition is peaked at ≈ 2.3 MeV.	89
6.8	ISOLDE data and its corresponding R-matrix fit. This spectrum was taken by implanting 60 keV ^{32}Ar ions into a $20 \mu\text{g}/\text{cm}^2$ carbon foil and observing the beta-delayed proton groups with cooled PIN diodes. The detection setup was immersed in a 3.5 Tesla magnetic field that prevented the β s from reaching the detectors and summing with protons.	91
6.9	Spectrum of γ -rays in coincidence with a β signal in D_2 , D_3 , or D_4 . Lines from ^{32}Ar decay are marked with a “ \star ”. The remaining labelled lines are from ^{32}Cl decay.	95

6.10	Stack of Si detectors.	97
6.11	Geometry file for one of the clovers.	97
6.12	Geometry of the 120% detector.	98
6.13	Geometry file of the detector array used for simulations. The Si detectors are surrounded by the beamline. The aluminium endcaps for two side clovers are not shown in the figure, but are used in the simulations.	99
6.14	The absolute $\epsilon_\gamma\epsilon_\beta$ from ^{32}Cl decays and the PENELOPE efficiency curves for each detector.	103
6.15	Spectrum of γ s in coincidence with 3878-keV γ -rays and a β signal in D ₂ , D ₃ or D ₄ . All of the peaks except for the ones at 2230 keV and 511 keV correspond to the expected γ cascades following the 3878-keV γ ray. Bottom panel: same as above, but with the coincidence gate shifted down by 8 keV. This shows that the 2230-keV γ comes mainly from coincidences with the Compton continuum of the 4770-keV γ ray in ^{32}S	104
6.16	The region of interest where the γ ray corresponding to the decay from the $T = 2$ state to the ground state should appear at $E_\gamma = 5046$ keV. The main 5038-keV peak is the first escape from the 5550-keV γ ray from ^{32}Cl	105
6.17	Residuals of linear fits. The energy calibration is largely linear for all detectors from 1 MeV to 6 MeV.	107
6.18	The 2836 and the 2839 keV γ -ray doublet. The insets show the proton spectrum gated with GATE 1 (which has a peak corresponding to 610-keV protons) and GATE 2 respectively. This shows that the 2836-keV component is followed by proton emission whereas the 2839-keV γ is not.	108

TABLES

3.1	PREDICTED DOPPLER SHIFTS FROM MONTE CARLO SIMULATIONS	29
3.2	LEVEL ENERGIES AND DOPPLER-CORRECTED GAMMA RAY ENERGIES FROM ^{32}S	35
3.3	GAMMA-RAY ENERGIES FOR CASCADES FROM THE LOWEST $T = 2$ STATE IN ^{32}S	36
3.4	RELATIVE GAMMA BRANCHES (IN %) FROM THE LOWEST $A = 32$ $T = 2$ STATES. EXCITATION ENERGIES ARE IN KEV	38
3.5	COMPARISON OF MEASURED MASS EXCESSES OF THE LOWEST $T = 2$, $A = 32$ QUINTET WITH IMME FIT	40
4.1	THE THREE GENERATION STANDARD MODEL OF QUARKS AND LEPTONS	45
5.1	GAMMA-RAY DETECTION EFFICIENCIES AT 15.1 CM (FROM REF. [70].)	71
5.2	GAMMA-RAY INTENSITIES FROM THE BETA-DECAY OF ^{32}Cl	76
5.3	BETA BRANCHES FROM ^{32}Cl DECAY	78
6.1	PROTON GROUPS IN COINCIDENCE WITH A 1249 KEV GAMMA RAY	93
6.2	SUMMING CORRECTIONS AND SIMULATED EFFICIENCIES	100
6.3	SUMMING CORRECTIONS AND SIMULATED EFFICIENCIES	101
6.4	ABSOLUTE $\beta\gamma$ BRANCHES FROM THE LOWEST $T = 2$ STATE IN ^{32}Cl	109
6.5	RELATIVE γ BRANCHES FROM THE LOWEST $T = 2$ STATES IN THE $A = 32$ MULTIPLY	111

ACKNOWLEDGMENTS

This thesis is a result of the work of many people with whom I have been fortunate to associate with during the last six years. First and foremost, I am forever indebted to my thesis advisor, Alejandro García, for being an incredibly wonderful teacher, mentor and friend. Over the years I have benefited greatly from working with him and learned a lot from his knowledge and intelligent suggestions. His enthusiasm, dedication, willingness to teach and patience were a constant source of inspiration throughout my graduate student career.

I am grateful to Dan Melconian for being a great friend and collaborator, and for being extremely helpful in various experiments that we were mutually involved in. Dan's help in the analysis of the data presented in this dissertation is one of the main reasons this work could be completed on time. I would like to thank him for always being available when I needed him, and for teaching me useful techniques in data reduction and Monte Carlo simulations.

I would like to thank Umesh Garg for offering to be my co-advisor during my absence from the University of Notre Dame. His wonderful hospitality and warmth was a constant source of encouragement during the cold winters at South Bend. I was greatly influenced by discussions with him about my research work and am grateful that he constantly motivated me to do better than what I thought were my capabilities.

This dissertation is a result of endless discussions with many other collab-

orators. I benefited greatly from stimulating discussions with Eric Adelberger and John Hardy who were more than willing to share their vast experience and knowledge about precision measurements and weak interactions with me.

Eric's valuable suggestions and interesting ideas during the course of the $^{31}\text{P}(p, \gamma)$ experiment and the subsequent analysis of the data were rewarding for me at many levels. His critical analysis of the paper that followed taught me important writing skills that were helpful in writing this dissertation. The ^{32}Cl beta-decay measurement at Texas A&M University would not have been possible without John's help and cooperation. John's insightful comments, valuable advice and continual presence during the experiment guided us towards a successful run at the first attempt.

In addition, for the $^{31}\text{P}(p, \gamma)$ experiment, I was fortunate to obtain extremely useful tips and suggestions from Kurt Snover and help from Seth Hoedl, Sky Sjue and Anne Sallaska during the whole experimental procedure and data analysis. For the Texas A&M University experiment, I would like to thank in particular Victor Iacob for being around at all times to help with the experiment. I am also thankful to Bob Tribble, Livius Trache and Gabriel Tabacaru, who worked really hard to provide us with a clean radioactive ion-beam and patiently answered all my questions about the MARS spectrometer, and, Cristina Bordeanu and Ninel Nica for spending more than a reasonable amount of time in the experimental shifts to ensure smooth data acquisition.

The experiments described in this dissertation could not be completed without the help of many other people. At the University of Washington, Greg Harper and Doug Will taught me a lot about the use of the tandem Van de Graaf accelerator and ion sources and Dick Seymour was forever present and ready to help with

computer issues. Hank Simons, Jim Elms and David Hyde patiently worked with me on machining various parts of the target ladder and chamber while teaching me the nuances of precision design and machining.

I would like to extend my thanks to Jennifer Maddox, Shari Herman, and Sandra Trobaugh at the University of Notre Dame and Barbara Fulton, Kate Higgins, and Debra Nastaj at the University of Washington for being incredibly helpful on the administrative front. Their speedy and efficient handling of all my paperwork ensured me a smooth ride through graduate school.

I am grateful to my numerous friends and well wishers who have been at my side during both good and bad times over the past few years, especially Leah Koskimaki for her caring support during the last phase of my PhD and for taking the time to diligently read through my entire dissertation and offer useful suggestions to make the language more coherent.

Finally, I can't thank my parents enough for all their support and love throughout my life. Their immense faith in my abilities was the main driving force behind everything. I dedicate this work to them and everybody else in my family, for all their love and inspiration.

CHAPTER 1

INTRODUCTION

*We cannot help being thirsty,
moving toward the voice of water....*
- Jalal ad-Din Rumi

The Standard Model of particle physics describes nature at the most fundamental level. This Standard Model is an elegant theory that describes elementary particles and their interactions in terms of the strong, electromagnetic and weak forces. It comprises of the standard electroweak theory, which unifies the electromagnetic and the weak interaction, and of quantum chromodynamics, which is the theory of strong interactions. Within the Standard Model, the elementary particles that constitute matter are made up of fermions, and the interactions between the fermions are mediated by bosons. Although the Standard Model has been extremely successful in reproducing experimental results and vice-versa (such as the masses of the W bosons and the existence of top quark), there is reason to believe that it is not a complete theory of fundamental interactions. Several questions remain unanswered. For example, the model contains approximately 19 free parameters (such as the masses of the elementary particles and the values of the coupling constants) that cannot be independently calculated. These values need to be experimentally measured and then incorporated into the model. It also does not answer other important questions such as why there exist three generations of

fermions or why there is more matter than antimatter in the universe. These are but a few questions that lead us to believe that there exists a more fundamental theory that offers a complete description of nature.

One way to investigate physics beyond the Standard Model is by careful measurements of beta-decay observables, which are supposedly governed by the theory of electroweak interactions. The standard electroweak theory assumes the validity of various fundamental symmetries, such that the violation of any of these symmetries would constitute a signal of new physics. In this dissertation, we describe two measurements that are related to such Standard Model tests. In these measurements, the atomic nucleus is used as a probe to search for and set improved constraints on new physics.

The first measurement described in this dissertation stringently tests the isobaric multiplet mass equation (IMME) for the $A = 32$ multiplet. Although this is not directly related to testing the Standard Model, it addresses important nuclear physics issues related to observables and parameters that are important for Standard Model tests. For example, the IMME has been previously used to determine configuration mixing corrections and beta endpoint energies in the absence of experimental data, which are directly related to tests of CKM unitarity and searches for scalar interactions in weak processes.

The second measurement described is the determination of the ft value for the $0^+ \rightarrow 0^+$ Fermi decay of ^{32}Ar from the superallowed decay branch. This measured ft value provides a useful check of theoretically calculated corrections that are important for tests of CKM unitarity and the conserved vector current hypothesis.

Both the measurements described are related to isospin symmetry breaking,

which occurs due to charge-dependent interactions within nuclei. A thorough understanding of such effects is important in the study of nuclear beta decays to probe the fundamental properties of the electoweak interaction.

CHAPTER 2

THE ISOBARIC MULTIPLY MASS EQUATION AND ITS RELEVANCE

2.1 Isospin in nuclear physics: charge independence of nuclear forces

The concept of isospin in nuclear physics was first introduced by Heisenberg in 1932 [1] based on observations of clustering of stable nuclei about the $N \approx Z$ line. He noted that such an effect indicates an underlying symmetry of the strong interaction. Furthermore, he made the hypothesis that the neutron and the proton can be treated as two states of the same particle, called the nucleon. A new quantum number called isospin was thus assigned to the nucleon on the basis of its charge. Since the nucleon was a two-state system, analogous to a spin-1/2 particle, the isospin assigned to each nucleon was 1/2, with two possible projections in *isospin space*. It soon became apparent, with the investigation of proton-proton (pp) and neutron-proton (np) interaction strengths via low energy scattering experiments, that the nucleon-nucleon interaction was approximately *charge independent*. These experiments determined that, if the ranges are taken to be identical, after Coulomb corrections are taken into account, there exists rough agreement between the pp and np forces [2]. Furthermore, the study of mirror nuclei ¹ (such as ${}^3\text{H}$ and ${}^3\text{He}$) showed that these nuclei had approximately the same masses after correcting for the electrostatic energy [3]. Such similarity strongly

¹Mirror nuclei are pairs of nuclei having the same A such that either nucleus can be obtained from the other by transforming all the neutrons of one into protons and all protons into neutrons.

indicated identical nn and pp interaction strengths and further corroborated the charge independence of the nucleon-nucleon interaction.

The charge independence of the nuclear force is analogous to the spin independence of the Coulomb force in atoms. For a spin-1/2 particle, spin independence implies that the Hamiltonian is invariant under unitary transformations in two dimensions. Such transformations are described in the group theoretical representation by the $SU(2)$ rotation group, where the angular momentum operator is the generator of the group. Rotational invariance in 3-dimensional space implies conservation of total angular momentum and vice-versa.

In a formalism identical to angular momentum, the nucleon wavefunction can be represented by a two-component spinor. On separating the isospin part from the space-spin part of the wavefunction, we define the proton and the neutron basis vectors in *isospin space*

$$|\chi_p\rangle = \begin{pmatrix} 1 \\ 0 \end{pmatrix} \quad |\chi_n\rangle = \begin{pmatrix} 0 \\ 1 \end{pmatrix} \quad (2.1)$$

and the Pauli isospin matrices

$$\mathbb{1} = \begin{pmatrix} 1 & 0 \\ 0 & 1 \end{pmatrix} \quad \tau_1 = \begin{pmatrix} 0 & 1 \\ 1 & 0 \end{pmatrix} \quad \tau_2 = \begin{pmatrix} 0 & -i \\ i & 0 \end{pmatrix} \quad \tau_3 = \begin{pmatrix} 1 & 0 \\ 0 & -1 \end{pmatrix} \quad (2.2)$$

which follow the usual commutation relations

$$[\tau_i, \tau_j] = 2i\epsilon_{ijk}\tau_k . \quad (2.3)$$

It follows from above, that if there exists a charge operator Q which follows the

eigenvalue equation

$$Q|\chi\rangle = q|\chi\rangle \quad (2.4)$$

with $q = 0$ if $|\chi\rangle = |\chi_n\rangle$ and $q = e$ if $|\chi\rangle = |\chi_p\rangle$, then this operator can be obtained in terms of the Pauli matrices as

$$Q = e \left(\frac{\mathbb{1} + \tau_3}{2} \right). \quad (2.5)$$

The eigenvalue of this operator gives the charge of the nucleon in units of e by definition.

The other two components of $\boldsymbol{\tau}$ (τ_1 and τ_2) are not related to any observables. However, it is customary to define the isospin *raising* and *lowering* operators in terms of their linear combinations, $\tau^{(\pm)} = \frac{1}{2}(\tau_1 \pm i\tau_2)$, which convert neutrons into protons and vice-versa.

The arguments stated above can be generalized for a system of A nucleons, such that the total nuclear isospin \mathbf{T} and its component T_3 are

$$\mathbf{T} = \frac{1}{2} \sum_{i=1}^A \boldsymbol{\tau}_i \quad T_3 = \frac{1}{2} \sum_{i=1}^A \tau_{i3} . \quad (2.6)$$

From this, it follows that the charge operator for the nucleus satisfies the eigenvalue equation

$$Q_N|\psi_N\rangle = \sum_{i=1}^A Q_i|\psi_N\rangle = e(A/2 + T_3)|\psi_N\rangle = Ze|\psi_N\rangle . \quad (2.7)$$

The arguments stated above have two direct implications:

1. The third component of nuclear isospin can be written as

$$T_3 = \left(\frac{Z - N}{2} \right). \quad (2.8)$$

2. The conservation of electric charge demands that T_3 has to be a conserved quantity, i.e.

$$[H, T_3] = 0. \quad (2.9)$$

2.2 Isospin symmetry violation, isobaric multiplets and the IMME

The approximate charge independence of the strong nuclear force implies that the nucleon wavefunction is invariant under the application of a rotation operator in isospin space. In a manner analogous to angular momentum, such a rotation can be represented as a continuous unitary transformation, where the unitary operator that corresponds to a finite rotation of angle ϕ about $\hat{\mathbf{n}}$ in isospin space is given by

$$U_{\hat{\mathbf{n}}}(\phi) = \exp(-i\phi\hat{\mathbf{n}} \cdot \mathbf{T}) , \quad (2.10)$$

\mathbf{T} being the generator of the rotation group. This $SU(2)$ rotation group has single-valued irreducible representations of dimension $2T + 1$. Therefore, for a particle moving in a central hadronic field with total isospin T , there exist $2T + 1$ degenerate states that can be characterized by projections of the total isospin onto an arbitrary axis. This leads to the conclusion that isospin is a conserved quantity in the presence of purely hadronic forces.

However, it is known that isospin is not an exact symmetry. The isotropy of isospin space (neglecting the mass difference between u and d quarks) is broken by the electromagnetic interaction. Such charge-dependent couplings break the $(2T + 1)$ -fold degeneracy (akin to the Zeeman and the Stark effects in atomic physics) and lead to the existence of *isospin multiplets*. The members of a given multiplet are labelled by T_3 (projections on the \hat{z} axis by definition) on the basis of electric charge. As in the case with angular momentum, T_3 takes values between

$-T$ and $+T$. In a simple model describing isospin multiplets, the level schemes of each nucleus would therefore be shifted by the Coulomb energy and the neutron-proton mass difference. What follows below is the description of such a model, namely the isobaric multiplet mass equation (denoted as IMME henceforth), that relates the masses of the members of an isospin multiplet. The mass difference between u and d quarks is neglected throughout.

The IMME was first proposed by Wigner at a conference proceedings [4] and later derived with more mathematical rigor by Weinberg and Treiman [5]. Since electromagnetic effects are characterized by the fine structure constant, isospin is conserved sufficiently to the lowest order in e^2 . This allows for first-order perturbation theory to work well in the description of isospin symmetry violation by electromagnetic effects.

A two-body charge-dependent interaction can be added to the isospin conserving hadronic Hamiltonian as a perturbation such that,

$$H = H_{CI} + H_{CD} , \tag{2.11}$$

where the indices refer to *charge independent* and *charge dependent* respectively. In its most general form, at tree-level, H_{CD} can be written in terms of the Pauli matrices as

$$H_{CD} = \sum_{i < j} (\alpha \tau_3(i) + \beta)(\alpha \tau_3(j) + \beta) f(r_{ij}) , \tag{2.12}$$

where α and β are constants that depend on the nature of the charge-dependent interaction, and $f(r_{ij})$ is a function dependent on the relative separation between two interacting nucleons, which are labelled by the indices i and j . This charge

dependent perturbation can be written as

$$\begin{aligned}
f(r_{ij}) \left(\sum_{i<j} \left[\beta^2 + \frac{\alpha^2}{3} \boldsymbol{\tau}(i) \cdot \boldsymbol{\tau}(j) \right] + \sum_{i<j} \alpha\beta [\tau_3(i) + \tau_3(j)] \right) \\
+ f(r_{ij}) \left(\sum_{i<j} \frac{\alpha^2}{3} [3\tau_3(i)\tau_3(j) - \boldsymbol{\tau}(i) \cdot \boldsymbol{\tau}(j)] \right) . \quad (2.13)
\end{aligned}$$

The three sums in Eq. (2.13) transform as tensors of rank 0, 1, and 2 respectively in isospin space. Thus, the expectation value of the total Hamiltonian can be expressed as

$$\begin{aligned}
\langle \xi TT_3 | H_{CI} + H_{CD} | \xi TT_3 \rangle = E_{\xi,T} + \langle \xi TT_3 | H_{CD}^{(0)} | \xi TT_3 \rangle \\
+ \langle \xi TT_3 | H_{CD}^{(1)} | \xi TT_3 \rangle + \langle \xi TT_3 | H_{CD}^{(2)} | \xi TT_3 \rangle . \quad (2.14)
\end{aligned}$$

Here $E_{\xi,T}$ are the eigenvalues of H_{CI} , ξ represents all the other quantum numbers necessary for a unique representation of the eigenstate $|\xi TT_3\rangle$, and $H_{CD}^{(n)}$ transforms as an isotensor of rank n .

The matrix elements of irreducible tensor operators (such as the ones in Eq. (2.14)) can be expressed as the product of *reduced matrix elements* and Clebsch-Gordan coefficients (that purely depend on the geometrical properties of the tensor and the states involved) using the Wigner-Eckart theorem [6]. Application of the Wigner-Eckart theorem to Eq. (2.14) yields

$$\begin{aligned}
\langle \xi TT_3 | H_{CI} + H_{CD} | \xi TT_3 \rangle = E_{\xi,T} + \langle \xi T || H_{CD}^{(0)} || \xi T \rangle \\
+ \frac{T_3}{[T(T+1)]^{1/2}} \langle \xi T || H_{CD}^{(1)} || \xi T \rangle \\
+ \frac{3T_3^2 - T(T+1)}{[(2T-1)T(T+1)(2T+3)]^{1/2}} \langle \xi T || H_{CD}^{(2)} || \xi T \rangle . \quad (2.15)
\end{aligned}$$

This expression is constituted of energies expressed in terms of the reduced matrix elements and coefficients involving T and T_3^2 . Therefore, the relation between the masses of a given isospin multiplet can be written to the first-order as

$$M(\xi, T, T_3) = a(\xi, T) + b(\xi, T)T_3 + c(\xi, T)T_3^2, \quad (2.16)$$

which is the isobaric multiplet mass equation (IMME). The coefficients of the IMME are mainly related to the Coulomb displacement energies between isobaric analog states, with small contributions from other charge dependent effects (such as the electromagnetic spin-orbit interaction) [7]. Deviations from Eq.(2.16), such as the requirement of a non-vanishing $d(\xi, T)T_3^3$ term could indicate one of many scenarios: isospin mixing with nearby states of different isospin, the presence of many-body charge-dependent forces, or the need for a higher order perturbation theory calculation.

2.3 Experimental tests of the isobaric multiplet mass equation

Although there is no fundamental principle that forbids violation of Eq. (2.16), theoretical calculations indicate that the IMME should hold down to $|d| \lesssim 1$ keV for multiplets that do not have isospin-allowed strong decays [8, 9]. Over the years many experimental tests have been performed looking for potential deviations from the IMME (for example, an additional cubic term) [10, 11] that show remarkable agreement with the model. The only significant deviations are found in light nuclei with unbound states and smaller Coulomb barriers, which lead to non-perturbative effects. For example, the lowest $A = 9$, $T = 3/2$ quartet requires a significantly large cubic term and has been explained as a combination of higher order charge-dependent interactions and expansion of the nuclear wavefunction

due to Coulomb effects [9]. The $A = 8, T = 2$ multiplet was the only known quintet that required either an additional dT_3^3 term or an eT_3^4 term or both for a satisfactory fit.

The success of the IMME makes it a useful tool to predict masses and level-energies for cases where experimental data is lacking. For example, it has been used to map the proton drip line over a wide range, determine the rp -process path in stellar nucleosynthesis, identify candidates for diproton emission [12], and constrain models for the configuration mixing correction factor needed for tests of CKM unitarity [13]. In addition, the IMME was used to determine the β end-point energy from the decay of ^{32}Ar which is a requirement for analyzing the Doppler broadening of β -delayed groups from ^{32}Ar . The shape of the proton spectrum provides information about the $\beta - \nu$ correlation, which sets constraints on scalar contributions to the weak interaction [14].

A recent precision measurement of the ^{33}Ar mass using a Penning trap mass spectrometer at ISOLDE indicated breakdown of the IMME for the $A = 33, T = 3/2$ quartet, where an unexpectedly large cubic term was required to fit the members of the quartet ($d = -2.95 \pm 0.90$ keV) [15]. It was later realized that the problem originated due to an incorrect determination of the mass of the lowest $T = 3/2$ state in ^{33}Cl [16]. The masses of the members of the lowest $A = 33, T = 3/2$ quartet are now known with high precision and are in excellent agreement with IMME predictions [17]. Another recent measurement of the mass of ^{32}Ar to 1.8 keV [18] made the lowest $A = 32, T = 2$ quintet the most precisely measured quintet to date [11]. In spite of excellent agreement with the IMME, the mass of the $T_3 = 0$ member of this multiplet (^{32}S) was on a weak footing. A $^{31}\text{P}(p, \alpha)$ resonance study [19] gave an excitation energy of 12049 ± 2 keV for

the lowest $T = 2$ state. An earlier $^{31}\text{P}(p, \gamma)$ study [20] obtained a significantly different result, i.e. an excitation energy of 12045.0 ± 0.4 keV, but no details were provided about the difficult task of determining the excitation energy to such a high precision. This provides the motivation to remeasure the excitation energy of the lowest $T = 2$ state in ^{32}S with high accuracy and precision. The following chapter describes the experiment involved to remeasure the mass of the lowest $T = 2$ state in ^{32}S .

CHAPTER 3

MASS OF THE LOWEST $T = 2$ STATE IN ^{32}S : TESTING THE IMME

In the previous chapter we have described the motivation for determining the excitation energy of the lowest $T = 2$ state in ^{32}S . In this chapter we present details and the results of our measurement.

3.1 Introduction

Before this work, the lowest $J^\pi, T = 0^+, 2$ state in ^{32}S had been observed using the isospin-forbidden $^{31}\text{P}(p, \gamma)$ resonance reaction at $E_p = 3283(3)$ keV [21]. The total width of the state is known to be $\Gamma = 40(15)$ eV [22]. Although the state is mainly unbound to isospin-forbidden proton and α emission [19], it also de-excites to the ground state via γ transitions, with $\Gamma_\gamma \approx 2$ eV. Figure 3.1 shows the allowed γ transitions from the $J^\pi, T = 0^+, 2$ state in ^{32}S . This level mainly decays via a $M1$ transition to the $J^\pi, T = 1^+, 1$ state at ≈ 8 MeV, which in turn decays to the ground state with a high branching ratio [21]. The excitation energies of the states in ^{32}S can therefore be obtained by precise determination of the γ -ray energies from ^{32}S via $^{31}\text{P}(p, \gamma)$.

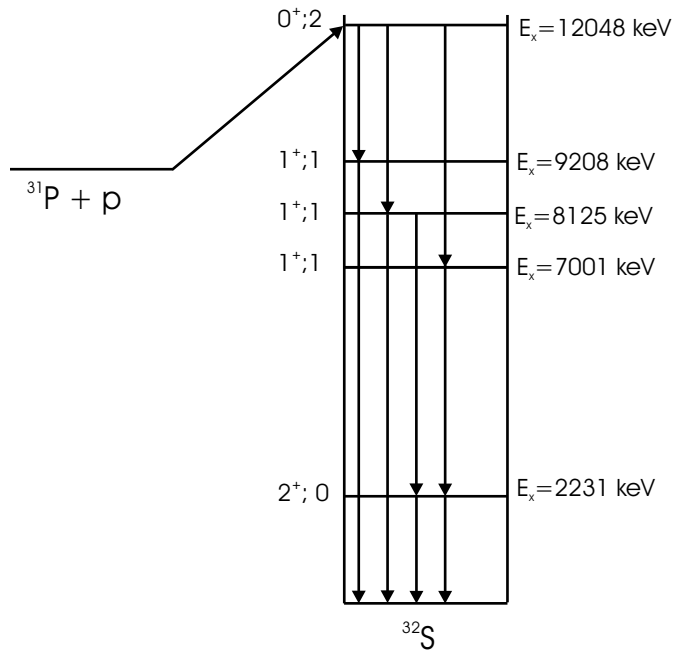


Figure 3.1. Allowed γ decays of the lowest $T = 2$ state in ^{32}S .

3.2 Experimental details

3.2.1 Target preparation

The ^{31}P target was produced by ion-implantation. A $3\ \mu\text{A}$ beam of ^{31}P ions at $\approx 90\ \text{keV}$ was produced using a sputter ion source and implanted on an ultra-pure, 0.5 mm thick Tantalum backing. The beam was collimated and rastered using computer-controlled magnetic steerers to produce a uniform target. Calculations using TRIM [23] indicated that the implantation profile had a FWHM of $\approx 700\ \text{\AA}$ at 90 keV incident energy. A total of $55\ \mu\text{Ah}$ ^{31}P ions were deposited, yielding a ratio of $\approx 3 : 1$ Phosphorus to Tantalum atoms in the target. This target had a measured energy loss of $\approx 4\ \text{keV}$ for 3 MeV protons.

3.2.2 Apparatus

The $^{31}\text{P}(p, \gamma)$ measurement was performed with the University of Washington FN tandem accelerator, operating such that the ion source was positioned at the terminal. The target chamber was a ISO-NW100 tee, with three glass viewports for alignment purposes. The target ladder was designed to allow for direct water-cooling of the target backings. An adjustable bellows arrangement provided vertical degree of freedom to the ladder, such that three targets could be used at anytime during the experiment, without breaking vacuum. The target ladder is shown in Figure 3.2 and the bellows and flange arrangement is shown in Figure 3.3. Gamma-rays were registered with two 50% HPGe (GMX) detectors whose signals were processed by temperature-controlled electronics to minimize gain-drifts. Figure 3.4 shows a simplified block diagram of the electronics setup.

The detectors were mounted on platforms that could rotate about the vertical axis at the center of the chamber and were aligned using mechanical alignment jigs. Two independent measurements were done at different times by impinging the ^{31}P target with an $\approx 6 \mu\text{A}$, 3.285 MeV proton beam. In the first measurement, data were obtained with two HPGe detectors located ≈ 60 cm from the center of the chamber, at $\pm 90^\circ$ to the beam where the Doppler shift is minimal. This is shown in Figure 3.5. The energy calibration was based on a ^{56}Co source and $^{35}\text{Cl}(n, \gamma)$ capture radiation. In the second measurement, one detector was aligned at 0° and positioned 10.3 cm from the target as shown in Figure 3.6. Although Doppler shifts are maximum at $\theta_\gamma = 0^\circ$, the sensitivity to detector misalignment was minimal. The energy calibration for this measurement was based on ^{56}Co and $^{27}\text{Al}(p, \gamma)$ radiation. Figure 3.7 shows a gamma spectrum from the 0 degree experiment.

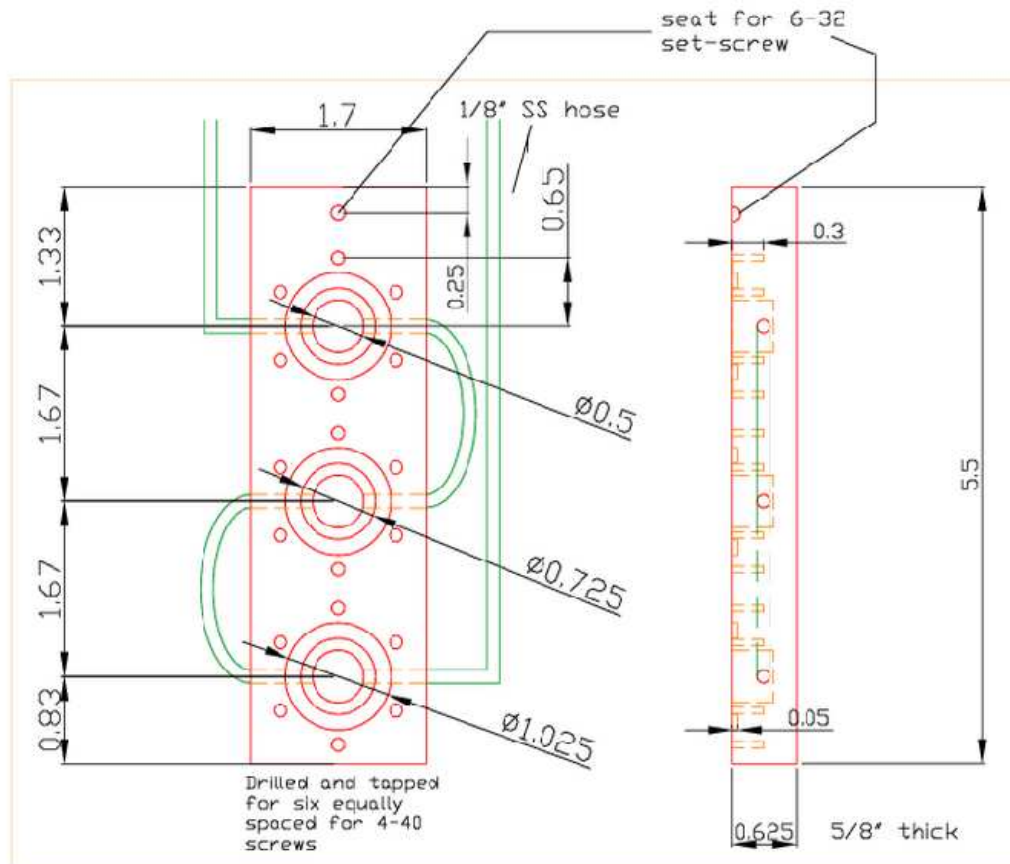


Figure 3.2. Target ladder with water cooling. Dimensions are in inches

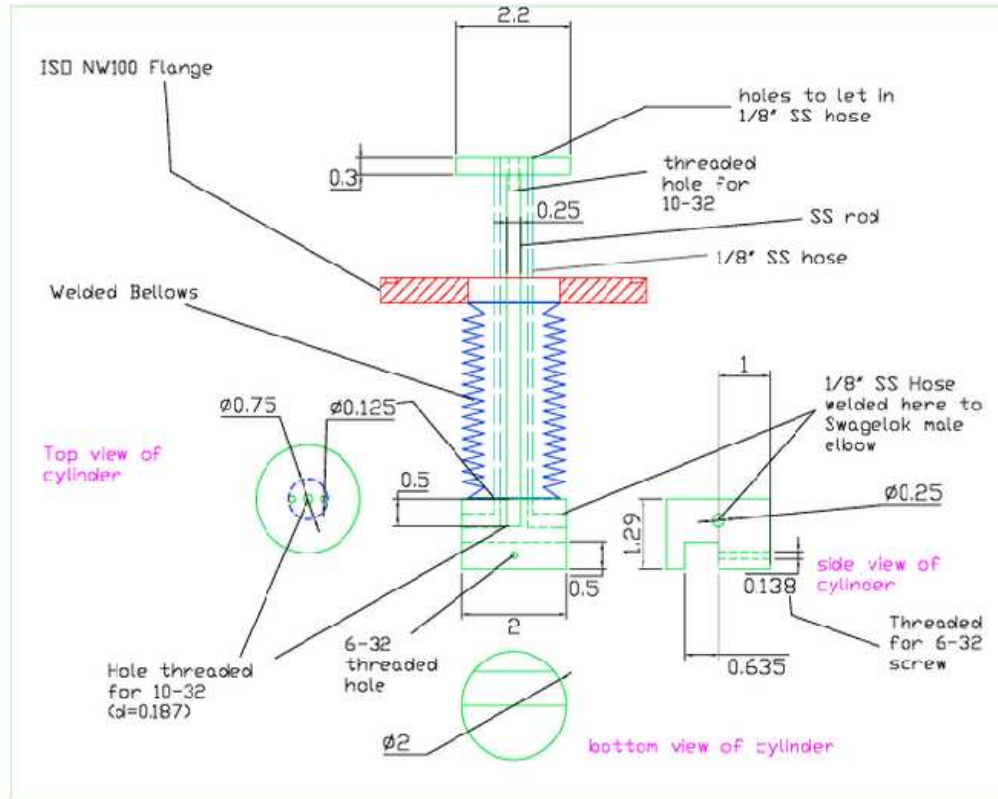


Figure 3.3. Bellows and flange arrangement for target ladder.
Dimensions are in inches

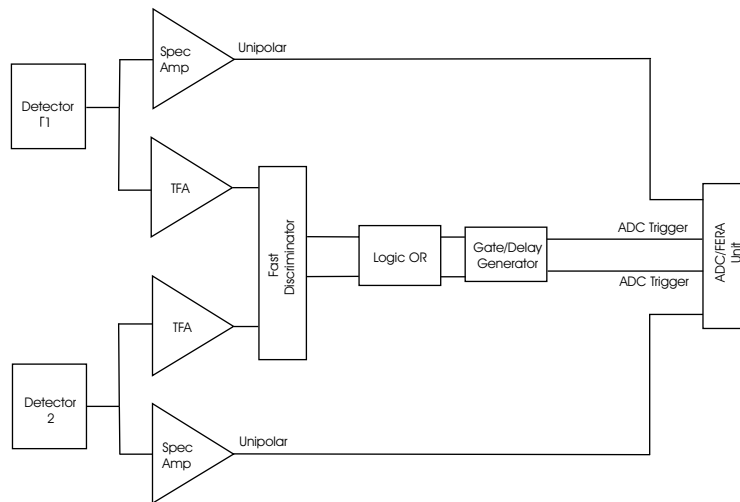


Figure 3.4. Schematic of electronics setup. Spec Amp = Spectroscopy Amplifier, TFA = Timing Filter Amplifier

3.3 Energy calibration

A ^{56}Co source, present at all times during data acquisition, provided γ -ray calibrations with energies up to 3.5 MeV. Calibration points at higher energies were obtained using the $^{27}\text{Al}(p, \gamma)$ and $^{35}\text{Cl}(n, \gamma)$ capture reactions. For the former, the target was prepared by thermal evaporation of 99.999% pure Aluminium in a Tungsten boat, deposited on a Tantalum backing. The target thickness was $\approx 20 \mu\text{g}/\text{cm}^2$. This ^{27}Al target was bombarded by a $15 \mu\text{A}$, 992 keV proton beam to produce γ -rays with well known energies up to 11 MeV [24]. For the $^{35}\text{Cl}(n, \gamma)$ reaction, the target ladder was removed and a Li_2O target placed at the edge of the target chamber as shown in Figure 3.8. This target was produced by thermal evaporation of Lithium Oxide in a Platinum boat. The ^7Li target was bombarded by a 600 nA, 1.912 MeV proton beam to produce neutrons in a forward-angle cone, with a nearly Maxwellian velocity distribution for neutron energies between

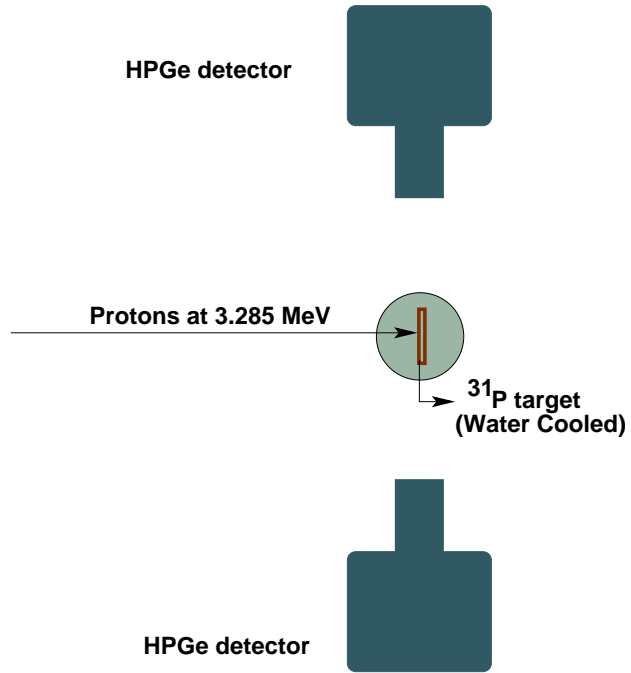


Figure 3.5. Top view of the experimental setup used for the $^{31}\text{P}(p, \gamma)$ data at $\theta_\gamma = 90^\circ$.

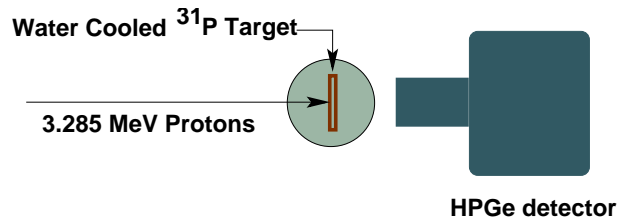


Figure 3.6. Top view of the experimental setup used for the $^{31}\text{P}(p, \gamma)$ data at $\theta_\gamma = 0^\circ$.

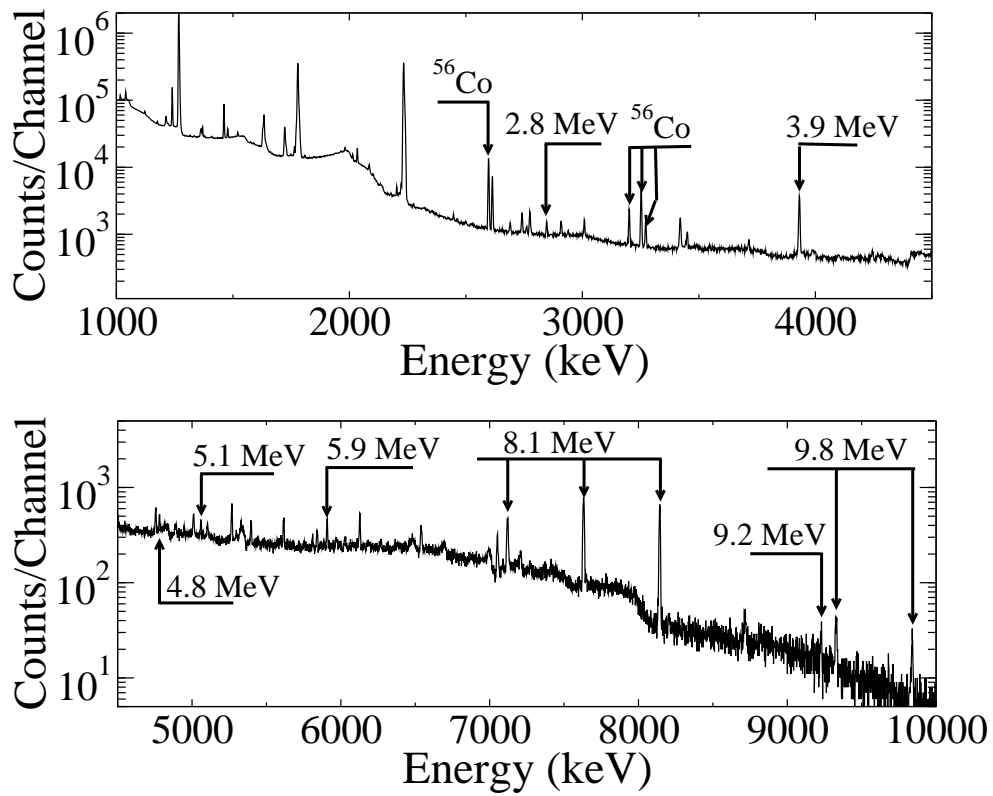


Figure 3.7. $^{31}\text{P}(p, \gamma)$ spectrum from the 0° experiment. The ^{32}S lines and some ^{56}Co calibration peaks are labeled. The 9.8 MeV γ ray is mainly from direct capture.

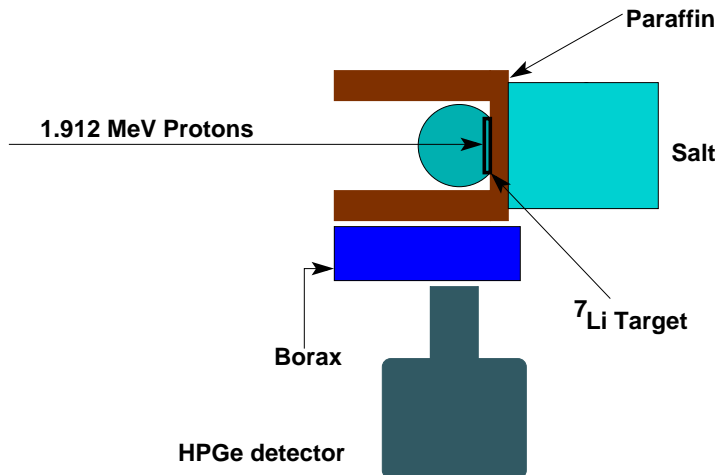


Figure 3.8. Top view of the experimental setup for the $^{35}\text{Cl}(n, \gamma)$ calibration used in the $\theta_\gamma = \pm 90^\circ$ measurement.

0 – 110 keV via the $^7\text{Li}(p, n)$ reaction [25]. The target thickness ($\approx 500 \mu\text{g}/\text{cm}^2$) was chosen such that all the protons lose energy up to the neutron-separation energy (≈ 1881 keV). The emitted neutrons were first moderated by a 4 cm thick paraffin slab, and then captured on to a $8 \times 10^3 \text{ cm}^3$ volume of NaCl to produce gamma rays with well-determined energies up to 8.5 MeV from $^{35}\text{Cl}(n, \gamma)$ [26]. The HPGe detector was moved to an angle of 90° approximately 60 cm from the center of the chamber as shown in Figure 3.8. Neutrons moving toward the Ge detector were moderated by 8 cm of paraffin and further attenuated by 15 cm of borax to protect the detectors from neutron damage. Figure 3.9 shows typical calibration spectra.

3.4 Data Analysis

Incomplete charge collection within Ge detectors produces exponentially decaying tails below gamma-ray peaks [27, 28] while multiple-Compton scattering

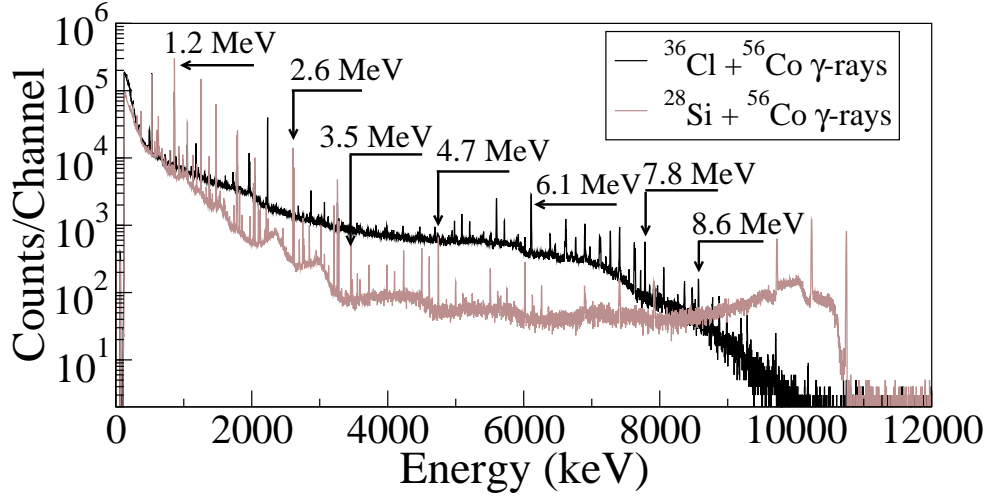


Figure 3.9. Calibration lines with detector positioned at 90° to the beam.

gives plateaus below the peak centroid. Peak centroids were extracted by fitting the γ peaks with a Gaussian folded with a delta function and two low-energy exponential tails. Each tail was of the form

$$T(x; \mu) = \frac{1}{2l} \exp \left[\frac{(x - \mu)}{l} + \frac{1}{2} \left(\frac{\sigma}{l} \right)^2 \right] \times \operatorname{erfc} \left[\frac{1}{\sqrt{2}} \left(\frac{(x - \mu)}{\sigma} + \frac{\sigma}{l} \right) \right], \quad (3.1)$$

where erfc is the complementary error function, l is the decay-length of the tail, σ is the Gaussian spread and μ is the peak centroid. The derivation to obtain $T(x; \mu)$ is described in detail in appendix A. The γ -peak line-shapes were assumed to have the form

$$L(x; \mu) = \sum_{i=1}^2 f_i T_i(x; \mu) + \frac{1}{\sqrt{2\pi\sigma^2}} \left(\exp \frac{-(x - \mu)^2}{2\sigma^2} \right), \quad (3.2)$$

where f_1 and f_2 were the relative areas of the exponential tails with respect to the pure Gaussian. Figure 3.10 shows the contribution of each tail to the photopeak

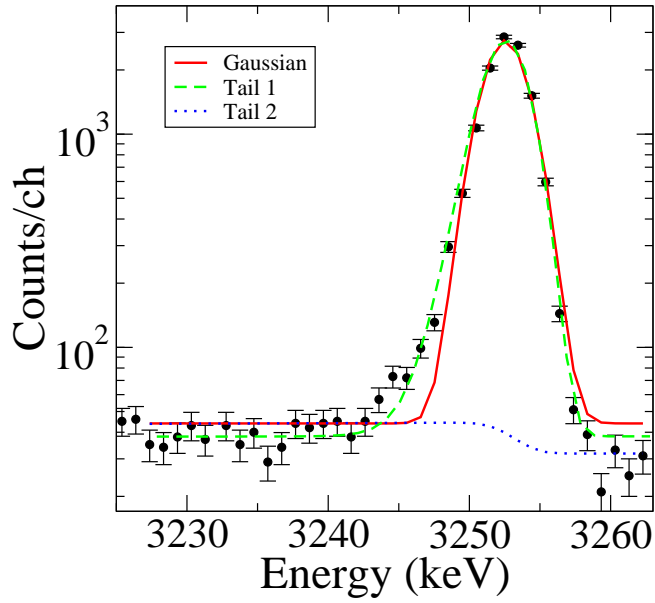


Figure 3.10. Line-shape of γ peak. The contribution of each parameter is shown.

for a ^{50}Co calibration line.

The γ spectrum was analyzed in the following manner: first, the line-shape of a high statistics peak from ^{56}Co at 3253 keV was determined by keeping the decay length of the second tail, l_2 (representing the multiple-Compton plateau below the centroid) at a large and fixed value (≈ 460 keV). Then, the background and the remaining parameters were varied to minimize χ^2 using the procedure described in Appendix A. The other peaks were then fitted by requiring l_1 and f_1 to scale linearly with energy while varying the other parameters to minimize χ^2 . Peaks on Compton edges of other γ rays were avoided so that we could fit the data using a flat background. Figure 3.11 shows two gamma rays of interest and their fits.

Sensitivity to ADC nonlinearities and line-shape variations were minimized in the following manner. The centroids, x_i , of a few calibration gamma-ray peaks

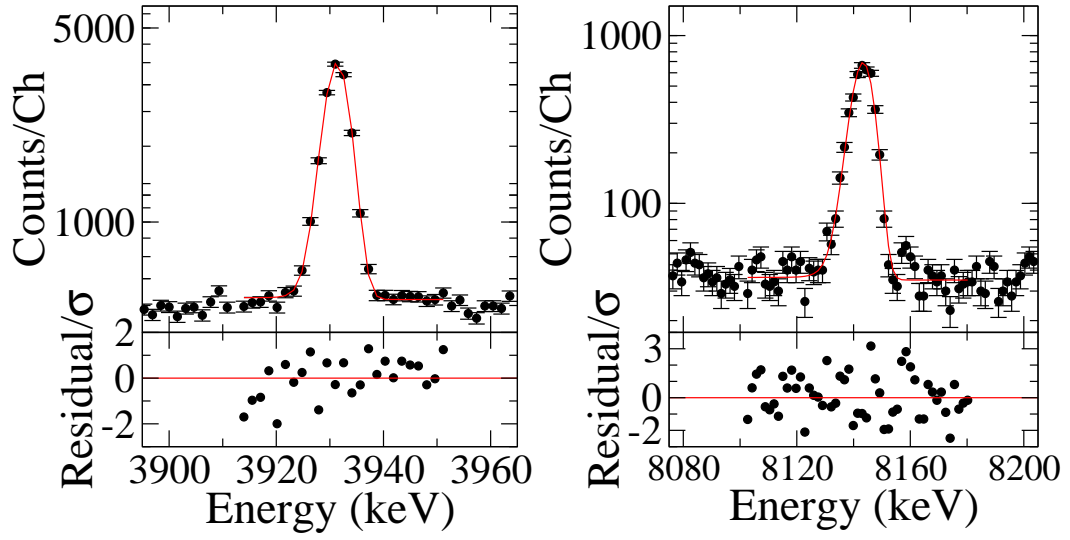


Figure 3.11. Fits to the most intense de-excitation gamma-rays from the $T = 2$ state.

around each $^{31}\text{P}(p, \gamma)$ line of interest were fitted to a linear function, $E_{\gamma i} = a + bx_i$. The uncertainties in peak centroids were obtained by combining in quadrature the errors due to counting statistics and uncertainties in the calibration energies. This provided the a and b coefficients, which related the $^{31}\text{P}(p, \gamma)$ energies to the closest calibration line,

$$E_{\gamma i}(^{32}\text{S}) = E_{\gamma i}(\text{cal}) + b \times [x_i(^{32}\text{S}) - x_i(\text{cal})] . \quad (3.3)$$

3.5 Systematic Effects

3.5.1 Gain Drifts

In spite of the use of a temperature-controlled electronics rack, small gain drifts did occur during the course of the experiment. These drifts were large enough to have a significant effect for the centroids at higher energies. Figure 3.12 shows

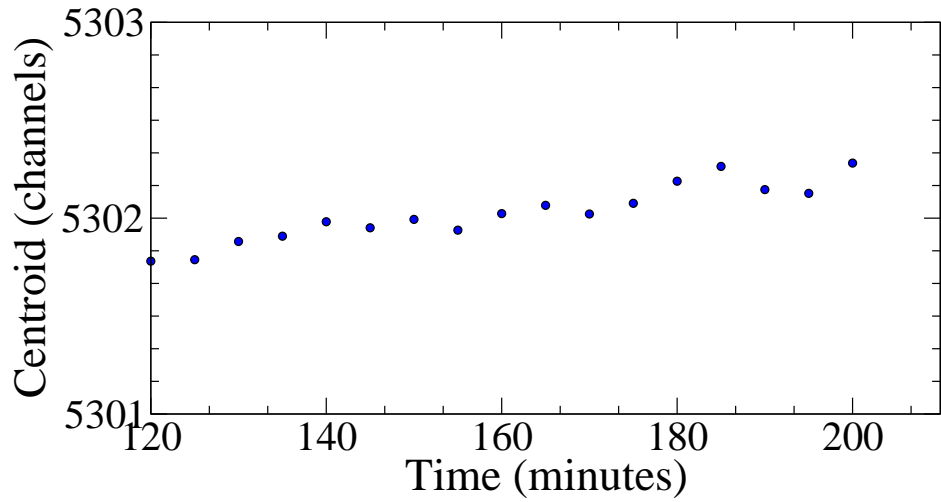


Figure 3.12. Centroid of the 2598 keV ^{56}Co γ peak as a function of time.

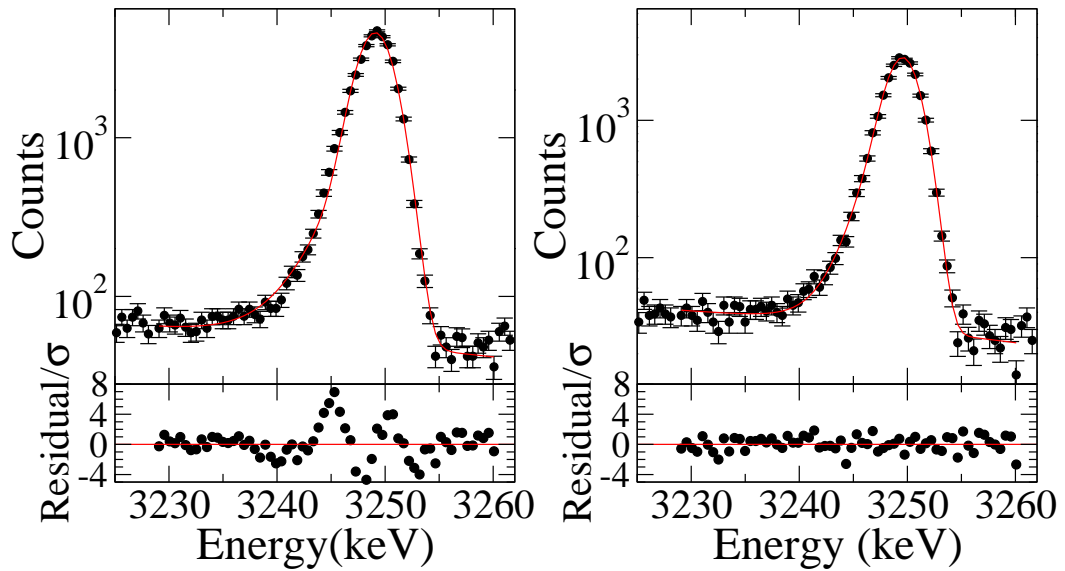


Figure 3.13. Gain shift correction applied to the data. The left panel shows the fit before correction, with $\chi^2/\nu = 3.99$. The right panel shows the data the corresponding fit after correction, with a much improved χ^2/ν of 1.09.

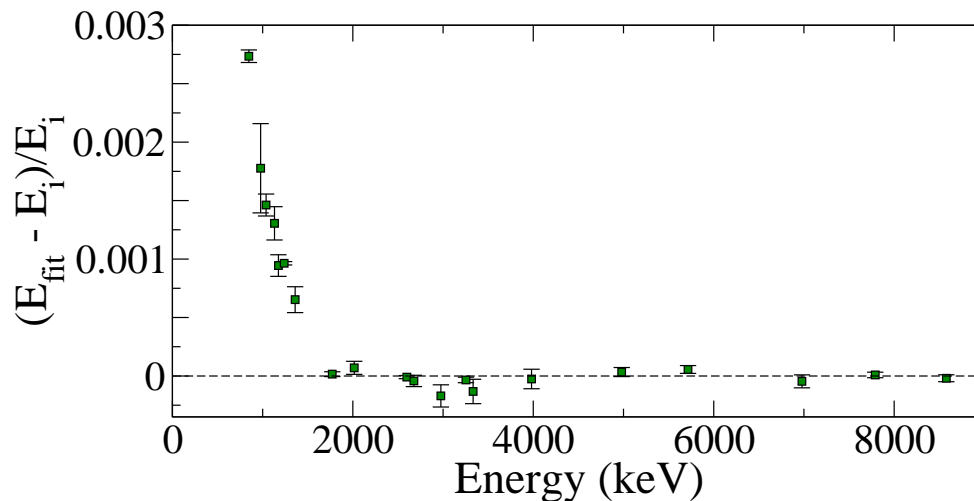


Figure 3.14. Nonlinearity of the ADC. The points show centroids of $^{35}\text{Cl}(n, \gamma)$ and ^{56}Co calibration lines. Pronounced differences are seen between the observed positions and a linear fit to the region between 2015 keV and 8578 keV.

the variation of the centroid of a ^{56}Co calibration line with time. Such gain shifts were corrected using a time stamp that was recorded for each event. Piecewise corrections to the data (taken over time intervals ranging between 15 and 180 minutes) were based on a few high statistics peaks. After each time interval, the centroid (μ) and the standard deviation (σ) for events belonging to these peaks were registered. Each of these calibrations were used to match the centroids of the shifted events to a fixed reference using a linear fitting routine. Events whose centroids were shifted by more than 3 standard deviations were vetoed from the spectrum. Figure 3.13 shows the marked improvement in the reduced χ^2 on fitting a calibration line before and after the application of such corrections. The ^{56}Co lines were common to all data sets and were used to correct gain shifts that may have occurred between runs when data were not being acquired.

3.5.2 ADC nonlinearities

Detector signals were digitized by an Ortec 413 ADC. We observed significant non-linearity in the energy range $0 \leq E_\gamma \leq 1.5$ MeV (see Figure 3.14) and did not use any lines in that range for gain-matching or energy determination. Additional data, taken with the doubled gains in the spectroscopy amplifiers, proved that the non-linearity was a property of the ADC and not of the preceding electronics; these data also provided an additional check on the energy of the 3.9 MeV $^{31}\text{P}(p, \gamma)$ gamma ray, which corresponds to a transition from the $T = 2$ state to the $J^\pi = 1^+$, $T = 1$ state at 8125 keV.

3.5.3 Doppler effects

Since the observed γ rays were emitted from a recoiling compound nucleus, their registered energies would be Doppler shifted depending on detector orientation. The Doppler-shifted energy observed by a detector at an angle θ_γ is given by

$$E' = E_0 \frac{\sqrt{1 - (v^2/c^2)}}{1 - (v/c) \cos \theta_\gamma} \quad (3.4)$$

which in the non-relativistic limit reduces to

$$E' = E_0 \left(1 + \frac{p}{m} \cos \theta_\gamma \right), \quad (3.5)$$

where p is the momentum of the recoiling compound nucleus. Although Doppler shifts are minimal at $\theta_\gamma = \pm 90^\circ$, the sensitivity to angular uncertainty is maximal. For the $\theta_\gamma = 0^\circ$ case, the Doppler shift is maximal, but there is least sensitivity to angular displacements. In addition, the shift in γ energies is attenuated due to the solid angle subtended by the detector. The Doppler shifts for both the geometries

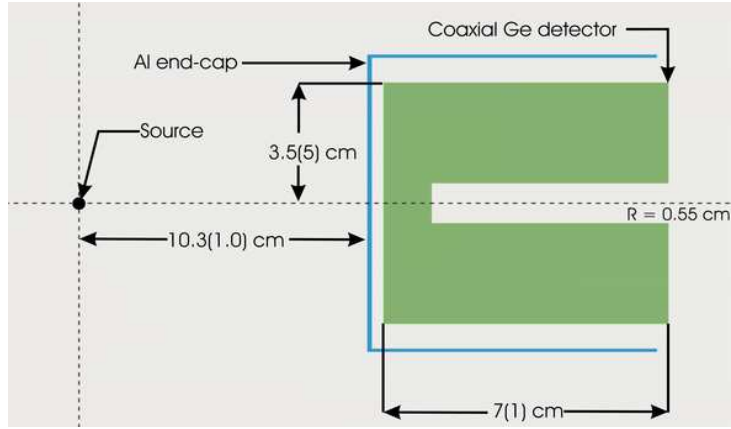


Figure 3.15. Detector geometry used for simulations. The dimensions of the crystal are obtained from the manufacturers. We make conservative estimates on the uncertainties.

were determined using careful Monte Carlo simulations using a conservative estimate of 1.0 cm for target-detector misalignment. Figure 3.15 shows the geometry of the Ge detector used for the simulations.

For the $^{31}\text{P}(p, \gamma)$ and the $^{27}\text{Al}(p, \gamma)$ gamma rays, the half-life of the decaying state was used to randomly generate decay times from an exponentially decaying distribution. The energy loss by the compound nucleus during that lifetime was calculated using the stopping power at that particular energy, which was determined using SRIM [23]. For the $^{27}\text{Al}(p, \gamma)$ reaction only the primary γ rays from the parent $E_x = 12541.31$ keV state were used for calibration since the angular correlations between the cascading gammas were unknown. Doppler broadenings of the secondary gammas from $^{31}\text{P}(p, \gamma)$ were simulated by accounting for the angular correlation between the two emitted gammas as well as the transverse component of momentum imparted by the emission of the first gamma ray.

For the $^{35}\text{Cl}(n, \gamma)$ reaction, the neutron angular-distribution results for $^7\text{Li}(p, n)$

from Ref. [25] were fed into a program that simulated neutron scattering on paraffin and neutron capture on ^{35}Cl . This simulation provided us with the eventual recoil velocities and positions of the ^{36}Cl nuclei prior to γ emission. The recoil velocities and directions and the known γ energies from Ref. [26] were entered into the radiation-transport program PENELOPE [29] to simulate the interaction of the γ radiation with the detector and calculate the net Doppler shift. Table 3.1 shows the results for the predicted Doppler shifts from the Monte Carlo simulations. The uncertainties in the predicted shifts arise from uncertainties in the detector solid angle, the lifetime of the state, the uncertainty in the stopping power and target-detector misalignment. Although the corrections for the 0° data are large, their model-dependence is very small because the shifts were virtually unattenuated; in all the cases the ions changed their velocities by $< 10^{-7} c$ during the parent state's lifetime.

TABLE 3.1
PREDICTED DOPPLER SHIFTS FROM MONTE CARLO
SIMULATIONS

Source	E_γ (keV)	Detector distance (cm)	Detector angle (deg)	Doppler shift (keV)
$^{31}\text{P}(p, \gamma)$	2840	10.3(1.0)	0.0(5.5)	7.28(5)
$^{31}\text{P}(p, \gamma)$	3922	10.3(1.0)	0.0(5.5)	10.06(7)
$^{31}\text{P}(p, \gamma)$	3922	59.0(1.0)	90.00(97)	0.00(17)
$^{31}\text{P}(p, \gamma)$	4770	10.3(1.0)	0.0(5.5)	12.16(7)

TABLE 3.1

Continued

Source	E_γ (keV)	Detector distance (cm)	Detector angle (deg)	Doppler shift (keV)
$^{31}\text{P}(p, \gamma)$	5046	10.3(1.0)	0.0(5.5)	12.94(9)
$^{31}\text{P}(p, \gamma)$	5894	10.3(1.0)	0.0(5.5)	15.11(10)
$^{31}\text{P}(p, \gamma)$	8124	10.3(1.0)	0.0(5.5)	20.83(13)
$^{31}\text{P}(p, \gamma)$	8124	59.0(1.0)	90.00(97)	0.00(36)
$^{31}\text{P}(p, \gamma)$	9206	10.3(1.0)	0.0(5.5)	23.21(16)
$^{27}\text{Al}(p, \gamma)$	2777	10.3(1.0)	0.0(5.5)	4.31(3)
$^{27}\text{Al}(p, \gamma)$	3062	10.3(1.0)	0.0(5.5)	4.75(3)
$^{27}\text{Al}(p, \gamma)$	3124	10.3(1.0)	0.0(5.5)	4.85(3)
$^{27}\text{Al}(p, \gamma)$	3376	10.3(1.0)	0.0(5.5)	5.24(3)
$^{27}\text{Al}(p, \gamma)$	3952	10.3(1.0)	0.0(5.5)	6.14(4)
$^{27}\text{Al}(p, \gamma)$	4607	10.3(1.0)	0.0(5.5)	7.15(4)
$^{27}\text{Al}(p, \gamma)$	4742	10.3(1.0)	0.0(5.5)	7.36(5)
$^{27}\text{Al}(p, \gamma)$	5653	10.3(1.0)	0.0(5.5)	8.78(6)
$^{27}\text{Al}(p, \gamma)$	5662	10.3(1.0)	0.0(5.5)	8.79(6)
$^{27}\text{Al}(p, \gamma)$	6264	10.3(1.0)	0.0(5.5)	9.73(6)
$^{27}\text{Al}(p, \gamma)$	7922	10.3(1.0)	0.0(5.5)	12.30(8)
$^{35}\text{Cl}(n, \gamma)$	1131	59.0(1.0)	90.00(97)	-0.03(3)
$^{35}\text{Cl}(n, \gamma)$	2676	59.0(1.0)	90.00(97)	-0.07(6)
$^{35}\text{Cl}(n, \gamma)$	2975	59.0(1.0)	90.00(97)	-0.08(7)

TABLE 3.1

Continued

Source	E_γ (keV)	Detector distance (cm)	Detector angle (deg)	Doppler shift (keV)
$^{35}\text{Cl}(n, \gamma)$	3333	59.0(1.0)	90.00(97)	-0.09(8)
$^{35}\text{Cl}(n, \gamma)$	3981	59.0(1.0)	90.00(97)	-0.11(9)
$^{35}\text{Cl}(n, \gamma)$	4980	59.0(1.0)	90.00(97)	-0.13(12)
$^{35}\text{Cl}(n, \gamma)$	5715	59.0(1.0)	90.00(97)	-0.15(13)
$^{35}\text{Cl}(n, \gamma)$	6978	59.0(1.0)	90.00(97)	-0.19(16)
$^{35}\text{Cl}(n, \gamma)$	7790	59.0(1.0)	90.00(97)	-0.21(18)
$^{35}\text{Cl}(n, \gamma)$	8579	59.0(1.0)	90.00(97)	-0.23(20)

3.5.4 The field-increment effect

Acceleration of primary and secondary charge carriers within the intrinsic volume of the detector and variations in the charge collection efficiency over the detector volume can shift the observed peaks in a manner that depends on source position, detector geometry, bias voltage and γ -ray energy [30]. It was important to test the magnitude of this effect in the measurement because the γ rays from the $^{31}\text{P}(p, \gamma)$ and $^{27}\text{Al}(p, \gamma)$ reactions were at $\approx 0^\circ$ to the detector, whereas the $^{35}\text{Cl}(n, \gamma)$ γ -rays were incident on the detector from the side (see Figure 3.8).

The magnitude of this effect was tested by fixing a ^{56}Co source at 0° to the

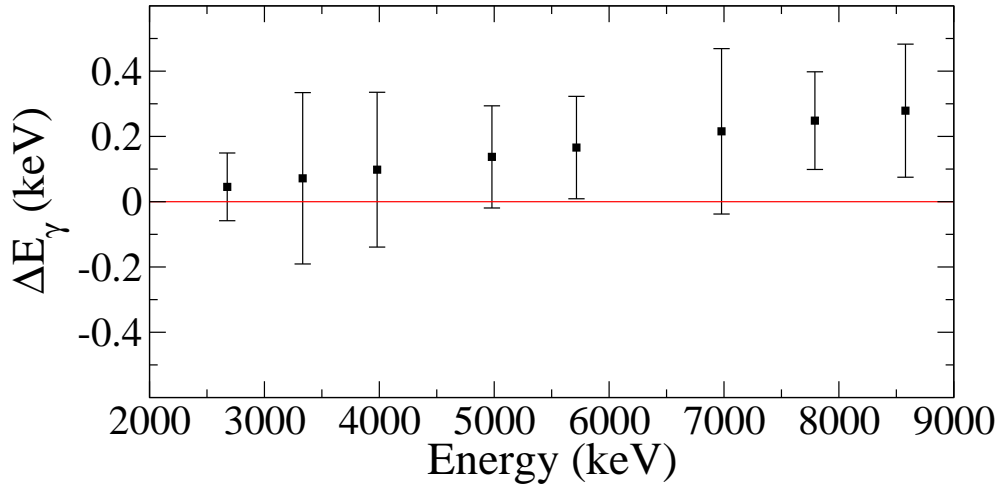


Figure 3.16. Shifts in apparent γ -ray energies with changes in the incident γ -ray angle. The y-axis shows the difference in the inferred Doppler-shift-corrected γ energies from $^{35}\text{Cl}(n, \gamma)$ at two extreme angles (incident along the axis of the co-axial detector and approximately normal to the detector axis).

detector at a distance of 5 cm from the detector end-cap. This provided an angle-independent reference. Then $^{35}\text{Cl}(n, \gamma)$ data were taken with the Ge detector at 65° , 90° and 125° to the beam at the center of the chamber. This ensured that the ^{36}Cl γ rays were incident on the detector at three different angles, while gammas from the ^{56}Co source were always from a fixed position. The energies of the $^{35}\text{Cl}(n, \gamma)$ lines were corrected for Doppler shifts as previously described. Figure 3.16 shows the difference between the Doppler-shift-corrected data at 125° and 65° . A small systematic effect may be present, but it was not large compared to our other uncertainties. The shifts are relatively insignificant for high energies.

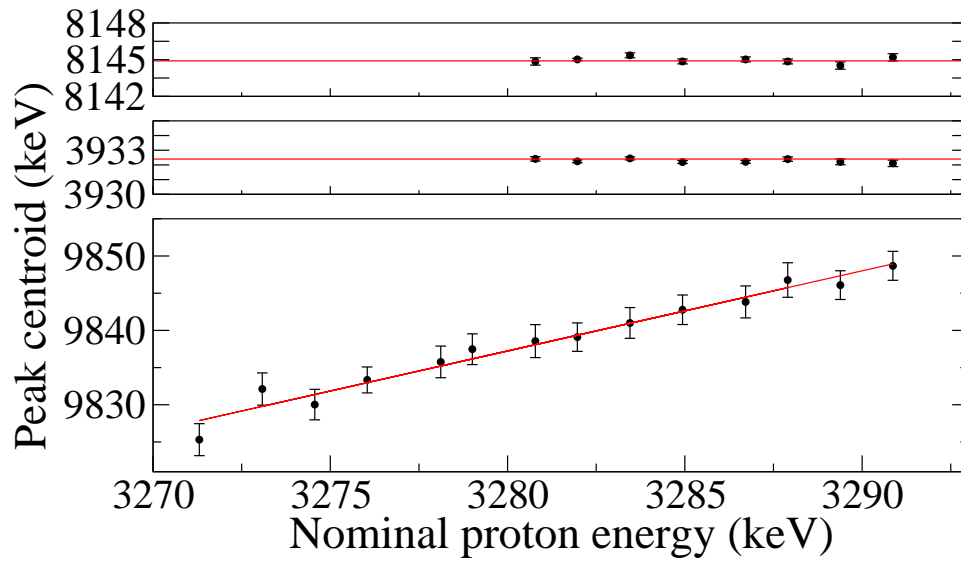


Figure 3.17. Energies of the 3.9 and 8.1 MeV γ peaks versus proton energy in the lab frame. For comparison the γ_1 data is shown (which corresponds to transitions to the first excited state at 2.2 MeV). The γ_1 data shows a non-resonant behavior as expected.

3.5.5 Nonresonant background

If there were non-resonant components to the $^{31}\text{P}(p, \gamma)$ γ -rays, they would shift their centroids in a manner depending on the beam energy and the structure of the target. The data showed no evidence for such non-resonant components. Figure 3.17 shows the centroids of 3922 and 8124 keV γ rays versus proton energy from the 0° detector. Data points at lower proton energies are missing for the 3.9 MeV and 8.1 MeV gammas because there are no observable peaks. For comparison we show the centroid for the γ_1 yield, which does not come from a narrow resonance.

3.6 Results and Discussion

3.6.1 Excitation energy of the $T = 2$ state

The precision of the $\pm 90^\circ$ data was limited both by possible misalignments of the Ge detectors and by the incident-angle dependence of the pulse height in the ^{36}Cl calibration. The 0° data, on the other hand, were limited by uncertainties in the calibration γ ray energies and peak line-shapes. Table 3.2 shows the gamma ray energies deduced from this work. The 3.9 MeV and 8.1 MeV γ ray energies are obtained from a weighted mean of the 0° and the 90° data. Since some of the uncertainties are common to both data sets, we use only the uncertainties from the 0° data in Table 3.2. The excitation energies of the levels are obtained by adding the energies of the cascading γ rays to the nuclear recoil energy. The excitation energy of the $J^\pi, T = 1^+, 1$ state at 8.1 MeV was obtained using the weighted mean of the excitation energy from the 5894-2230 keV cascade and the 8124 keV γ ray. On comparison with previous determinations, we obtain satisfactory agreement

TABLE 3.2
 LEVEL ENERGIES AND DOPPLER-CORRECTED
 GAMMA RAY ENERGIES FROM ^{32}S .

J^π, T	E_x (keV)		E_γ (keV)
	Previous work	This work	
2 ⁺ , 0	2230.57(15) ^a
1 ⁺ , 1	7002.5(10) ^b	7001.44(36)	4770.49(33)
1 ⁺ , 1	8125.40(20) ^a	8125.32(24)	5894.32(28) 8124.12(24)
1 ⁺ , 1	9207.5(7) ^b	9207.55(71)	9206.13(71)
0 ⁺ , 2	12045.0(4) ^c	12047.96(28)	2840.32(14) 3922.37(15) 5046.09(39)

^a M. Babilon *et al.* [31].

^b From Ref. [32].

^c M. S. Antony *et al.* [20].

TABLE 3.3

GAMMA-RAY ENERGIES FOR CASCADES FROM
THE LOWEST $T = 2$ STATE IN ^{32}S .

E_{γ_1} (keV)	E_{γ_2} (keV)	E_x (keV)
5046.09(39)	4770.49(33) ^a	12047.96(53)
3922.37(15)	8124.12(24)	12047.86(28)
3922.37(15)	5894.32(28) ^a	12048.10(35)
2840.32(14)	9206.13(71)	12048.01(72)
Combined value		12047.96(28)

^a This γ -ray de-excites to $E_{x1} = 2230.57(15)$ keV [31].

for the excitation energies of the three $T = 1$ levels fed by the $T = 2$ state, but not with the previously cited value [20] for the excitation energy of the $T = 2$ state itself. Table 3.3 shows the gamma energies in the 3 cascade chains observed in this work and the deduced excitation energy of the $T = 2$ level. Since the uncertainties are correlated we use the smallest of the uncertainties in the data as the total uncertainty in the excitation energy. Our value for the excitation energy of the lowest $T = 2$ state, 12047.96(28) keV, is about 3.0 keV ($\approx 7\sigma$) higher than that reported by Antony *et al.* [20] but agrees well with the lower-precision results of Ref. [19].

3.6.2 Relative gamma branches from the $T = 2$ state

In addition to precise determination of excitation energies in ^{32}S , we obtain more precise values for the relative γ branches from the $T = 2$ state in ^{32}S . The relative branches to states labelled by i were obtained by

$$BR(i) = \frac{A(i)}{\left(\sum_{j=1}^3 \frac{A(j)\eta(i)}{\eta(j)} \right)}, \quad (3.6)$$

where A represents the photopeak area and η is the efficiency for detecting a particular γ ray. The γ detection efficiencies at various γ ray energies were obtained using PENELOPE Monte Carlo simulations. Table 3.4 shows the relative γ branches. A 6% uncertainty was assumed in the ratio of γ -detection efficiencies. For comparison we show the relative branches from the isobaric analog state in the mirror ^{32}P nucleus.

3.6.3 Isospin violating γ decays

The transition matrix element for electromagnetic transitions in nuclei is composed of isoscalar and isovector components. The isospin selection rules follow as a direct consequence, i.e., $\Delta T = 0, \pm 1$ for allowed γ transitions [34].

The lowest $T = 2$ state in ^{32}S provides an excellent opportunity to investigate the possibility of an additional isotensor component to the electromagnetic interaction. Such a component would allow $\Delta T = 2$ γ transitions, which, in this particular case, would be manifest as a resonant component to the γ_1 yield at $E_\gamma = 9.8$ MeV. Although a previous measurement showed a flat background for the γ_1 yield [35], it was interesting to check for a significant contribution to the

TABLE 3.4

RELATIVE GAMMA BRANCHES (IN %) FROM THE
 LOWEST $A = 32$ $T = 2$ STATES. EXCITATION ENERGIES
 ARE IN KEV

Final st.	^{32}P		^{32}S		
	E_x	Ref. [33]	E_x	Ref. [21]	This Work
$1_3^+;1$	2230	9.4(5)	9208	11(2)	9.4(7)
$1_2^+;1$	1149	85.7(8)	8125	83(8)	84.3(9)
$1_1^+;1$	0	4.7(6)	7001	6(1)	6.3(7)

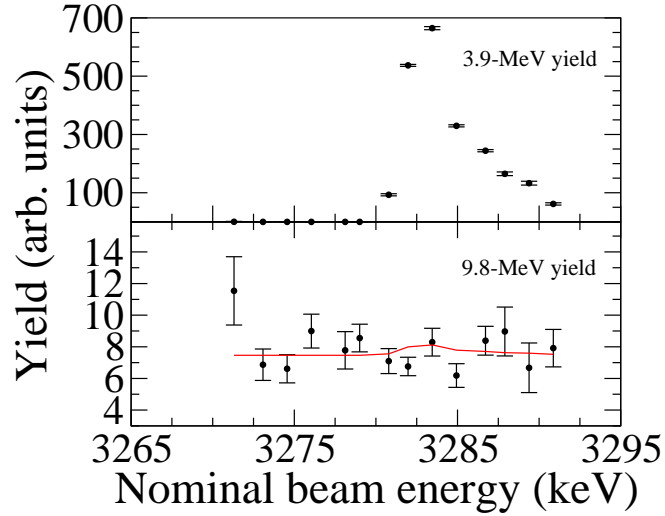


Figure 3.18. Top panel: Excitation function of 3922-keV γ yield.
 Bottom panel: Excitation function of γ_1 yield (this includes the single
 escape peak for additional statistics). The continuous line shows the
 upper limit described in the text.

γ_1 yield in this particular experiment.

Figure 3.18 shows excitation functions for the 3.9 MeV γ ray (that corresponds to an isospin-allowed, $\Delta T = 1$ transition) and the 9.8 MeV γ ray. These were obtained by varying the proton energy in steps of ≈ 1 keV through the resonance and observing the yields. The γ_1 yield data were fitted to a model using the method of least squares with two adjustable parameters (a constant background and a resonant term), which was assumed to have the same shape as the 3922-keV γ yield. The best fit gave a resonant contribution consistent with zero. We assumed the resonant γ_1 yield to be factor 10^{-3} smaller than the 3922-keV yield. An upper limit on the isospin violating branch was obtained using

$$BR(9.8 \text{ MeV}) = BR(3.9 \text{ MeV}) \times 10^{-3} \times \frac{\eta(3.9 \text{ MeV})}{\eta(9.8 \text{ MeV})}. \quad (3.7)$$

This upper limit was 0.25% at the 90% confidence level and yielded a γ_1 width of ≤ 7.3 meV.

Our measured strength ratio $\Gamma_{\gamma_1}/\Gamma_{\gamma}(3.9 \text{ MeV})$ when expressed as an $E2/M1$ ratio of Weisskopf reduced strengths is less than 0.9%.

3.6.4 A test of the IMME

On combining our results with the best available results for the other 4 members of the $A = 32$ isospin multiplet, we obtain the most precisely measured quintet known to date. The revised masses are shown in Table 3.5. The measured mass excesses were fitted to the IMME using a second-order polynomial fitting routine. Ref. [37] was used for the ^{32}Si mass rather than the more precise value from the latest compilation [36] because the uncertainty quoted for the mass was

TABLE 3.5

COMPARISON OF MEASURED MASS EXCESSES OF THE
 LOWEST $T = 2$, $A = 32$ QUINTET WITH IMME FIT

Isobar	T_3	M_{Exp} (keV) ^a	M_{IMME} (keV)
³² Si	-2	-24080.86(77) ^b	-24082.52(61)
³² P	-1	-19232.78(20) ^c	-19232.48(18)
³² S	0	-13967.74(31) ^d	-13968.32(26)
³² Cl	+1	-8291.5(1.8) ^e	-8290.05(63)
³² Ar	+2	-2200.2(1.8) ^f	-2197.67(1.50)

$Q(\chi^2 = 13.1, \nu = 2)^g = 0.001$

^a Ground state masses are from Ref. [36].

^b From Ref. [37].

^c $E_x = 5072.44 \pm 0.06$ keV from Ref. [22].

^d This work.

^e M. C. Pyle *et al.* [16].

^f K. Blaum *et al.* [18].

^g $Q(\chi_0^2, \nu)$ is the probability of obtaining a set of data with $\chi^2 \geq \chi_0^2$, given that the model is correct.

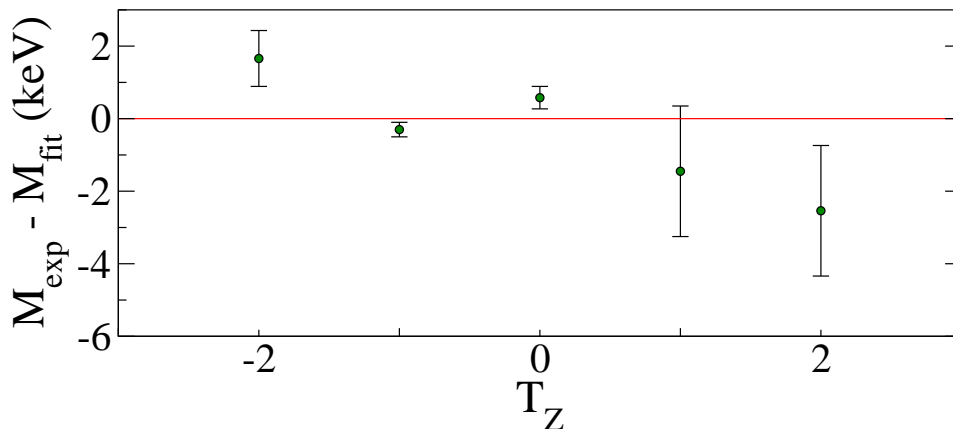


Figure 3.19. Difference between measured mass excesses and IMME fit for the $A = 32$, $T = 2$ quintet in keV.

≈ 15 times smaller than that quoted by the experimenters themselves. Because of the high precision attained in this multiplet, a new measurement of the ^{32}Si mass would be welcome as the existing mass measurements are not well documented ². The fit results are shown in Table 3.5 and Figure 3.19. We observe a significant disagreement with the IMME prediction, $Q(\chi^2, \nu) = 0.001$. Reasonable agreement with the data, $Q(\chi^2, \nu) = 0.21$, can be found by adding a very small cubic term, dT_z^3 to the IMME with $d = 0.54 \pm 0.16$ keV, which is the smallest known and most precisely determined violation of the IMME. For comparison, the most precise determination of a d coefficient previously had an uncertainty of 1.4 keV [11]. Fitting the data with a quartic term rather than a cubic term yields a quartic coefficient, $e = 0.53 \pm 0.15$ keV; with $Q(\chi^2, \nu) = 0.64$.

²Ref. [36] calculated the mass from the $^{31}\text{Si}(n, \gamma)$ gamma-ray energy published in Ref. [38], but corrected the unreasonable published uncertainty of 0.0005 keV to 0.05 keV by studying how well other known γ -ray energies were reproduced. However, the authors of Ref. [38] themselves presented a revised evaluation of the mass of ^{32}Si with an uncertainty of $0.822 \mu\text{u}$ or 0.77 keV [37].

3.6.5 Isospin mixing with other 0^+ levels

The presence of nearby 0^+ levels could affect the isospin purity of the $T = 2$ state in ^{32}S and lead to breakdown of the IMME. In particular, for the case of two-state isospin mixing, the $T = 2$ state would possess an admixture of the other 0^+ state and vice-versa, such that

$$|T = 2\rangle = \alpha|\Psi; T = 2\rangle + \beta|\Psi; T\rangle \quad (3.8)$$

$$|T_{\text{admixed}}\rangle = -\beta|\Psi; T = 2\rangle + \alpha|\Psi; T\rangle, \quad (3.9)$$

where $|\Psi; T = 2\rangle$ and $|\Psi; T\rangle$ represent the unperturbed states of pure isospin, and, $\alpha^2 + \beta^2 = 1$. The energy difference between the perturbed states is given by

$$E(i) - E(j) = \Delta E_u \sqrt{1 + \frac{4\langle\Psi; T = 2|H_{IM}|\Psi; T\rangle^2}{\Delta E_u^2}}, \quad (3.10)$$

where the indices i and j label the perturbed energy levels, ΔE_u is the energy spacing between the unperturbed levels and the isospin-mixing matrix element is $\langle\Psi; T = 2|H_{IM}|\Psi; T\rangle$.

Such isospin mixing would allow an isospin forbidden $\Delta T = 2$ $E2$ transition from the $T = 2$ state to the first excited $J^\pi = 2^+$, $T = 0$ state at 2.2 MeV. Although we do not observe such a transition, the mixing scenario cannot be ruled out. Excellent agreement with the IMME in the $A = 32$ system, $Q(\chi^2, \nu) = 0.74$, would be obtained if the excitation energy of the $T = 2$ state in ^{32}S were 2.5 keV lower than our results. Two 0^+ levels are known [32] to lie slightly below the $T = 2$ state and are potential candidates for the admixed level. A 100 eV wide $J^\pi, T = 0^+, 0$ state at $E_x = 11930$ keV lies 118 keV below the $T = 2$ state. An isospin-mixing matrix element of ≈ 17 keV would shift the $T = 2$ state upward by

2.5 keV, implying an isospin impurity with an intensity of 2.1%. This $J^\pi, T = 0^+, 0$ level would not affect the positions of the $T = 2$ states in ^{32}P and ^{32}Cl , which is consistent with the data. A second $J^\pi = 0^+$ level (of unknown isospin) occurs at $E_x = 11869$ keV. If this level were responsible for the 2.5 keV shift, it would need a mixing matrix element of 21 keV and an isospin impurity with an intensity of 1.4%. Matrix elements of this size are not implausible.

We measured excitation functions around both the 11930 and 11869 keV resonances and found no resonant component to the γ_1 yield on the first resonance and a significant yield on the second. Assuming $\Gamma_p/\Gamma = 1$ in all cases, the $T = 2$, 11930 keV and 11869 keV states have γ_1 widths of ≤ 7.3 , ≤ 52 and $330(70)$ meV. These results however do not provide enough information to exclude either of the levels as the source of the isospin admixture.

3.7 Conclusions

This precision measurement of the mass of the lowest $T = 2$ state in ^{32}S ($\Delta M/M \approx 10^{-5}$) makes the $A = 32$ multiplet the most precisely measured $T = 2$ quintet and easily provides the most stringent test of the isobaric multiplet mass equation. Such a test provides the best demonstration of the validity of the approximations inherent in the IMME and its utility for predicting masses away from the valley of stability. A significant violation of the isobaric multiplet mass equation is observed. This violation could be explained by isospin-mixing with a nearby 0^+ level.

CHAPTER 4

$0^+ \rightarrow 0^+$ FERMI DECAYS: PROBES TO TEST THE STANDARD MODEL

In this chapter we introduce the motivation to measure the ft value for the $0^+ \rightarrow 0^+$ beta-decay of ^{32}Ar . Such measurements are critical for Standard Model tests in the quest for a more complete theory of fundamental interactions.

4.1 The standard electroweak model for quarks and leptons and CKM unitarity

The Standard Model of electroweak interactions provides a unified theory that couples the electromagnetic and weak interactions. Both these interactions are introduced as different components of a single gauge theory, based on the group $SU(2) \times U(1)$. In the minimal Standard Model [39], the leptonic and the hadronic fields can be decomposed into left-handed $SU(2)$ doublets and right-handed singlets in weak-isospin space. Gauge invariance under local $SU(2) \times U(1)$ transformations requires the presence of the vector gauge fields $W_\mu^i(x)$, $i = 1, 2, 3$ and $B_\mu(x)$ for the $SU(2)$ and $U(1)$ sectors respectively, which couple to the fermionic fields with their associated gauge coupling constants g and g' .

The framework of the Standard Model explained above can be classified in a scheme with three generations of quarks and leptons as shown in Table 4.1. Maximal parity violation indicates that the charged weak currents are purely left-handed for quarks and leptons at low energies. The absence of right-handed

TABLE 4.1

THE THREE GENERATION STANDARD MODEL OF
QUARKS AND LEPTONS

	Leptons	Charge	T_3^a
doublets:	$\begin{pmatrix} \nu_e \\ e \end{pmatrix}_L$ $\begin{pmatrix} \nu_\mu \\ \mu \end{pmatrix}_L$ $\begin{pmatrix} \nu_\tau \\ \tau \end{pmatrix}_L$	0 -1	1/2 -1/2
singlets:	e_R μ_R τ_R	-1	0
	Quarks	Charge	T_3^a
doublets:	$\begin{pmatrix} u \\ d \end{pmatrix}_L$ $\begin{pmatrix} c \\ s \end{pmatrix}_L$ $\begin{pmatrix} t \\ b \end{pmatrix}_L$	+2/3 -1/3	1/2 -1/2
singlets:	u_R c_R t_R d_R s_R b_R	+2/3 -1/3	0 0

^a Analogous to section 2.1, T_3 is a component of *weak* isospin.

currents is incorporated within the standard electroweak model in a $SU(2)_L \times U(1)$ gauge theory, such that the transformations act on only the left-handed doublets in Table 4.1. It is however known that the quark doublets in Table 4.1 do not participate as pure states in the weak interaction. Experimental comparison of the strengths of strangeness-conserving decays to the strengths of strangeness-changing processes validate this claim. Such compelling experimental evidence prompted the Cabibbo hypothesis, which modifies the weak hadronic current in terms of one parameter, θ_C , the Cabibbo angle [40]. The phenomenon of Cabibbo mixing was later generalized for three quark families and parameterized using a 3×3 matrix [41] called the Cabibbo-Kobayashi-Maskawa matrix (denoted henceforth as the CKM matrix) that relates the weak eigenstates to the mass eigenstates via a unitary transformation, such that the weak eigenstates can be expressed as a linear combination of the mass eigenstates ³

$$\begin{pmatrix} d' \\ s' \\ b' \end{pmatrix} = \begin{pmatrix} V_{ud} & V_{us} & V_{ub} \\ V_{cd} & V_{cs} & V_{cb} \\ V_{td} & V_{ts} & V_{tb} \end{pmatrix} \begin{pmatrix} d \\ s \\ b \end{pmatrix} = V_{CKM} \begin{pmatrix} d \\ s \\ b \end{pmatrix}. \quad (4.1)$$

The weak hadronic current is modified similarly

$$J_\mu^h = (\bar{u} \quad \bar{c} \quad \bar{t}) \gamma_\mu (1 - \gamma_5) V_{CKM} \begin{pmatrix} d \\ s \\ b \end{pmatrix}. \quad (4.2)$$

Each element of the CKM matrix is experimentally determined from the weak decays of the relevant quarks. In the recent past, considerable interest arose to

³In the lepton sector, similar mixing exists owing to non-zero neutrino masses.

check the unitarity of this mixing matrix. This has prompted various experimental programs to measure the matrix elements with high precision [42]. Any deviation from unitarity would indicate the need for a modification of the theory and provide experimental evidence of extensions to the minimal Standard Model. This could indicate a variety of new scenarios, such as the existence of right-handed currents ⁴, more than three generations of quarks and leptons [44] or mixing with exotic fermions [45].

Currently, the most stringent experimental test of CKM unitarity is in the first row such that

$$|V_{ud}|^2 + |V_{us}|^2 + |V_{ub}|^2 = 1 - \delta , \quad (4.3)$$

where a nonzero value of δ would violate the unitarity condition and indicate ‘new physics’.

The largest matrix element in Eq. (4.3) is V_{ud} , which makes its uncertainty critical for unitarity tests. The value of V_{ud} can be determined using three different methods:

1. Nuclear superallowed Fermi beta-decays.
2. Decay of the free neutron.
3. Pion beta-decay.

In what follows below, we give a brief description of the methods and limitations involved in extracting V_{ud} from these three methods. In particular, we shall focus on superallowed Fermi transitions in nuclei which currently provide the most precise value of V_{ud} .

⁴For example, as predicted by manifest left-right symmetric models [43].

4.2 Methods to extract the value of V_{ud}

4.2.1 Superallowed Fermi decays

The transition probability per unit time for a beta-decay is given by Fermi's Golden Rule. If the beta particle is emitted with a momentum between $\hbar\mathbf{k}_e$ and $\hbar(\mathbf{k}_e + d\mathbf{k}_e)$ and the neutrino is emitted with a momentum between $\hbar\mathbf{k}_\nu$ and $\hbar(\mathbf{k}_\nu + d\mathbf{k}_\nu)$, then the decay rate is given by:

$$dw_{fi} = \frac{2\pi}{\hbar} |M_{fi}|^2 \frac{d\mathbf{k}_e}{(2\pi)^3} \frac{d\mathbf{k}_\nu}{(2\pi)^3} \delta(E_o - E_e - E_\nu) , \quad (4.4)$$

E_0 being the beta end-point energy. In a simpler form, the decay rate can be expressed as

$$\frac{1}{t} = \frac{2\pi}{\hbar} |M_{fi}|^2 f , \quad (4.5)$$

where M_{fi} is the matrix element responsible for the transition from a state $|i\rangle$ to a state $|f\rangle$ and f is the phase space available for the decay. The $V - A$ structure of the weak interaction allows us to decompose the matrix element for allowed beta-transitions into two components, the Gamow-Teller component (GT) and the Fermi component (F). This matrix element can be expressed as

$$|M_{fi}|^2 = G_V^2 |M_F|^2 + G_A^2 |M_{GT}|^2 , \quad (4.6)$$

where G_V and G_A are the effective vector and axial-vector coupling constants respectively. The vector and axial-vector matrix elements can be expressed in terms of reduced matrix elements as

$$|M_F|^2 = \frac{1}{2J_i + 1} \sum_{f,i} |\langle f || \sum_k \tau^{(\pm)}(k) || i \rangle|^2 , \quad (4.7)$$

and

$$|M_{GT}|^2 = \frac{1}{2J_i + 1} \sum_{f,i} |\langle f || \sum_k \tau^{(\pm)}(k) \boldsymbol{\sigma}(k) || i \rangle|^2, \quad (4.8)$$

where $\tau^{(\pm)}(k)$ are the isospin raising and lowering operators introduced in §. 2.1, the components of $\boldsymbol{\sigma}(k)$ are the three Pauli spin matrices and J_i is the total angular momentum of the initial state i .

The nature of the transition matrix elements in Eqs. (4.7) and (4.8) imply that for $0^+ \rightarrow 0^+$ nuclear beta-decays (also known as superallowed Fermi transitions), the Gamow-Teller decay strength does not contribute to the lowest order and the weak current is a purely vector interaction. The nuclear matrix element for such transitions is given purely by the expectation value of the isospin ladder operator in Eq. (4.7), which is a simple $SU(2)$ Clebsch-Gordon coefficient. Since the parent and the daughter states for such transitions are isobaric analogs of each other, the decay is largely independent of nuclear structure effects, assuming that isospin is an exact symmetry. Therefore, on substituting Eq. (4.6) into Eq. (4.5) with $|M_{GT}| = 0$, it is obvious that for all such transitions occurring between states of the same isospin the ft value (*the comparative half-life*) should ideally be a constant, i.e.

$$ft = \frac{K}{G_V^2 |M_F|^2}, \quad (4.9)$$

K being a constant. The experimental data required to extract the ft value for a given $0^+ \rightarrow 0^+$ decay are shown in Figure 4.1. The Q_{EC} value is essential to extract the phase space, f , available for the decay, while measurements of the superallowed branch and the half-life give the partial half-life, t , for the superallowed transition.

The constancy of ft values predicted by Eq. (4.9) is, however, based on a few important assumptions:

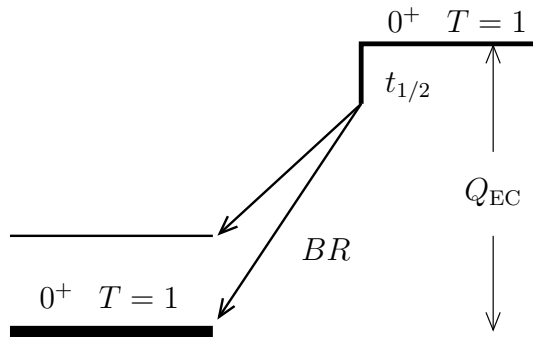


Figure 4.1. The experimental data needed to measure the ft value for a superallowed transition

- The vector coupling constant is not renormalized in the many-body nuclear medium (the conserved vector current hypothesis).
- Isospin symmetry is not violated.
- There are no radiative corrections required.

It is well known that based on these assumptions, the ft values of various superallowed transitions are constant only at the few percent level [46]. Precise measurements of ft values of various $T = 1$ emitters indicate a breakdown of such constancy, which, as we shall see, is restored once theoretical corrections [47] accounting for the above assumptions are included. We now describe the implications of these three assumptions and the corrections involved therein.

4.2.1.1 The CVC hypothesis

The conserved vector current hypothesis [48, 49] was postulated in analogy to the conservation of the electromagnetic current. In the case of electromagnetism,

the coupling constant (e) to the electromagnetic field is unaffected by the emission or absorption of virtual particles, such that the net charge of the system is conserved. The electromagnetic current is a combination of only isoscalar and isovector components. This current can be written in terms of these components as

$$\begin{aligned}
j_\mu^{EM} = & \frac{1}{2} \bar{\psi} [F_1^S(k^2) \gamma_\mu + i \frac{F_2^S(k^2)}{2M} \sigma_{\mu\nu} k_\nu + F_3^S(k^2) k_\mu] \psi \\
& + \bar{\psi} [F_1^V(k^2) \gamma_\mu + i \frac{F_2^V(k^2)}{2M} \sigma_{\mu\nu} k_\nu + F_3^V(k^2) k_\mu] \frac{1}{2} \tau_3 \psi ,
\end{aligned} \tag{4.10}$$

where k_μ is the momentum transferred, and the isoscalar and isovector form factors are defined in terms of the proton and neutron form factors by

$$\begin{aligned}
F_i^S(k^2) &= F_i^p(k^2) + F_i^n(k^2) \\
F_i^V(k^2) &= F_i^p(k^2) - F_i^n(k^2)
\end{aligned} \tag{4.11}$$

for $i = 1, 2, 3$. In the zero momentum transfer limit, the first form factor F_1 of the isovector current is the charge of the nucleon in units of e . In other words, the electromagnetic coupling constant is unaffected by strong interactions.

The weak vector current for the hadronic sector can be expressed as a Lorentz invariant vector (neglecting recoil order effects) in a similar manner

$$V_\mu^h = \bar{\psi} [g_V(k^2) \gamma_\mu + i \frac{g_M(k^2)}{2M} \sigma_{\mu\nu} k_\nu + g_S(k^2) k_\mu] \tau^{(\pm)} \psi . \tag{4.12}$$

Eqs. (4.10) and (4.12) indicate that the isovector component of the electromagnetic current and the weak vector current are identical in structure. This similarity leads us to the CVC hypothesis, which states that the weak hadronic vector cur-

rent, its Hermitian conjugate and the isovector component of the electromagnetic current form a single isospin triplet of conserved currents. It follows that, in the zero momentum transfer limit

$$g_V(k^2 \rightarrow 0) = F_1^V(k^2 \rightarrow 0) = 1 . \quad (4.13)$$

Thus, the vector coupling constant is always the same, independent of the nuclear medium in which the decay occurs. In section 4.2.1.5 we show the remarkable experimental success of the CVC hypothesis.

4.2.1.2 Isospin symmetry breaking corrections

For a superallowed Fermi decay, if the parent and the daughter states were perfect analogs of each other, then the Fermi matrix element would be model independent and given by

$$|M_F|^2 = [T(T + 1) - T_{3i}T_{3f}]\delta_{if} . \quad (4.14)$$

However, analog symmetry is broken due to charge-dependent forces between the nucleons. Such *isospin symmetry breaking* effects are of the order of 1% for $T = 1 \rightarrow T = 1$ transitions and reflect small differences between the initial and the final state wavefunctions (depending on the structure of the nucleus of interest). This reduces the strength of the Fermi transition to the 0^+ state, such that, the Fermi matrix element requires a theoretically calculated charge-dependent correction δ_C

$$|M_F|^2 \implies |M_F|^2(1 - \delta_C) . \quad (4.15)$$

The isospin breaking correction, δ_C , is composed of two different components. One arises due to configuration mixing with other 0^+ states in both the parent and the daughter nuclei (denoted by δ_{CM}), while the other arises due to differences in the single-particle neutron and proton radial wavefunctions, which cause the radial overlap integral between the parent and the daughter nucleus to be less than unity (denoted by δ_{RO}). Over the years, there have been many independent theoretical calculations of δ_C for superallowed Fermi emitters. Towner and Hardy [50] used shell model calculations to determine δ_{CM} and Woods-Saxon radial wavefunctions to obtain δ_{RO} . Ormand and Brown used a similar shell-model scheme as Ref. [50] to obtain δ_{CM} and self-consistent Hartree-Fock calculations using Skyrme-type interactions to calculate δ_{RO} for various nuclei [51]. Sagawa, Van Giai, and Suzuki [52] have added RPA calculations to microscopic Hartree-Fock calculations to obtain δ_C for various nuclei and Navrátil, Barrett, and Ormand [53] have calculated δ_C for the ^{10}C case using a large-basis shell model calculation. For all the cases calculated so far, the radial overlap corrections (δ_{RO}) are known to be much larger than the configuration mixing corrections (δ_{CM}) [50].

4.2.1.3 Radiative corrections

Additional radiative corrections are required for such weak processes because of the possible emission and absorption of virtual photons by the charged particles involved in the weak decay. Such radiative corrections are composed of a transition-dependent term δ_R and a transition-independent term Δ_R^V . The transition dependent term is further divided into δ'_R , which is independent of nuclear structure, and δ_{NS} , which is structure dependent. The structure independent

terms are written as

$$\delta'_R = \frac{\alpha}{2\pi} [\bar{g}(E_0) + \delta_2 + \delta_3] \quad (4.16)$$

$$\Delta_R^V = \frac{\alpha}{2\pi} [4 \ln(m_Z/m_p) + \ln(mp/m_A) + 2C_{\text{Born}}] + \dots \quad (4.17)$$

In the above equations, E_0 is the beta end-point energy, m_Z is the Z-boson mass, m_p is the proton mass, m_A is the A_1 -meson mass, and δ_2 and δ_3 are higher-order QED corrections. $\bar{g}(E_0)$ is the average of the energy dependent function derived by Sirlin [54] and C_{Born} arises from axial-vector photonic contributions of the order of the fine structure constant [50].

The nuclear structure dependent corrections, δ_{NS} , have been calculated for a wide range of nuclei that decay via superallowed transitions using varying choices of effective interactions and shell model spaces [50].

These radiative corrections are incorporated in Eq. (4.9) such that

$$G_V^2 \implies G_V^2(1 + \Delta_R^V) . \quad (4.18)$$

$$f \implies f(1 + \delta_R) , \quad (4.19)$$

where

$$\delta_R = \delta'_R + \delta_{NS} . \quad (4.20)$$

4.2.1.4 The corrected ft value

The arguments presented above lead us to define a *corrected* ft value for a superallowed transition

$$\mathcal{F}t \equiv ft(1 + \delta'_R)(1 + \delta_{NS} - \delta_C) = \frac{K}{|M_F|^2 G_V^2 (1 + \Delta_R^V)} . \quad (4.21)$$

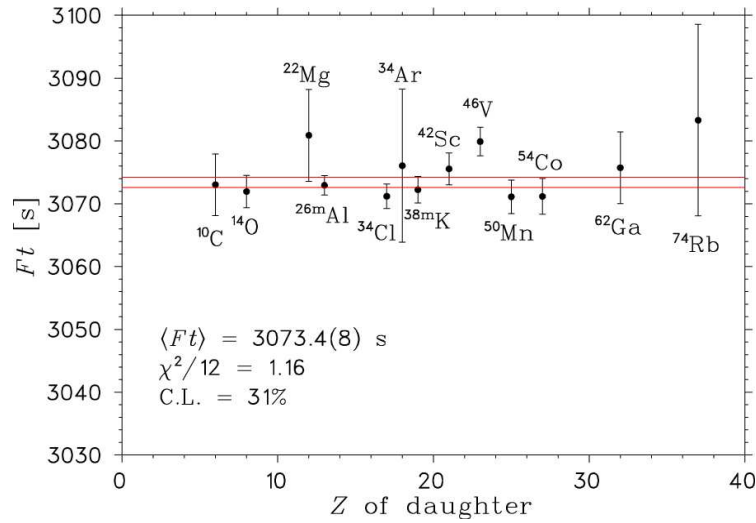


Figure 4.2. Corrected ft values for the most precisely measured $T = 1$ superallowed beta emitters.

If the CVC were true, this corrected ft value should be a constant for all superallowed transitions that occur between analog states of a given isospin T . The CVC hypothesis can thus be tested stringently by accurate measurements of the ft values of various superallowed decays and precise determinations of the theoretical corrections involved.

4.2.1.5 Experimental tests of the CVC hypothesis

The ft values of many $T = 1$ superallowed emitters have been measured accurately over an extended period of time [55]. This provides a stringent test of the CVC hypothesis. Figure 4.2 shows the phenomenal success of the CVC hypothesis; the data provides experimental verification of the CVC hypothesis to one part in 3×10^{-4} .

4.2.1.6 Determination of V_{ud} from superallowed Fermi decays

With a mutually consistent set of $\mathcal{F}t$ values for various cases, their average value can be used to determine the vector coupling constant G_V . For the weak decays of quarks, this vector coupling constant is related to the universal weak interaction coupling constant G_F by:

$$G_V = G_F V_{ud} g_V(k^2 \rightarrow 0) \quad (4.22)$$

where the V_{ud} factor is included for a semi-leptonic decay due to Cabibbo mixing. Since G_F is very well known from the muon lifetime ($G_F = 1.16637(1) \times 10^{-5}$ GeV⁻² [42]), and $g_V(k^2 \rightarrow 0) = 1$, V_{ud} can be obtained from the $\overline{\mathcal{F}t}$ value for the known $T = 1$ cases

$$|V_{ud}|^2 = \frac{K}{2G_F^2(1 + \Delta_R^V)\overline{\mathcal{F}t}}. \quad (4.23)$$

4.2.2 Neutron and pion decays

V_{ud} can also be obtained from the decay of the free neutron and the pion. We explain briefly the advantages and the limitations of these two methods to obtain V_{ud} .

Neutron beta decay has an advantage over nuclear beta decays because of the structural simplicity of the neutron. There are no complicated nuclear structure dependent corrections or renormalization effects of nuclear medium involved in neutron decay. However, this has both vector and axial-vector contributions. Unlike the vector current, the axial-vector current is only partially conserved (PCAC) [56], which requires two measurements to obtain V_{ud} . One is the neutron lifetime and the other is λ , the ratio of the axial-vector and vector effective coupling con-

starts,

$$\lambda = G_A/G_V = \frac{G_F V_{ud} g_A}{G_F V_{ud}}, \quad (4.24)$$

which can be obtained by a correlation measurement to separate the vector and axial-vector components [57].

Pion beta decay has advantages over both neutron and nuclear beta decay because there exist no structure dependent corrections like the neutron, however, unlike the neutron, the interaction current is purely a vector current. Unfortunately, the branch for the decay is extremely small ($\approx 10^{-8}$) [58], which results in severe experimental limitations.

4.3 Present status of CKM unitarity

Although the theoretically calculated corrections are small for pion and neutron beta decays, they are limited by experimental uncertainties. The most precise value for V_{ud} is obtained from superallowed nuclear beta decays. Figure 4.3 shows a comparison of the uncertainties involved presently in obtaining V_{ud} using these three methods. The uncertainty in V_{ud} was further reduced by a recent precise determination of the radiative correction factor by Marciano and Sirlin [59], such that

$$|V_{ud}| = 0.97377 \pm 0.00027. \quad (4.25)$$

Previously, on using ft values of various superallowed beta transitions, there were indications that CKM unitarity was violated at the 2.4σ level [60]. Two recent measurements, the branching ratios of $K^+ \rightarrow \pi^0 e^+ \nu_e (K_{e3}^+)$ and $K_L \rightarrow \pi^\pm e^\mp \nu_e (K_{e3}^0)$ yield higher values for V_{us} than previously quoted [61, 62]. The

$0^+ \rightarrow 0^+$ decays

$$|V_{ud}| = 0.9738(3)$$

PRL **96** 2006 032002

$n \rightarrow p e^- \bar{\nu}$

$$|V_{ud}| = 0.9746(19)$$

PDG 2006

$\pi^+ \rightarrow \pi^0 e^+ \nu$

$$|V_{ud}| = 0.9728(30)$$

PRL **93** (2004) 181803

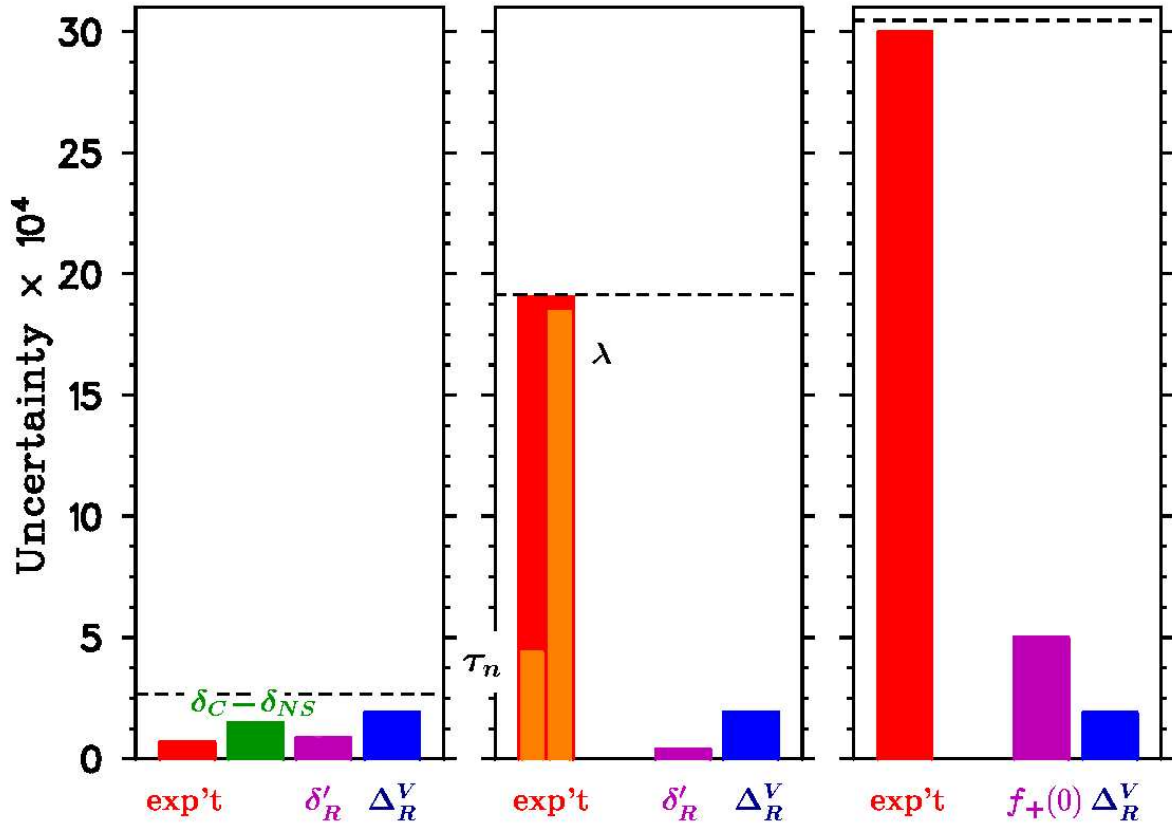


Figure 4.3. V_{ud} from the three different methods. The contribution of the uncertainties are shown.

Particle Data Group [42] adopts these recent values to obtain

$$|V_{us}| = 0.2257 \pm 0.0021 . \quad (4.26)$$

The value of V_{ub} is the smallest in the first row of the CKM matrix and is obtained from B decays. The particle data group quoted value [42] for V_{ub} is

$$|V_{ub}| = (4.31 \pm 0.30) \times 10^{-3} . \quad (4.27)$$

The newly evaluated values shown in Eqs. (4.25), (4.26) and (4.27) restore unitarity such that

$$|V_{ud}|^2 + |V_{us}|^2 + |V_{ub}|^2 = 0.9992 \pm 0.0011 . \quad (4.28)$$

However, the development of novel radioactive ion trapping methods has inspired many research groups to investigate the previously determined Q_{EC} values for various superallowed decays via direct mass measurements with high precision. In a recent measurement of the Q_{EC} value for the case of ^{46}Va , the measured masses yielded a value ≈ 2 keV higher than the value quoted in previous compilations [63]. If the Q_{EC} values of all the other precisely measured superallowed cases were shifted by approximately the same amount, then the average $\mathcal{F}t$ value in Eq. (4.23) would be higher, which would resurrect the non-unitarity problem.

4.4 The beta decay of ^{32}Ar

The superallowed beta decay of ^{32}Ar is an interesting case to study. The beta-decay is followed by isospin-forbidden delayed proton emission $\approx 93\%$ of

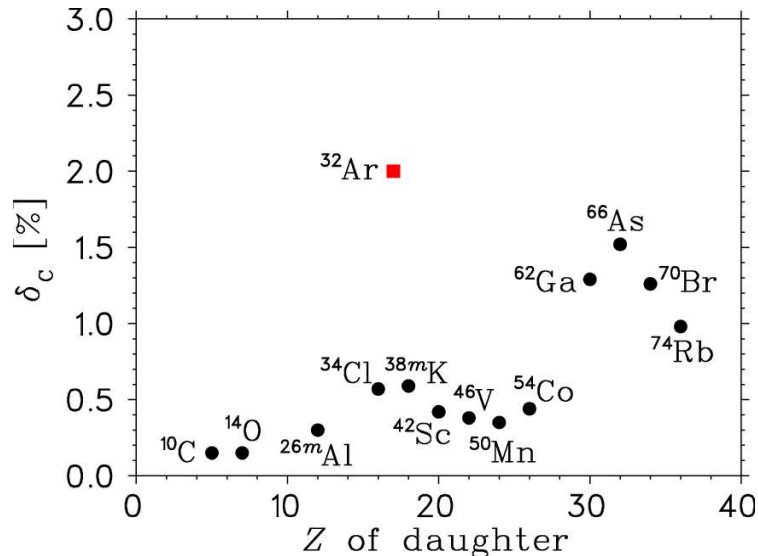


Figure 4.4. Predicted coulomb corrections for a number of superallowed decays using the Hartree Fock calculations of Ref. [51]

the time, which makes the superallowed branch easier to determine with high accuracy. Also, for the case of ^{32}Ar , δ_C is calculated to be much larger than most of the other superallowed beta emitters that have been experimentally studied ($\delta_C = 2.0 \pm 0.4\%$) [64]. These Coulomb corrections are larger for ^{32}Ar because of the loose binding of $d_{3/2}$ and $s_{1/2}$ proton states compared to the tight binding of the corresponding neutron states. Thus, the tail of the radial wavefunction for the protons extends further than that of the neutrons, which leads to a larger δ_{RO} correction. Figure 4.4 compares the calculated δ_C values of a number of superallowed decays to ^{32}Ar .

The isospin-breaking correction for ^{32}Ar can be decomposed into $\delta_{CM} = 0.6\%$ and $\delta_{RO} = 1.4\%$ [64]. Since the corrections are large for this case, it is interesting to check the calculated corrections by measuring the δ_C value for ^{32}Ar superallowed decay. In addition, it must also be noted that the δ_{CM} correction factor is

highly model dependent; it is inversely proportional to the difference in excitation energies as shown in Eq. (3.10). This model dependence is reduced by constraining the strength of the charge dependent interaction to reproduce the b and c IMME coefficients for the specific isobaric multiplet involved in the Fermi beta decay [50].

A previous measurement of the $e^+ - \nu$ correlation in the $0^+ \rightarrow 0^+$ decay of ^{32}Ar [14] through detailed analysis of the shape of the delayed-proton spectrum provides information to measure δ_{CM} for this particular case. Isospin mixing with non-analog 0^+ states would reduce the Fermi strength to the analog state and permit vector β branches to these non-analog states. There is work in progress to determine δ_{CM} experimentally by identifying such transitions from the proton spectrum and from knowledge of the $e^+ - \nu$ correlation [65].

4.5 ^{32}Ar superallowed decay: What needs to be known?

The half-life for the ^{32}Ar beta decay is already known to 0.2% [65], while a precision measurement of the ^{32}Ar mass [18] yields a Q_{EC} value known to ≈ 2.5 keV, or $\approx 0.04\%$. The absolute branch for the superallowed decay, however, is only known to $\approx 13\%$ [33]. An improved high precision measurement of the branch is the only remaining requirement for a meaningful ft value determination for ^{32}Ar β decay.

Figure 4.5 shows a simplified decay scheme for ^{32}Ar . The $J^\pi = 0^+, T = 2$ state in the daughter ^{32}Cl nucleus is mainly unbound to proton emission. However, $\approx 7\%$ of the time, the daughter state decays via γ emission. An accurate determination of the superallowed branch therefore requires precise measurements of the delayed proton and γ branches respectively. For the γ -ray detection efficiencies, an intrinsic calibration can be done using the subsequent beta decay of the ^{32}Cl

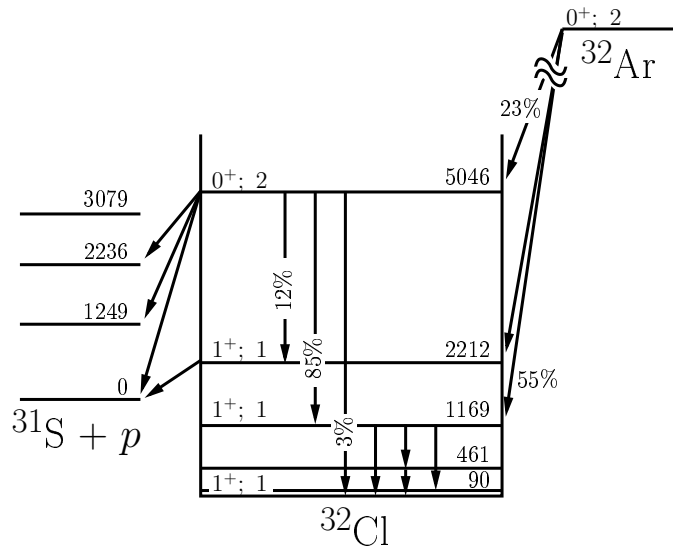


Figure 4.5. Simplified decay scheme of ^{32}Ar . The delayed proton emission and some of the levels that γ decay are shown.

daughter nucleus and known values of delayed γ yields from ^{32}Cl β -decay. This minimizes systematic uncertainties associated with the geometrical size and the distribution of the source. In order to determine the γ branches with high precision to make a meaningful test of the calculated δ_C corrections, it is important to know the delayed γ yields from ^{32}Cl with accuracies of $\approx 1 - 2\%$. The following two chapters explain the experimental procedure to measure the γ yields from ^{32}Cl β -decay and the determination of the superallowed branch for ^{32}Ar β -decay to test the calculated isospin-symmetry breaking corrections.

CHAPTER 5

DELAYED GAMMA YIELDS FROM ^{32}Cl BETA DECAY

In this chapter we describe the experimental details and preliminary results from an experiment at the Cyclotron Institute of Texas A&M University to obtain the delayed γ yields from the β -decay of ^{32}Cl .

5.1 Introduction

Prior to the work described in this chapter, the γ yields following the β -decay of ^{32}Cl were determined using the $^{32}\text{S}(p, n)$ reaction and a rabbit system [66]. This result was limited by the efficiency calibration of the γ -ray detector, and the yields were known to $\lesssim 10\%$. As explained previously (§ 4.5), an improved determination of the γ yields from the decay of ^{32}Cl is essential to make a meaningful test of the calculated isospin-symmetry breaking corrections for the superallowed Fermi decay of ^{32}Ar . Figure 5.1 shows the decay scheme for ^{32}Cl . The β -decay of ^{32}Cl feeds states in ^{32}S , which subsequently de-excite via γ emission. Our measurement reports revised determinations of the absolute β and γ yields from ^{32}Cl decay. We remeasured the γ intensities to $\leq 0.3\%$ using a radioactive ^{32}Cl beam, a fast tape-transport system and an extremely well-characterized HPGe detector.

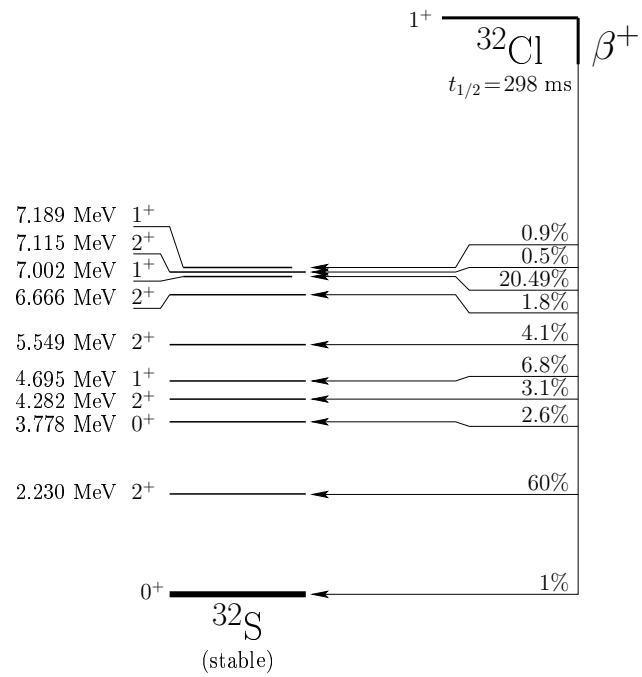


Figure 5.1. Decay scheme of ^{32}Cl . The beta branches are from Ref. [66].

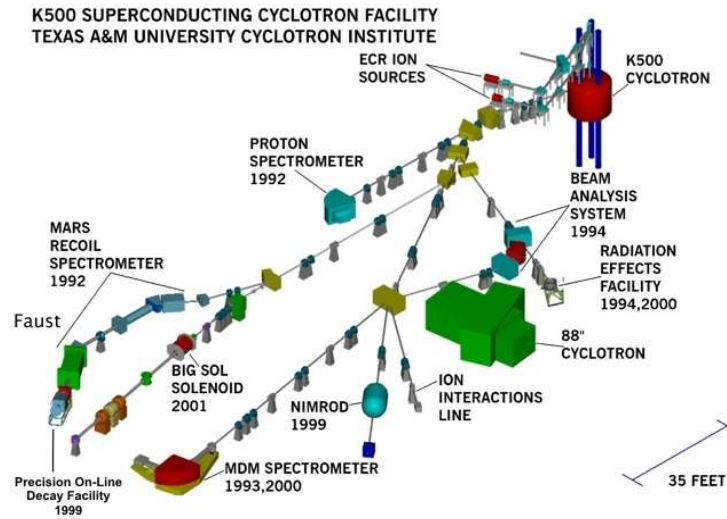


Figure 5.2. Schematic layout of the Cyclotron Institute laboratory.

5.2 Experimental details

5.2.1 The MARS spectrometer: Beam production

The measurement was carried out using the recoil spectrometer (MARS) at the Cyclotron Institute at Texas A&M University. Figure 5.2 shows a schematic of the facilities available at the site, and Figure 5.3 shows a schematic view of MARS. A description of the spectrometer is explained in detail in Ref. [67]. A primary beam of ^{32}S was produced by an ECR ion source and injected into the K500 superconducting cyclotron. The $\approx 400 \text{ nA}$ ^{32}S beam exited the K500 cyclotron at $\approx 24.8 \text{ MeV/A}$ and was directed towards the MARS recoil spectrometer. It was passed through magnets SW1 and SW2 (shown in Figure 5.3) and impinged on a liquid N_2 cooled H_2 gas target at 1.4 atm, where the entrance and exit windows of the gas cell were made of $\approx 5 \mu\text{m}$ Havar foil. The secondary beam of ^{32}Cl was produced in the gas cell via the inverse kinematic transfer reaction $^1\text{H}(^{32}\text{S}, n)^{32}\text{Cl}$.

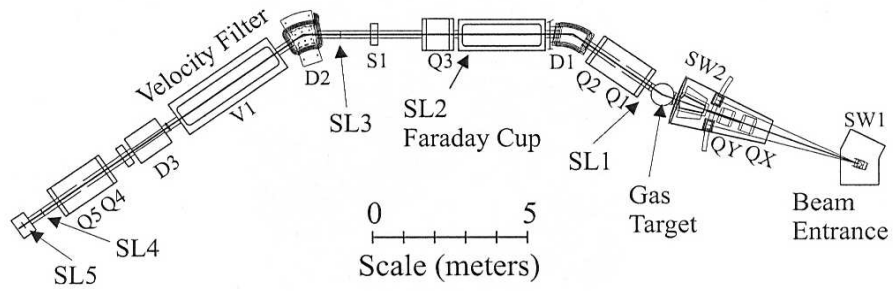


Figure 5.3. Schematic layout of the MARS recoil spectrometer.

Preliminary excitation function data indicated the reaction cross section to be ≈ 3 mb for the aforementioned energy [68].

The reaction products were spatially separated in the following manner: First, the beam was passed through the two quadrupole magnets Q1 and Q2 and then dispersed horizontally using the dipole magnet D1, which in combination with Q3 and D2 produced an achromatic beam that was sent into a velocity filter (V1). Then, the beam was dispersed vertically using the dipole D3, which together with the quadrupoles Q4 and Q5 produced an M/Q focus at the extraction slits of the MARS focal plane [69].

Contaminants in the beam were identified using a position-sensitive Si strip-detector (ΔE) and a 4-fold segmented Si detector (E) that were placed downstream from the MARS focal plane. The purity of the ^{32}Cl beam ($t_{1/2} = 298$ ms) was $\approx 88\%$, the only significant contaminants being ^{30}S ($t_{1/2} = 1.178$ s) and ^{31}S ($t_{1/2} = 2.572$ s). Figure 5.4 shows a two-dimensional spectrum from the first detector as a function of position. During data acquisition most of the ^{31}S contribution was minimized using the slits SL5.

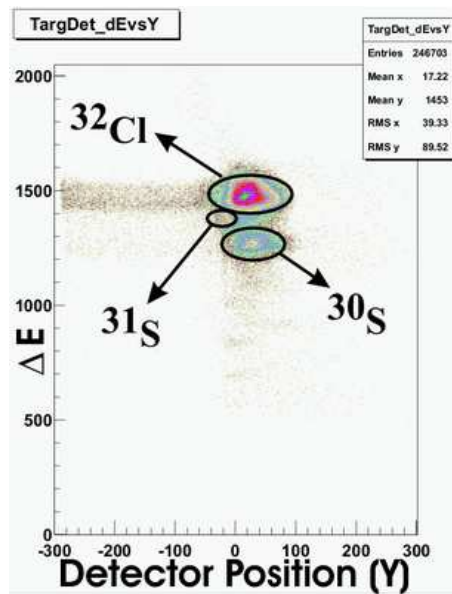


Figure 5.4. Ion identification using the first strip detector. The only significant contaminant is ^{30}S .

5.2.2 The fast tape-transport system: Data acquisition

The fast tape-transport system used for the measurement is shown in Figure 5.5. The ^{32}Cl beam from MARS, containing $\approx 2 \times 10^5$ atoms/s, exited the vacuum system through a $50\text{-}\mu\text{m}$ -thick Kapton window and then passed through a 0.3-mm -thick BC-404 scintillator and a series of degraders before finally stopping in a $75\text{-}\mu\text{m}$ -thick aluminized Mylar tape that is a part of the tape-transport system. Since the impurities in the beam had different ranges compared to ^{32}Cl , most of these impurities were not collected in the tape. The optimal set of degraders were later determined to consist of one 0.5 mils thick Al foil and a ‘dummy’ aluminized Mylar tape.

In a typical tape cycle, ^{32}Cl was collected in the tape for 0.8 seconds after which the accelerator beam was interrupted for a few μs by shifting the phase

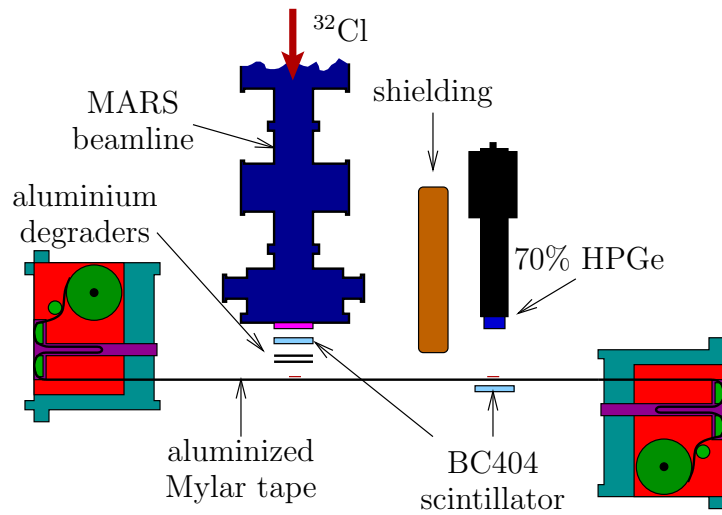


Figure 5.5. The fast tape-transport system at TAMU for precision measurements.

of one of the cyclotron dees off resonance. The tape-transport system was then triggered to move the radioactivity to a shielded counting station 90 cm away in ≈ 180 ms where data were acquired for 1 second (see Figure 5.5). The radioactivity in the tape was positioned between a 70% HPGe γ -ray detector and a 1-mm-thick BC-404 plastic scintillator to detect β particles. The former was located 15.1 cm away from the sample, while the latter was positioned only 5 mm away. For each tape cycle, the $\beta - \gamma$ coincidence data were stored event-by-event. The β and the γ -ray energies, the coincidence time between them and the time of the event relative to the beginning of the cycle were recorded. Each cycle was clock controlled and repeated continuously. The total number of beta singles events and the total number of heavy ions from the MARS spectrometer (that were detected by the first scintillator) for each cycle were determined from a scaler and recorded on a run by run basis.

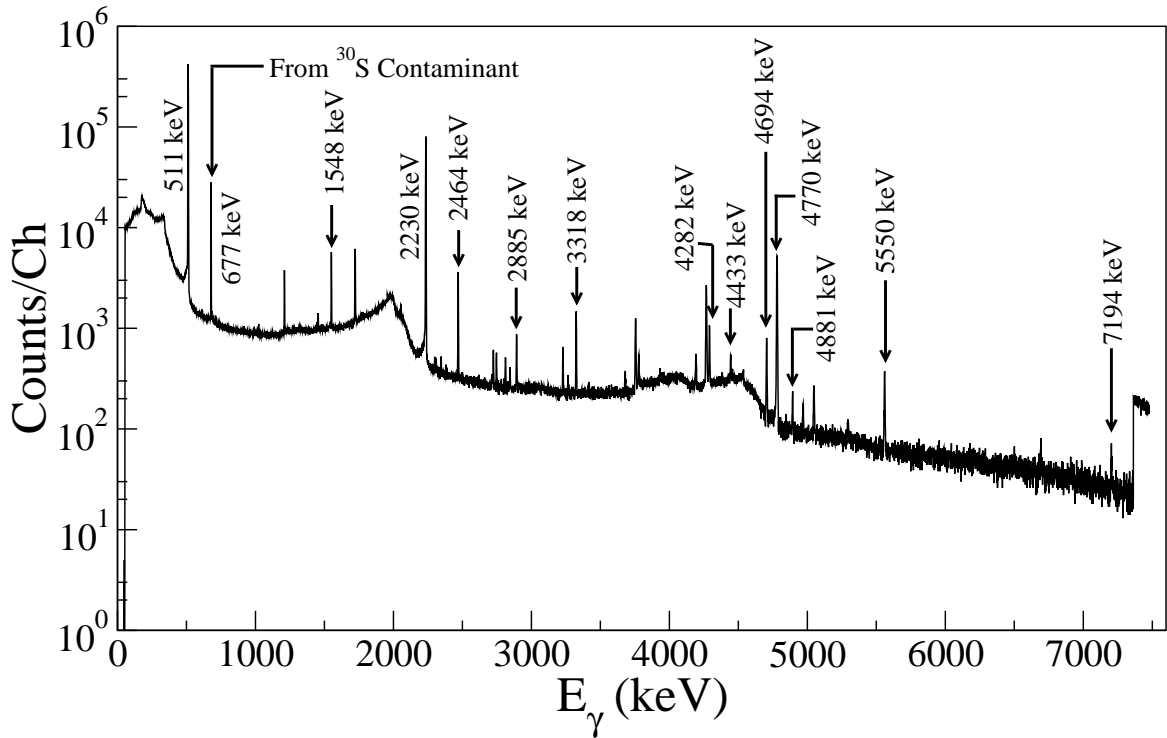


Figure 5.6. Delayed γ -ray spectrum following ^{32}Cl decay in coincidence with β particles.

5.3 Data analysis

Figure 5.6 shows the γ -ray spectrum from the experiment. These data were taken in coincidence with signals from the β counter to reduce room background. Almost all the peaks are associated with ^{32}Cl β -decay. We identified 8 new γ transitions from ^{32}Cl β -decay that were not previously reported. However, two γ -rays that were previously reported [32] with weak branches at energies $E_\gamma = 2833$ keV and $E_\gamma = 7115$ keV were absent from the spectrum. The 677 keV peak corresponds to a transition in ^{30}P due to the β -decay of ^{30}S contaminant nuclei. We also observed weak γ -ray peaks at $E_\gamma = 1266$ keV and E_γ at 1779 keV which indicate that small traces of ^{31}S and ^{28}P were present as additional impurities in

the sample.

5.3.1 Efficiency Calibration

The γ -ray detection efficiency calibration was fundamental to our measurement. The Ge detector used for this experiment was meticulously calibrated over a period of 5 years using both radioactive sources and a Monte Carlo photon transport code called CYLTRAN [70]. This was done through a series of steps: First, the absolute and the relative efficiencies were determined over a range of γ -ray energies using the high purity radioactive sources with extremely well-known activities known to $\approx 3\%$ or below. Then, the detector dimensions were determined independently of the factory specifications using various radioactive sources⁵. The measured parameters of the Ge detector were then used as inputs to the Monte Carlo code to obtain the efficiencies from the simulation. Finally, the dead-layer parameters of the detector were varied in the Monte Carlo simulation to obtain agreement with the measured values. Table 5.1 shows the calculated efficiencies for the detector over the energy range of interest, obtained using the method explained above.

These calculated efficiencies were fitted to a polynomial of the form

$$\ln \eta_i(E_{\gamma_i}) = \sum_{j=0}^3 a_j (\ln E_{\gamma_i})^j, \quad (5.1)$$

to obtain the efficiencies at the γ -ray energies of interest. Figure 5.7 shows the fit to the measured efficiencies.

⁵An independent x-ray scan of the detector revealed significant differences with the factory quoted specifications.

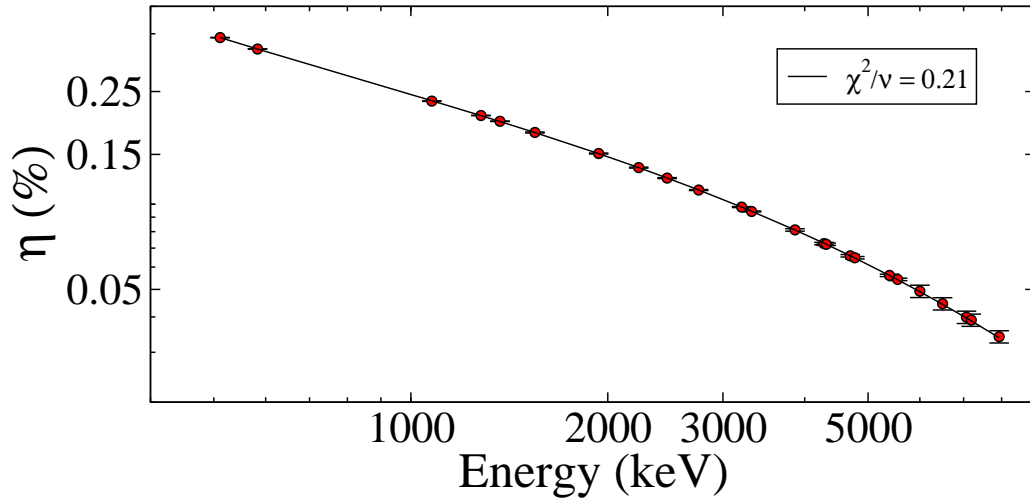


Figure 5.7. γ -ray detection efficiencies and the corresponding polynomial fit.

TABLE 5.1

GAMMA-RAY DETECTION EFFICIENCIES AT 15.1 CM (FROM REF. [70].)

Energy (keV)	Efficiency (%)
511.0	0.38769(78)
583.03	0.35339(71)
1076.9	0.23130(46)
1279.9	0.20579(41)
1368.6	0.19634(39)
1548.0	0.17920(72)
1936.9	0.15111(60)

TABLE 5.1

Continued

Energy (keV)	Efficiency (%)
2230.3	0.13471(54)
2465.1	0.12369(49)
2754.0	0.11225(45)
3203.87	0.09770(39)
3318.8	0.09426(38)
3866.2	0.08117(81)
4281.5	0.07263(73)
4316.0	0.07223(72)
4695.4	0.06574(66)
4772.2	0.06471(65)
5392.7	0.05606(56)
5548.9	0.05427(54)
6000.0	0.0493(25)
6500.0	0.0445(22)
7069.5	0.0400(20)
7189.7	0.0390(19)
7930.9	0.0341(17)

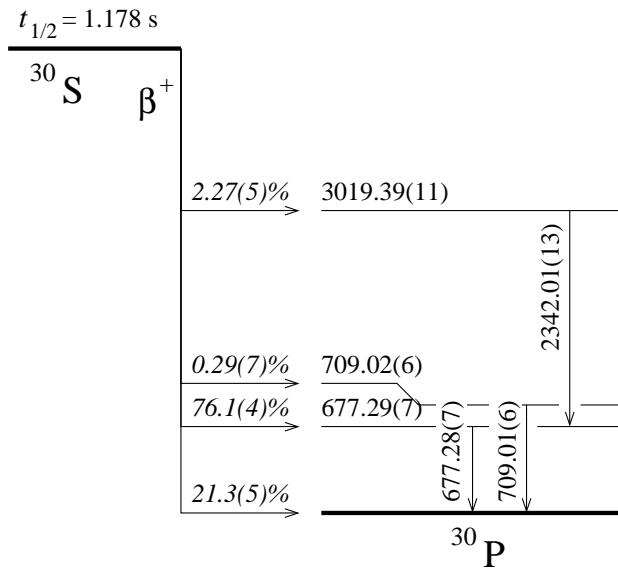


Figure 5.8. Decay scheme of the ^{30}S contaminant.

5.3.2 Determination of the γ -yields

One important consideration that had to be accounted for before obtaining the intensities from the data was the consistency of the position of the radioactivity in each tape cycle. Although the tape-transport system was known to be consistent in positioning the radioactivity to within $\pm 3 \text{ mm}$ for each cycle, larger deviations did occur for a number of cycles due to mechanical fluctuations. Such *bad* cycles were identified by registering the number of heavy ions that were detected in the first scintillator (located in front of the Aluminium degraders) and calculating the ratio of heavy ions to β singles. Any anomalously high ratio indicated deviations in tape position and a low ratio indicated fluctuations in the beam tune. Such cycles were labelled as *bad* cycles and not used for data analysis. In addition, tight timing cuts were made in each cycle ($0.008 \text{ s} \leq t \leq 0.9 \text{ s}$) to minimize contributions from the long-lived contaminants.

The γ -ray intensities following the β -decay of ^{32}Cl were obtained using two different methods. In the first method, the intensities were obtained as

$$Y(i) = \frac{N_{\beta\gamma}(i)}{\eta(i)N_{\beta}(^{32}\text{Cl})} . \quad (5.2)$$

In the above equation $N_{\beta\gamma}$ represents the photo-peak area of a particular γ -ray, $N_{\beta}(^{32}\text{Cl})$ is the number of β -singles events from ^{32}Cl decay and $\eta(i)$ is the efficiency of the Ge detector at that energy. This method of extracting the γ -ray intensities assumes negligible summing corrections (§ 5.5) and a constant β detection efficiency over a range of β end-point energies.

The photo-peak areas of the γ -ray peaks were obtained using the lineshape fit explained before (§ 3.4), with an additional high-energy tail to account for pile-up effects.

The dominant source of uncertainties in obtaining the yields using Eq. (5.2) comes from $N_{\beta}(^{32}\text{Cl})$. This is because the total number of β -singles registered by the scintillator were determined by a scaler to avoid significant dead-time effects. This number had to be corrected for the vetoed cycles, the timing cuts within each cycle and the betas from the contaminants. The contaminant betas could be deduced using knowledge of the β and the γ branches of the contaminant nucleus. For example, Figure 5.8 shows the decay scheme of ^{30}S , which contributes significantly to beam impurities. Since the β and γ branches for ^{30}S decay were reasonably well-known [33], the total number of ^{30}S contaminant nuclei were extracted using the 677 keV photo-peak areas and a relation similar to Eq. (5.2). We determined that $\approx 6\%$ of our activity was contaminated by ^{30}S nuclei.

In the second method, the photo-peak areas were determined using the same fitting routine. For a given γ -ray with energy E_{γ} that corresponds to a transition

$E_\gamma = E_i - E_j$, this photo-peak area is given by

$$N_{ij}^{\beta\gamma} = \frac{N_\beta(^{32}\text{Cl})}{\underbrace{\sum_i \beta_i \epsilon_i}_N} \left[\beta_i \epsilon_i + \sum_{k>i} \beta_k \epsilon_k \gamma_{ki} \right] \gamma_{ij} \eta_{ij} , \quad (5.3)$$

where ϵ_i represents the beta-detection efficiency for a β particle associated with a transition to the state labelled by i , and β_i is the β branch to state i . η_{ij} denotes the γ detection efficiency for a γ -ray with energy E_γ , and γ_{ij} is the γ branch for the transition. The β detection efficiencies were obtained using a PENELOPE Monte Carlo simulation. This simulation was done over a range of β -endpoint energies assuming that the radial implantation profile of ^{32}Cl in the tape was 1 cm in diameter. The depth profile was assumed to be a Gaussian distribution extending up to the edges. The data were fit to Eq. (5.3) using the method of least squares allowing an effective normalization (N), and the β and γ branches to vary such that the photo-peak areas were reproduced. The ground state β branch was fixed to $\beta_0 = 1.0^{+0.2}_{-0.5}\%$ from a previous measurement [71].

Once the β and γ branches were determined, the γ yields were obtained using the relation

$$Y_{ij} = \left[\beta_i + \sum_{k>i} \beta_k \gamma_{ki} + \sum_{i<n<k} \beta_k \gamma_{kn} \gamma_{ni} \right] \gamma_{ij} . \quad (5.4)$$

5.4 Preliminary Results

The γ intensities obtained using the two methods explained previously agree to within uncertainties. Table 5.2 shows the yields obtained by using the second method. All the intensities agree with the values quoted by Détraz *et al.* with much higher precision, except the 7188 keV γ -ray, which is lower by 2.5σ . The β

branches are shown in Table 5.3.

TABLE 5.2

GAMMA-RAY INTENSITIES FROM THE BETA-DECAY OF ^{32}Cl

E_γ (keV)	Assignment $E_i \rightarrow E_j$	Y_{ij} (%)	
		Previous work [66]	This work
1452	7001 \rightarrow 5549	...	0.27(2)
1548	3778 \rightarrow 2231	3.6(6)	3.04(5)
1770	5549 \rightarrow 3778	...	0.13(2)
1970	6666 \rightarrow 4695	...	0.18(5)
2051	4282 \rightarrow 2231	...	0.39(4)
2230	2231 \rightarrow 0	92.0(4.0)	89.6(3)
2305	7001 \rightarrow 4695	...	0.12(2)
2464	4695 \rightarrow 2231	4.0(4)	4.11(4)
2719	7001 \rightarrow 4282	...	0.52(2)
2887	6666 \rightarrow 3778	1.0(4)	0.96(3)
3222	7001 \rightarrow 3778	...	0.83(2)
3318	5549 \rightarrow 2231	2.5(4)	2.39(3)
4281	4281 \rightarrow 0	2.6(1)	2.50(6)
4434	6666 \rightarrow 2231	0.8(2)	0.80(3)
4695	4695 \rightarrow 0	2.8(6)	2.42(5)
4770	7001 \rightarrow 2231	20.5(2.0)	20.22(22)
4884	7115 \rightarrow 2231	0.45(20)	0.51(2)

TABLE 5.2

Continued

E_γ (keV)	Assignment $E_i \rightarrow E_j$	Y_{ij} (%)	
		Previous work [66]	This work
4958	7190 \rightarrow 2231	...	0.31(2)
5548	5549 \rightarrow 0	1.6(3)	1.49(4)
7188	7190 \rightarrow 0	0.41(10)	0.16(2)

5.5 Other systematic effects

Other systematic effects that could affect the measurement are coincidence summing of the γ -rays⁶, the dependence of β detection efficiency on the β endpoint energy and dead-time effects. These effects were not large for this experiment. The coincidence summing corrections are estimated to be small because of the small solid angle subtended by the Ge detector. Preliminary Monte Carlo simulations using PENELOPE indicate no significant variation of the beta-detection efficiency with the endpoint energy. Since the γ -ray rate varied from 1 kHz to 5 KHz during the time data were acquired, dead-time corrections are currently being investigated.

⁶Coincidence summing occurs if two γ s from a cascade reach the detector simultaneously and are recorded as a single γ -ray with the combined energy of both.

TABLE 5.3

BETA BRANCHES FROM ^{32}Cl DECAY

Daughter state (keV)	β yield (%)	
	Previous work [66]	This work
2230	60.0(4.0)	60.28(44)
3778	2.6(8)	1.07(6)
4282	3.1(4)	2.28(8)
4695	6.8(8)	6.2(1)
5549	4.1(5)	3.76(12)
6666	1.8(5)	2.03(7)
7001	20.5(2.0)	22.0(3)
7115	0.5(2)	0.57(3)
7190	0.9(1)	0.55(5)

CHAPTER 6

SUPERALLOWED BRANCH FOR ^{32}Ar BETA DECAY

We now describe the experimental procedure to obtain the branch for the $0^+ \rightarrow 0^+$ decay of ^{32}Ar . The $T = 2$ state in the daughter ^{32}Cl nucleus decays predominantly via isospin-forbidden proton emission. However, the width of this state is only ≈ 20 eV [14, 65], which implies that the γ decays of this state cannot be neglected. The absolute superallowed branch was obtained by accurately measuring the absolute proton and γ branches following ^{32}Ar decay. Figure 6.1 is the simplified decay scheme of ^{32}Ar , shown previously in Chapter 4.

The measurement was done at the National Superconducting Cyclotron Laboratory (NSCL) by implanting a known number of ^{32}Ar ions in a silicon detector and counting their subsequent decays. The absolute beta branch for the decay was obtained by the ratio of the total number of decay products to the total number of implanted parent ions.

6.1 Experimental Setup

^{32}Ar ions were produced at NSCL at the rate of ≈ 20 s $^{-1}$ by fragmenting a 100 MeV/u $^{36}\text{Ar}^{+12}$ beam on a 470 mg/cm 2 ^9Be target. The fragments passed through the A1200 fragment separator [72] that separated ^{32}Ar ions from other nuclides created in the fragmentation process. The two dipoles of the A1200 were

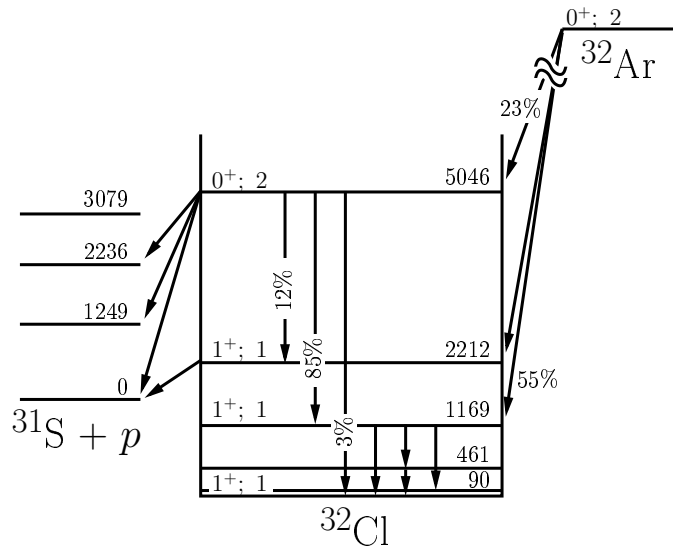


Figure 6.1. Simplified decay scheme of ^{32}Ar .

set at 2.08112 and 1.89409 T-m, respectively. Additional fragment separation was obtained using a 133-mg/cm²-Al-equivalent plastic wedge that was inserted between the two dipoles. The separated ^{32}Ar beam at ≈ 53 MeV/A left the A1200 fragment separator with a momentum spread of $\Delta p/p \approx 1\%$, after which it was passed through the Reaction Product Mass Separator (RPMS) Wien filter, which further purified the beam.

The detector array used for the measurement is shown in Figure 6.2. It consisted of a PIN silicon detector (D_1) and a stack of 3 fully depleted 450 mm²-area, 500- μm -thick silicon surface barrier detectors (D_2 , D_3 and D_4) surrounded by 5 large-volume high-purity Ge detectors. A 310- μm -thick Aluminium foil, inserted between D_1 and D_2 ensured that the incoming ^{32}Ar ions stopped in the middle of D_3 (the implantation detector). Signals from D_2 , D_3 and D_4 were processed by Canberra 2001 preamplifiers that had very low thresholds (≈ 20 keV) for detecting

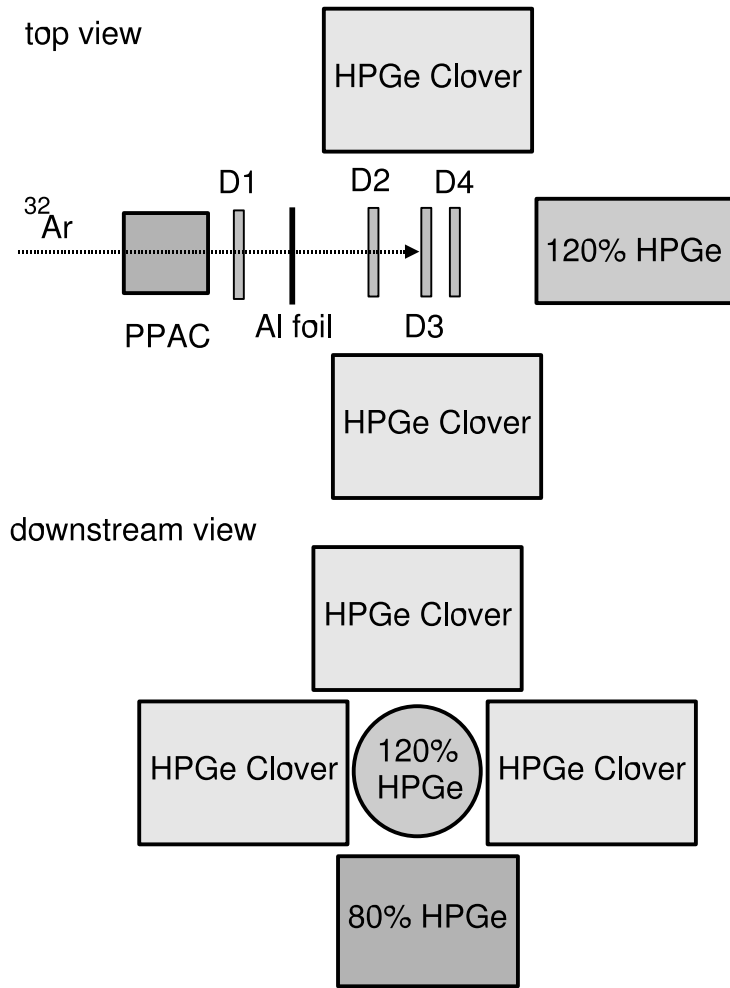


Figure 6.2. Top plus downstream views of the detector setup. The top view does not show the top and bottom Ge detectors.

β s as well as the much larger signals from the incoming heavy ions. D₁ provided energy loss and time-of-flight information that was used for identifying incoming fragments. The energy loss in D₂ in conjunction with the energy deposited in D₃ gave an independent identification of the stopping ions that was used to determine the actual number of ions implanted in D₃. The implantation detector also served as a delayed proton counter. D₂ and D₄ were used to reject fast light charged particles and served also as β detectors. D₄ also helped reject ³²Ar ions that did not stop in D₃. The trigger consisted of any event in detectors D₂, D₃ or D₄ resulting in a β detection efficiency of $\approx 98.6 \pm 1.4\%$. D₄ was located at ≈ 1.0 mm from D₃, while D₂ was located at ≈ 8.3 mm from D₃. The array of high-purity Ge detectors consisted of three 4-fold segmented clover detectors [73] G₁, G₂ and G₃, each with efficiencies of $\approx 120\%$, and 2 monolithic crystals, G₄ and G₅, with efficiencies of 80% and 120%, respectively.

6.2 Determination of the number of implanted ³²Ar ions

6.2.1 Ion identification

We separated events into *incoming ions* and *decays*. The former consisted of events in which D₁, D₂ and D₃ registered energies larger than ≈ 0.1 GeV, and no energy was registered by D₄. *Decay* events left between 40 keV and 15 MeV in D₂, D₃ or D₄ and deposited no energy in D₁. *Incoming ions* were further classified in 3 categories as shown in Figure 6.3. *Good* ions stopped in D₃ and were clearly identified as ³²Ar ions in both the E_1 vs. TOF₁ (energy and time of flight measured with D₁) and in the E_3 vs. E_2 spectra. Ions not guaranteed to be ³²Ar ions arrived in *buffer* regions in the particle identification spectra. The buffer regions were defined such that these regions were large enough so that no ³²Ar

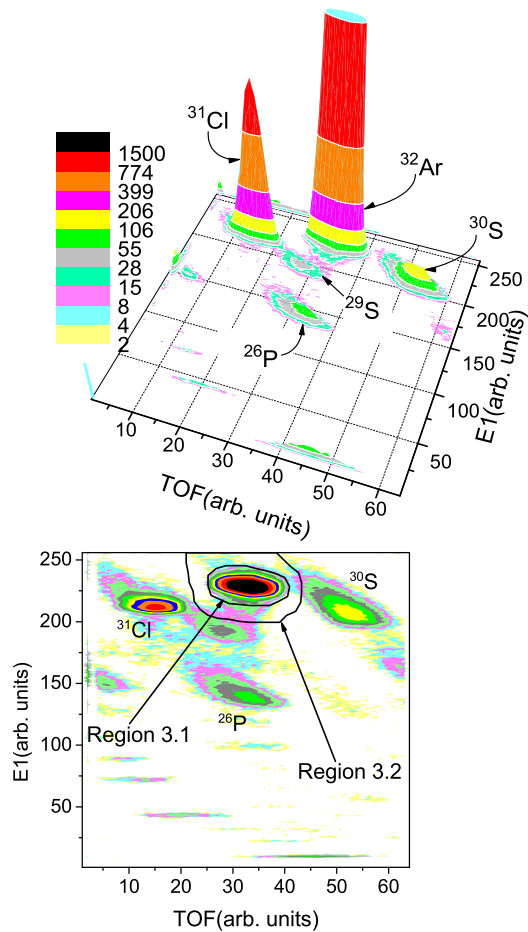


Figure 6.3. E_1 vs. TOF_1 spectrum from a single run. Top: 3d spectrum where the ^{32}Ar group has been truncated to show the other groups more clearly. Bottom: vertical projection showing Region 3.1 (*good* region), which contains the main ^{32}Ar group, and Region 3.2 (*buffer* region), which contained mostly ambiguous ions.

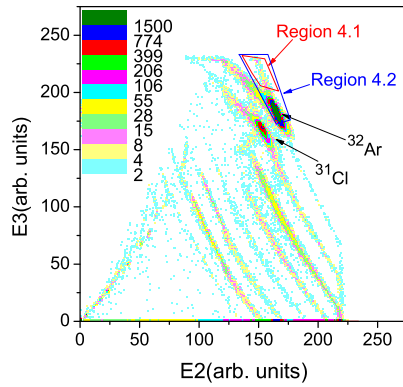


Figure 6.4. E_3 vs. E_2 spectrum of events shown in Figure 6.3. Region 4.1 was defined to show that these events arise from a high-energy tail of the beam (see text and Figure 6.6) and used to define Region 6.1; the larger Region 4.2 is used in conjunction with Region 6.1 to ensure all high-energy tail events are labelled *ambiguous*.

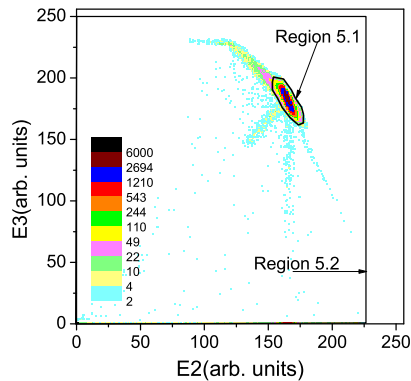


Figure 6.5. E_3 vs. E_2 showing only events on Region 3.1 in Figure 6.3. Region 5.1 contains *good* ^{32}Ar ions and contains 61 times more events than Region 5.2. Region 5.2 is exclusive of Region 5.1 and contains *ambiguous* ions.

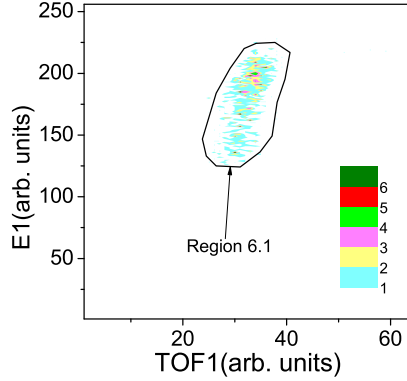


Figure 6.6. E_1 versus TOF_1 spectrum of events in Region 4.1 of Figure 6.4. Once defined, events that were in both Region 6.1 and Region 4.2 were labelled *ambiguous* to avoid high-energy tails in the beam profile.

ion whose proton emissions could have been detected by D_3 could lie outside the union of the *good* and *buffer* regions. The ions in the *buffer* regions were labelled as *ambiguous* ions. *Contaminant* ions were all those ions not contained in either of the two regions. While counting the number of implanted ions and their decays, all the *ambiguous* ions were rejected, and a 500 ms software dead-time (about five ^{32}Ar half-lives) was imposed on counting either incoming ions or proton decays following the implantation of an *ambiguous* ion. If a successive *ambiguous* ion was detected within 500 ms of the previous *ambiguous* ion, the clock was reset to impose the deadtime for another 500 ms. Incoming ions were identified with the help of the code LISE [74]. Figure 6.3 shows the E_1 vs. TOF_1 spectrum; the area labelled “Region 3.1” contained mainly ^{32}Ar ions, not clearly separated from contaminants. Region 3.2, which surrounds the main ^{32}Ar group in Region 3.1, mostly contained *ambiguous* ions. Figure 6.4 shows the E_3 vs. E_2 spectrum of all

events in Figure 6.3. Figure 6.5 is similar to Figure 6.4 but contains only events in Region 3.1 of Figure 6.3. Region 5.1 of Figure 6.5 contains the *good* ^{32}Ar ions; the remaining events are ^{32}Ar ions that either reacted before reaching D_3 or whose full energy was not detected in D_3 .

Some features in the particle identification spectra are as follows:

- *Saturation effects.* In Figure 6.4 the horizontal line in the high E_3 region and vertical line in the high E_2 region are due to saturation of the preamplifier signals. To obtain the best possible energy resolution, a single preamplifier was used on each detector; therefore the preamplifiers had to process an unusually wide range of energies.
- *Events in Region 4.1 of Figure 6.4.* Figure 6.6 shows the E_1 vs. TOF_1 spectrum of events in Region 4.1, showing that these events originate due to a high-energy tail in the beam profile. These ions deposited energy in D_1 and D_2 and more energy in D_3 than the *good* ^{32}Ar ions.
- *Vertical line descending from the main ^{32}Ar group in Figure 6.5.* These events are the combined results of ^{32}Ar ions that landed near the edge of D_3 after scattering in D_2 and those that reacted before coming to rest. This was later confirmed by GEANT calculations [75].

6.2.2 Number of implanted ions

Good ions were tagged as ions that appeared in Region 3.1 of Figure 6.3 and Region 5.1 of Figure 6.4 and did not deposit any energy in D_4 . *Ambiguous* ions on the other hand had to appear in either:

1. Region 3.2 of the E_1 vs. TOF_1 spectrum *and* either Region 5.1 *or* 5.2 of the

E_3 vs. E_2 spectrum, or

2. Region 3.1 of the E_1 vs. TOF₁ spectrum *and* Region 5.2 of the E_3 vs. E_2 spectrum, or
3. Region 6.1 of the E_1 vs. TOF₁ spectrum (*but not* Region 3.1 *or* 3.2) *and* Region 4.2 of the E_3 vs. E_2 spectrum, or
4. Region 3.1 of the E_1 vs. TOF₁ spectrum and Region 5.1 of the E_3 vs. E_2 spectrum (like a *good* ion) but also depositing energy in D₄.

A total of $N_{\text{Ar}} = 2.470 \times 10^6$ *good* ^{32}Ar ions (not preceded by an *ambiguous* ion in 500 ms) were implanted, along with $N_{\text{a}} = 0.130 \times 10^6$ *ambiguous* ions and $N_{\text{c}} \approx 1.000 \times 10^6$ *contaminant* ions.

If any of the *ambiguous* ions were ^{32}Ar ($t_{1/2} = 100.5(2)$ ms [65]), at most 3.18(2)% of their decays would occur after the end of 500 ms veto period and would be indistinguishable from the decay products of *good* ^{32}Ar ions. This effect was corrected for by averaging two extreme cases: that all the *ambiguous* ions were ^{32}Ar ions and that no *ambiguous* ions were ^{32}Ar ions. This average was added to N_{Ar} with a 100% uncertainty to obtain:

$$N_{\text{Ar}}^{\text{uncorr}} = (2.472 \pm 0.002) \times 10^6. \quad (6.1)$$

Monte Carlo simulations using GEANT to check for fragmentation reactions within D₃ indicate a loss of $(0.2 \pm 0.2)\%$ ^{32}Ar ions due to nuclear fragmentation [75]. This correction is incorporated to obtain a corrected number of implanted ^{32}Ar ions

$$N_{\text{Ar}}^{\text{corr}} = (2.467 \pm 0.005) \times 10^6. \quad (6.2)$$

Experimental investigation of the beam profile distribution was done using a ^{28}Al beam. The heavy ion count rates in D_1 , D_2 and D_3 were compared to the rates when a collimator was placed upstream of D_2 that blocked $\approx 40\%$ of its active area. This comparison indicated that the ^{32}Ar beam was highly non-uniform. This data was then used in conjunction with GEANT simulations and LISE calculations to obtain the radial beam profile and the implantation depth for ^{32}Ar ions in D_3 .

6.3 Beta-delayed proton branches

6.3.1 Delayed proton spectra

Figure 6.7 shows the energy spectrum of *decay* events in D_3 . The peaks correspond to beta-delayed proton groups from ^{32}Ar , with the prominent peak at $E_p \approx 3500$ keV being from the superallowed decay (see Figure 6.1 for a simplified decay scheme). The proton lines had pronounced high-energy tails from the summing with the energy deposited by the escaping positrons. The structure below $E_3 \approx 2$ MeV is dominated by β -decays not followed by protons (such as ^{32}Ar decays to particle-bound states of ^{32}Cl , or implanted ^{31}Cl ions that decay mainly to the ^{31}S ground state).

The areas under the delayed proton peaks were determined with the aid of a previously obtained high-resolution (≈ 5 keV FWHM) proton spectrum obtained at ISOLDE [14, 65] as shown in Figure 6.8.

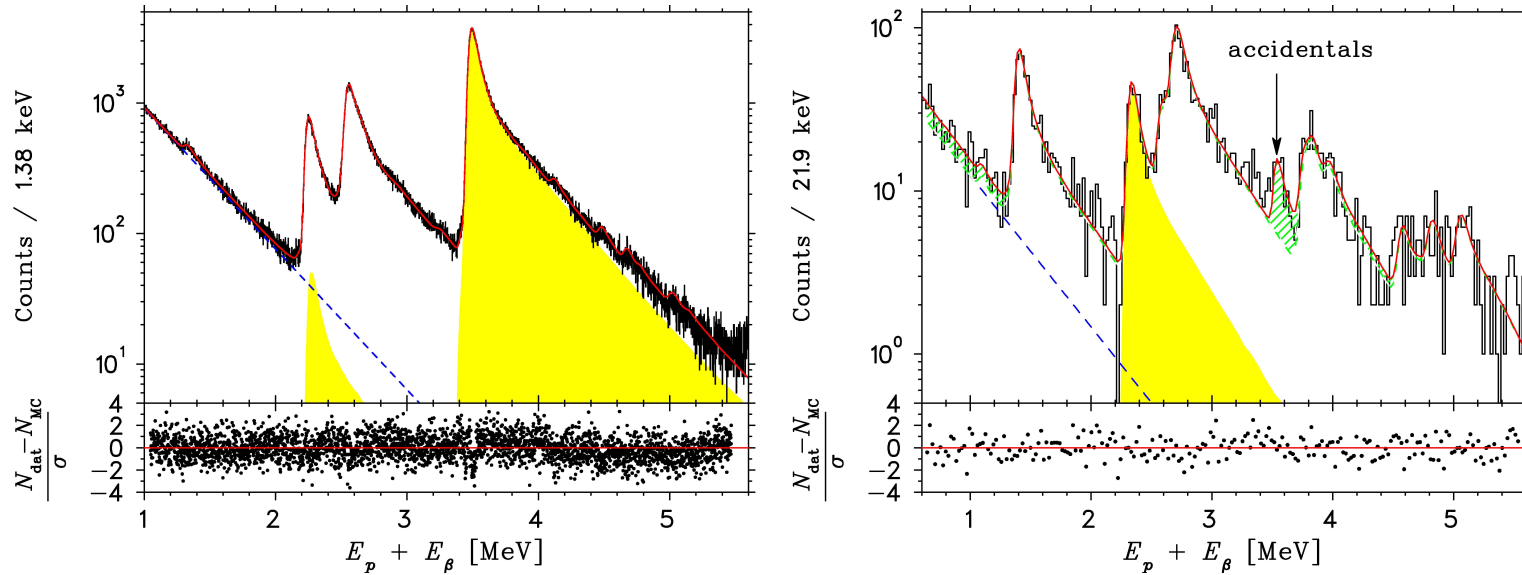


Figure 6.7. Left panel: singles delayed proton spectrum in D_3 (histogram) along with the corresponding R-matrix fit (solid line). The long high-energy tails are due to β summing. The filled curve corresponds to proton emission following the superallowed transition and the dashed is the β background. Right panel: same as the left, but gated by $E_\gamma = 1249$ keV. In this case, proton emission following the superallowed transition is peaked at ≈ 2.3 MeV.

This spectrum was fitted using a R-matrix formalism for overlapping, interfering daughter states [76] that parameterized the intrinsic delayed proton spectrum in terms of the transition matrix elements M_β , energies and proton widths Γ_p of 19 daughter states (except for the Fermi transitions, all the allowed decays are to 1^+ states that interfere with one another). This intrinsic shape was folded with a detector response function consisting of a Gaussian folded with two exponentials as described in Ref. [14] to fit the data in Figure 6.8. This yielded the relative intensities, energies and intrinsic widths of the proton groups with energies up to 4 MeV. Next, R-matrix levels were added to reproduce the energies and intensities of 9 weakly-fed states with $E_p > 4$ MeV. The widths of these levels were assumed to be negligible and their total intensity relative to the total intensity in the 2 – 4 MeV window is $\approx 1.9\%$. The data from the NCSL spectrum shown in Figure 6.7 were fit using the relative areas and widths from the ISOLDE spectrum allowing only the electronic noise parameters and the relative normalizations of backgrounds to vary freely. The overall normalization was fixed to equal the number of counts in the data. The backgrounds consist of a ^{29}S contamination and the minimally-ionizing β s (described by a simple exponential). The intrinsic proton shape from the ISOLDE data was input into a GEANT simulation which tracked and summed the deposited energies of both the proton and β . The model used in the fit was this simulated spectrum convoluted with Gaussian noise. The same approach was used to simulate the ^{29}S background. The resulting fit to the singles delayed proton spectrum in D_3 (shown in Figure 6.7) allowed to extract the total number of delayed protons and, based on the R-matrix intensity ratios, the number of decays for each of the groups.

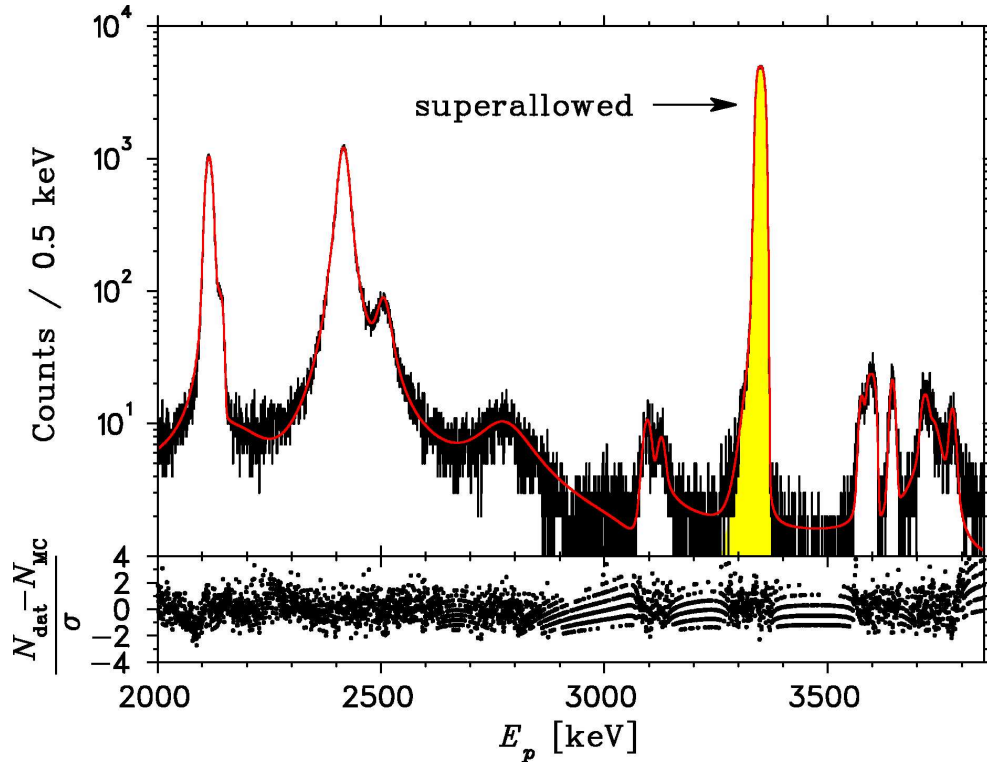


Figure 6.8. ISOLDE data and its corresponding R-matrix fit. This spectrum was taken by implanting 60 keV ^{32}Ar ions into a $20 \mu\text{g}/\text{cm}^2$ carbon foil and observing the beta-delayed proton groups with cooled PIN diodes. The detection setup was immersed in a 3.5 Tesla magnetic field that prevented the β s from reaching the detectors and summing with protons.

6.3.2 Delayed proton transitions feeding the ^{31}S first excited state

We used the γ -ray spectra to identify several delayed proton transitions to the $J^\pi = 3/2^+$, $E_x = 1249$ keV first excited state of ^{31}S . The right panel of Figure 6.7 shows the E_3 spectrum of events in coincidence with the 1249 keV γ -ray in any of the 5 Ge detectors. Once the groups were identified, we used the ISOLDE spectrum to obtain their relative intensities. This allowed us to infer the relative intensities of these groups without depending on the γ -ray efficiency. Table 6.1 lists the intensities obtained from these proton groups relative to the intensity of the superallowed proton group populating the ^{31}S ground state.

6.3.3 Delayed proton branches following the superallowed decay

On fitting the NSCL singles spectrum, we obtain $N_{p0} = (5.093 \pm 0.013) \times 10^5$ protons from the ^{32}Cl isobaric analog state (IAS) to the ^{31}S ground state (filled histogram). The uncertainty includes statistical fluctuations, the uncertainty in the line shape and the signal-to-background ratio.

The $E_p \approx 2.3$ MeV peak (filled histogram), clearly visible in the right panel of Figure 6.7 corresponds to proton emission from the IAS to the 1249-keV level in ^{31}S . This peak appears in the ISOLDE spectrum as a partially resolved shoulder on the right of the structure at $E_p \approx 2.1$ MeV. We obtained $N_{p1}/N_{p0} = (1.25 \pm 0.10)\%$ from the NSCL data which is in agreement with $N_{p1}/N_{p0} = (1.29 \pm 0.04)\%$ from the ISOLDE data. We adopt $N_{p1}/N_{p0} = (1.28 \pm 0.04)\%$ obtained as a weighted average but retain the smaller of the two uncertainties.

Furthermore, the ISOLDE spectrum was used to extract information for decays to the states at $E_x = 2235.6$ keV ($J^\pi = 5/2^+$) and $E_x = 3079$ keV ($J^\pi = 1/2^+$), such that $N_{p2}/N_{p0} = (0.12 \pm 0.04)\%$ and $N_{p3}/N_{p0} \leq 0.14\%$.

TABLE 6.1
 PROTON GROUPS IN COINCIDENCE WITH A 1249
 KEV GAMMA RAY

This work			Previous work [77]	
E_p (keV)	E_x (keV)	I_p (%) ^a	E_p (keV)	I_p (%) ^a
912(5)	3772(5)	0.07(4)	--	--
1218(5)	4087(5)	1.81(22)	1214(10)	1.8(2)
2145(5)	5046(5)	1.06(20)	--	--
2394(5)	5302(5)	0.62(11)	--	--
2515(5)	5427(5)	2.63(11)	--	--
3581(5)	6528(5)	0.37(4)	3592(10)	0.83(9)
3649(5)	6599(5)	0.30(3)	3643(10)	0.39(9)
3785(5)	6738(5)	0.12(5)	--	--
4386(5)	7361(5)	0.17(2)	--	--
4529(5)	7507(5)	0.03(1)	4521(10)	0.52(8)
4630(5)	7611(5)	0.14(5)	4621(10)	0.04(4)
4869(5)	7857(5)	0.18(3)	4858(10)	0.12(4)

^a Relative to the superallowed proton group leaving ³¹S in its ground state.

The total proton branch for the superallowed transition was then determined to be

$$b_{\text{SA}}^{\beta\text{p}} = \frac{N_{\text{p0}}}{N_{\text{Ar}}} \left(1 + \sum_{i=1,3} \frac{N_{\text{p},i}}{N_{\text{p0}}} \right) = (20.93 \pm 0.08)\% \quad (6.3)$$

where the error includes both statistical and systematic uncertainties.

The total number of protons up to 6.5 MeV was extracted from the normalized number of counts from the fit after the fit converged. The result, $N_p^{\text{tot}} = (8.818 \pm 0.005) \times 10^5$, implies a total proton branch of:

$$b_{\text{tot}}^{\beta\text{p}} = \frac{N_p^{\text{tot}}}{N_{\text{Ar}}} = (35.74 \pm 0.08)\%. \quad (6.4)$$

6.4 Beta-delayed γ branches

Figure 6.9 shows the summed γ -ray spectrum from the 5 Ge detectors in coincidence with a *decay* event in D₂, D₃ or D₄. To optimize statistics the *ambiguous* ion electronic dead time was not imposed. Nevertheless, all of the visible peaks correspond to ³²Ar decays which shows the absence of any significant contamination. The trigger for the experiment was given by events that left energy above threshold in any of the detectors D₂, D₃ or D₄. The probability of detecting a beta in any of these Si detectors was determined with a PENELOPE Monte Carlo simulation. Using the measured energy thresholds this was found to be $\epsilon_\beta = 0.99(1)$, independent of β end-point energy to within uncertainty. Thus, the γ -ray detection efficiency was largely independent of the β detection efficiency.

6.4.1 Gamma ray efficiencies

As explained previously, in order to determine the absolute γ branches from ³²Ar β -decay, an accurate γ detection efficiency calibration can be obtained using

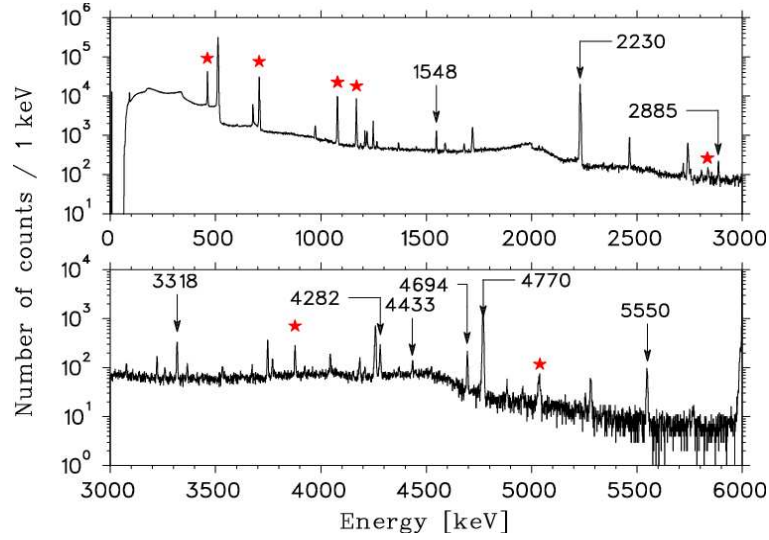


Figure 6.9. Spectrum of γ -rays in coincidence with a β signal in D₂, D₃, or D₄. Lines from ^{32}Ar decay are marked with a “★”. The remaining labelled lines are from ^{32}Cl decay.

the known delayed γ intensities from the decay of ^{32}Cl .

For a given γ -ray from the decay of ^{32}Cl , the γ -ray detection efficiency for detector G_i , $\epsilon_\gamma(G_i)$, can be obtained from

$$N_{\text{Ar}}(1 - b_{\text{tot}}^{\beta\text{p}}) b^{\beta\gamma}(^{32}\text{Cl}) = \left[\frac{N_\gamma(G_i)}{\eta_{\text{sum}}(G_i)\epsilon_\gamma(G_i)\epsilon_\beta} \right], \quad (6.5)$$

where $N_\gamma(G_i)$ and $b^{\beta\gamma}(^{32}\text{Cl})$ represent the photo-peak area of the gamma ray of interest and the known gamma yield [66] from ^{32}Cl decay respectively and the factor ϵ_β is the efficiency for detecting a β in the Si detectors. The factor $\eta_{\text{sum}}(G_i)$ is the summing correction factor which depends on the β and the γ branches and the solid angle subtended by the detector. This summing correction factor is defined such that the observed number of counts for a given peak, $N_\gamma(G_i)$, is

actually

$$N_\gamma(G_i) = \eta_{\text{sum}} N_\gamma^{\text{true}}(G_i), \quad (6.6)$$

where $N_\gamma^{\text{true}}(G_i)$ is the “true” photo-peak area if there existed no coincidence summing of the γ -rays.

Eq. (6.5) can be rewritten as

$$N_{\text{Ar}} \epsilon_\gamma(G_i) \epsilon_\beta = \left[\frac{N_\gamma^{\text{true}}(G_i)}{(1 - b_{\text{tot}}^{\beta\gamma}) b^{\beta\gamma}({}^{32}\text{Cl})} \right]. \quad (6.7)$$

It will be shown later (in Eq. 6.8) that the factor on the left side of Eq. 6.7 (rather than $\epsilon_\gamma(G_i)$) can be used to compute all of the γ branches following ${}^{32}\text{Ar}$ superallowed decay. This minimizes systematic uncertainties due to the geometrical size and distribution of the source, and uncertainties from ${}^{32}\text{Ar}$ ions that might have escaped detection (i.e. ions that land outside the active area in D_3 but whose γ s and β s could have been detected).

The γ -ray detection efficiency and the summing corrections were determined using PENELOPE Monte Carlo simulations. Figure 6.10 shows the stack of Si detectors used for the simulation. Figures 6.11 and 6.12 show the geometry of one clover and the 120% Ge detector, and Figure 6.13 shows the complete geometry file of the detector array that was used for the simulations.

The Monte Carlo simulations used the factory specified geometry of the crystals, the distances from D_3 and the implantation profile of the ${}^{32}\text{Ar}$ beam in D_3 to obtain the detection efficiencies for the detectors at the relevant energies. Then, the areas of the calibration peaks were determined independently using lineshape fits explained previously. The summing corrections were obtained using two other simulations. In one, for a given number of β -decays of ${}^{32}\text{Cl}$, the beta and gamma



Figure 6.10. Stack of Si detectors.

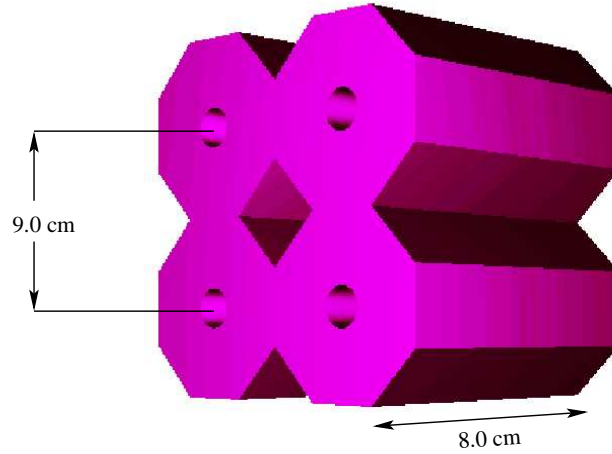


Figure 6.11. Geometry file for one of the clovers.

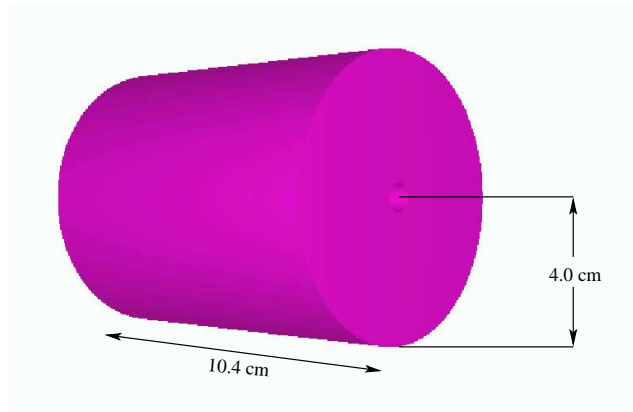


Figure 6.12. Geometry of the 120% detector.

branches from the TAMU measurement were used to feed states in ^{32}S and generate the γ -rays from the subsequent transitions. This simulation also registered the total number of photons originating from D_3 for each γ -ray energy. The energies deposited in each of the 5 detectors were then histogrammed and the photo-peak areas from the simulation determined. In the other simulation, the peak areas were obtained for the 5 detectors for a given number of photons originating from D_3 , independent of the branches. The summing correction for each γ -ray in the five detectors were obtained using ratios of the results from the two simulations. Tables 6.2 and 6.3 show the simulation results for the ^{32}Cl γ -rays in each detector. The ratios of the photo-peak areas from the Monte Carlo simulations were found to be in excellent agreement with the data.

For each detector, the data were fit using N_{Ar} in Eq. (6.7) as a normalization factor that was the only free parameter, allowed to vary to obtain agreement with the measured peak areas. Figure 6.14 shows the resulting efficiencies along with the PENELOPE simulated efficiency curves for each detector.

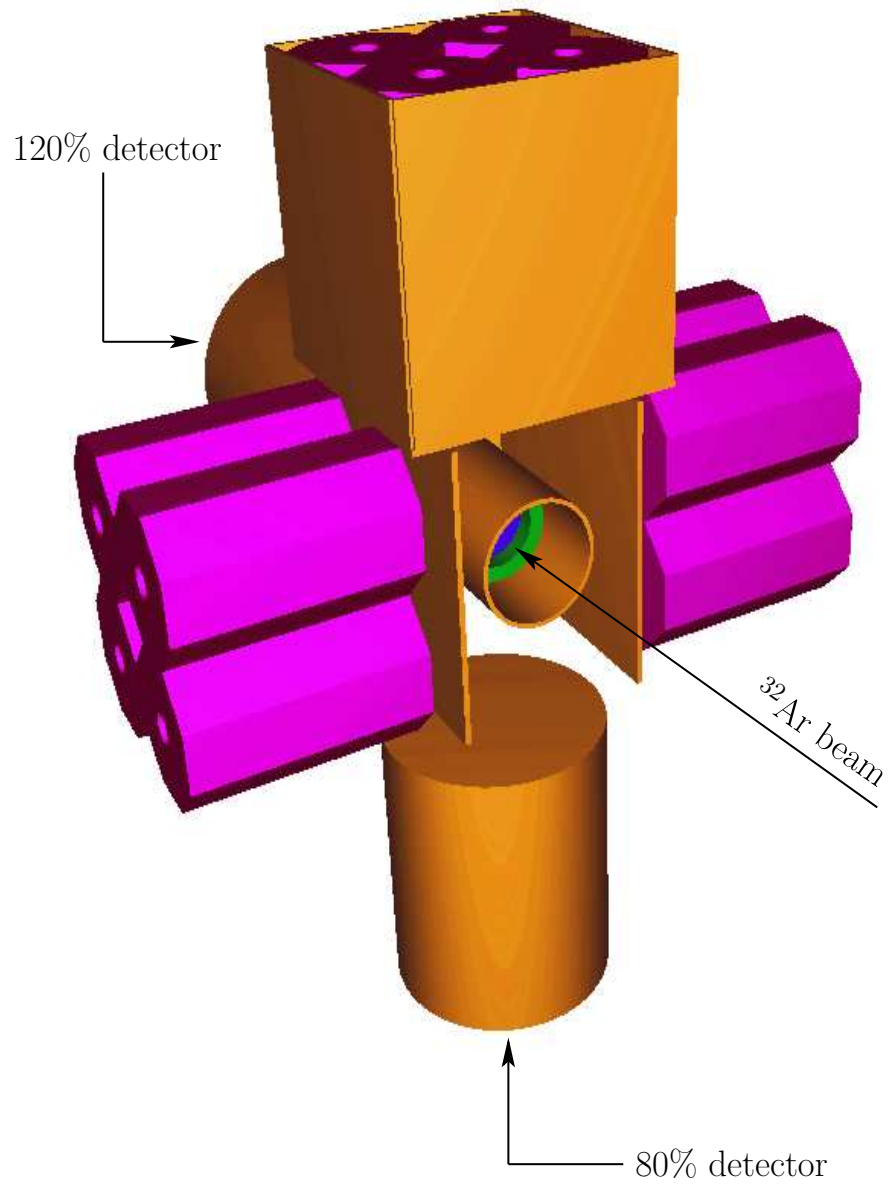


Figure 6.13. Geometry file of the detector array used for simulations. The Si detectors are surrounded by the beamline. The aluminium endcaps for two side clovers are not shown in the figure, but are used in the simulations.

TABLE 6.2

SUMMING CORRECTIONS AND SIMULATED EFFICIENCIES

E_γ (keV)	120% detector		80% detector		Clover 1	
	$\epsilon_\gamma(\times 10^3)$	η_{sum}	$\epsilon_\gamma(\times 10^3)$	η_{sum}	$\epsilon_\gamma(\times 10^3)$	η_{sum}
5549	5.53(7)	1.032(20)	2.49(5)	1.033(30)	6.52(8)	1.027(19)
4771	6.44(8)	0.933(12)	2.89(5)	0.977(19)	7.47(9)	0.912(11)
4695	6.48(8)	1.020(16)	2.91(5)	1.007(24)	7.63(9)	1.029(15)
4435	6.92(8)	0.942(20)	8.25(9)	0.925(18)
4282	7.07(8)	1.005(16)	3.16(6)	1.008(24)	8.35(9)	1.001(15)
3319	8.80(9)	0.931(13)	4.06(6)	0.953(20)	10.52(10)	0.909(12)
2887	9.59(10)	0.910(16)	4.44(7)	0.933(24)	11.47(11)	0.837(14)
2465	11.22(11)	0.928(11)	4.96(7)	0.979(17)	13.13(12)	0.912(10)
2231	11.96(11)	0.975(9)	5.43(7)	0.976(13)	14.35(12)	0.956(8)
1548	15.26(12)	0.911(10)	6.78(8)	0.950(15)	17.98(13)	0.870(9)

TABLE 6.3

SUMMING CORRECTIONS AND SIMULATED EFFICIENCIES

E_γ (keV)	Clover 2		Clover 3	
	$\epsilon_\gamma(\times 10^3)$	η_{sum}	$\epsilon_\gamma(\times 10^3)$	η_{sum}
5549	4.49(7)	1.028(23)	6.48(8)	1.019(19)
4771	5.23(7)	0.940(14)	7.58(9)	0.911(11)
4695	5.37(7)	1.010(18)	7.67(9)	1.056(16)
4435	5.70(8)	0.914(22)	8.09(9)	0.955(19)
4282	5.81(8)	1.012(18)	8.34(9)	1.008(15)
3319	7.29(9)	0.935(15)	10.45(10)	0.902(12)
2887	8.10(9)	0.855(16)	11.87(11)	0.799(13)
2465	9.07(10)	0.948(12)	13.40(12)	0.891(9)
2231	9.85(10)	0.978(10)	14.05(12)	0.977(8)
1548	12.56(11)	0.892(11)	18.02(13)	0.873(9)

6.4.2 Gamma decays of the ^{32}Cl isobaric analog state

The decays of the isobaric analog states in ^{32}P and ^{32}S lead us to expect γ -decays to three 1^+ levels (see Figure 6.1) in ^{32}Cl .

The absolute γ branches for these decays can be computed as,

$$b^{\beta\gamma} = \frac{\sum_{i=1}^5 N_{\gamma}^{\text{true}}(G_i)}{N_{\text{Ar}} \sum_{i=1}^5 \epsilon_{\gamma}(G_i) \epsilon_{\beta}}, \quad (6.8)$$

where the sum runs over all 5 Ge detectors; $N_{\gamma}(G_i)$ is the summing-corrected area of the particular γ -ray peak in detector G_i , and $\epsilon_{\gamma}(G_i)$ and ϵ_{β} are the γ photo-peak and β efficiencies respectively. We assume that ϵ_{β} is independent of the energy of the beta transition (a GEANT simulation indicated that the variations are negligible compared to other uncertainties in our experiment). The denominator on the right hand side of Eq. (6.8) comes from the calibration using lines from ^{32}Cl decay, which makes the calculation of the branches rather independent of the distribution of parent ions, as explained previously.

The β - γ coincidence spectrum in Figure 6.9 shows a peak at $E_{\gamma} = 3877.5(3)$ keV that is a candidate for the analog of the ^{32}P 5072 keV \rightarrow 1149 keV transition [32]. Figure 6.15 shows the spectrum of γ -rays in coincidence with a 3877-keV γ -ray in the $\beta - \gamma$ coincidence spectrum. The spectrum clearly shows the γ -rays expected from de-excitation of the 1168.5(2) keV state, confirming that the decays originate from the state at $E_x = 5046.3(4)$ keV after correcting for nuclear recoil. This verified the 3877 keV γ -ray to be the isobaric analog of the 5072 keV \rightarrow 1149 keV transition in ^{32}P .

The ^{32}P $T = 2$ state also decays directly to the ground state, which implies

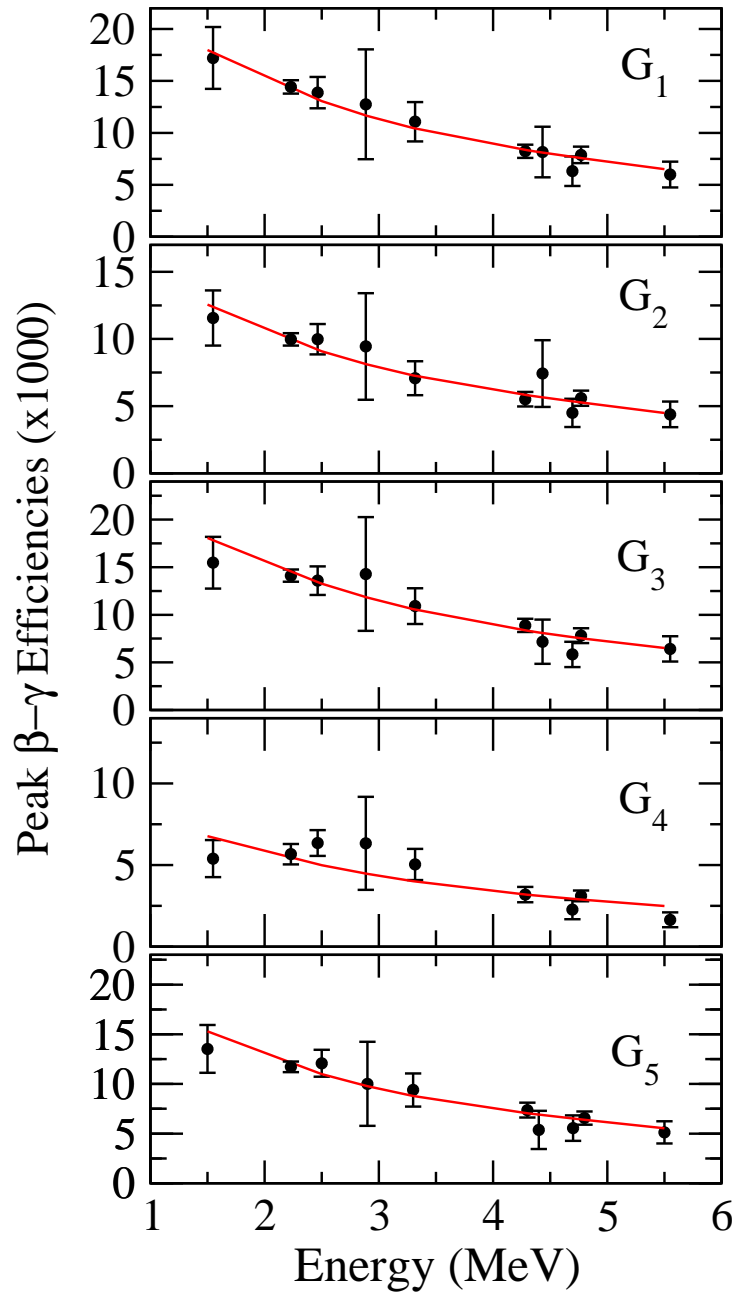


Figure 6.14. The absolute $\epsilon_{\gamma}\epsilon_{\beta}$ from ^{32}Cl decays and the PENELOPE efficiency curves for each detector.

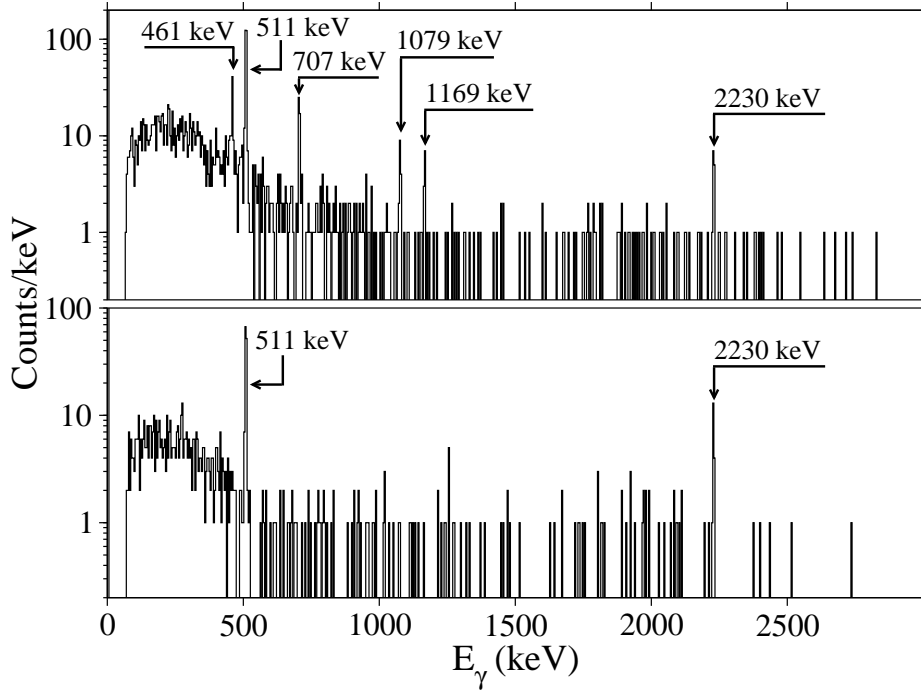


Figure 6.15. Spectrum of γ s in coincidence with 3878-keV γ -rays and a β signal in D₂, D₃ or D₄. All of the peaks except for the ones at 2230 keV and 511 keV correspond to the expected γ cascades following the 3878-keV γ ray. Bottom panel: same as above, but with the coincidence gate shifted down by 8 keV. This shows that the 2230-keV γ comes mainly from coincidences with the Compton continuum of the 4770-keV γ ray in ^{32}S .

that there ought to be a 5046-keV γ transition in ^{32}Cl . Unfortunately, the first escape peak of the 5549 keV γ -ray from ^{32}Cl appears as a strong peak in the region of interest in the spectrum. We however do not observe any significant contribution from the 5046 keV γ -ray. Figure 6.16 shows data from the summed spectrum of all the 5 detectors and the corresponding fit. The 5046 keV peak was fitted with a fixed centroid and width, allowing only the background and area parameters to vary to obtain the photo-peak areas from each detector.

The analog of the 5072 keV \rightarrow 2230 keV γ transition in ^{32}P [32] is observed

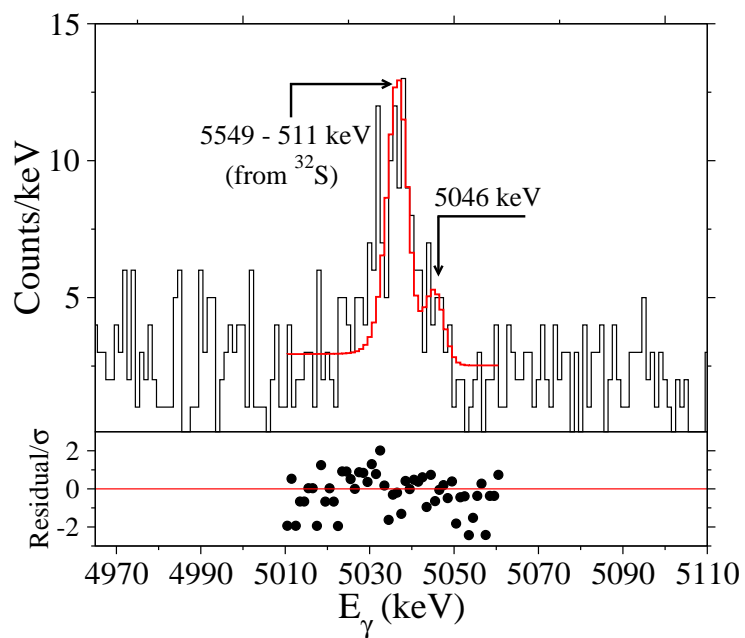


Figure 6.16. The region of interest where the γ ray corresponding to the decay from the $T = 2$ state to the ground state should appear at $E_\gamma = 5046$ keV. The main 5038-keV peak is the first escape from the 5550-keV γ ray from ^{32}Cl .

at $E_\gamma = 2836(1)$ keV. This is observed close to another peak at 2839 keV. We identified the 2836 keV peak as the one that arises from the analog transition by observing the proton spectrum in coincidence with both these peaks independently. As shown in Figure 6.18, protons at corresponding to energy 610(5) keV are observed in coincidence with the 2836 keV γ -ray. No protons are observed in coincidence with the 2839 keV γ -ray. The energy of the proton implies that was emitted from a state at 2212(5) keV which when added to 2836(1) keV yields $E_x = 5048(5)$ keV, consistent with the energy of the $T = 2$ state in ^{32}Cl .

The energy calibration for the above analysis was done by obtaining the peak centroids for a few high statistics peaks corresponding to γ -rays following the decay of ^{32}Cl . These centroids were fit to a linear function of the form shown previously in Eq. (3.3), using the known energies of states in ^{32}S . Figure 6.17 shows the residuals from the fits for all five detectors.

The absolute intensities of the three γ -decays of the $T = 2$ state are listed in Table 6.4. The total β -delayed γ branch for the superallowed transition is found to be

$$b_{\text{SA}}^{\beta\gamma} = (2.03 \pm 0.10)\%. \quad (6.9)$$

The superallowed branch is obtained from the proton and gamma branches to be

$$b_{\text{SA}}^\beta = (b_{\text{SA}}^{\beta\gamma} + b_{\text{SA}}^{\beta\text{p}}) = (22.96 \pm 0.13)\%. \quad (6.10)$$

6.5 ft value of the superallowed decay

Using a recent determination of the mass of ^{32}Ar [18] in addition to a recent determination of the β -delayed proton energy [65] and the masses of ^{31}S and the

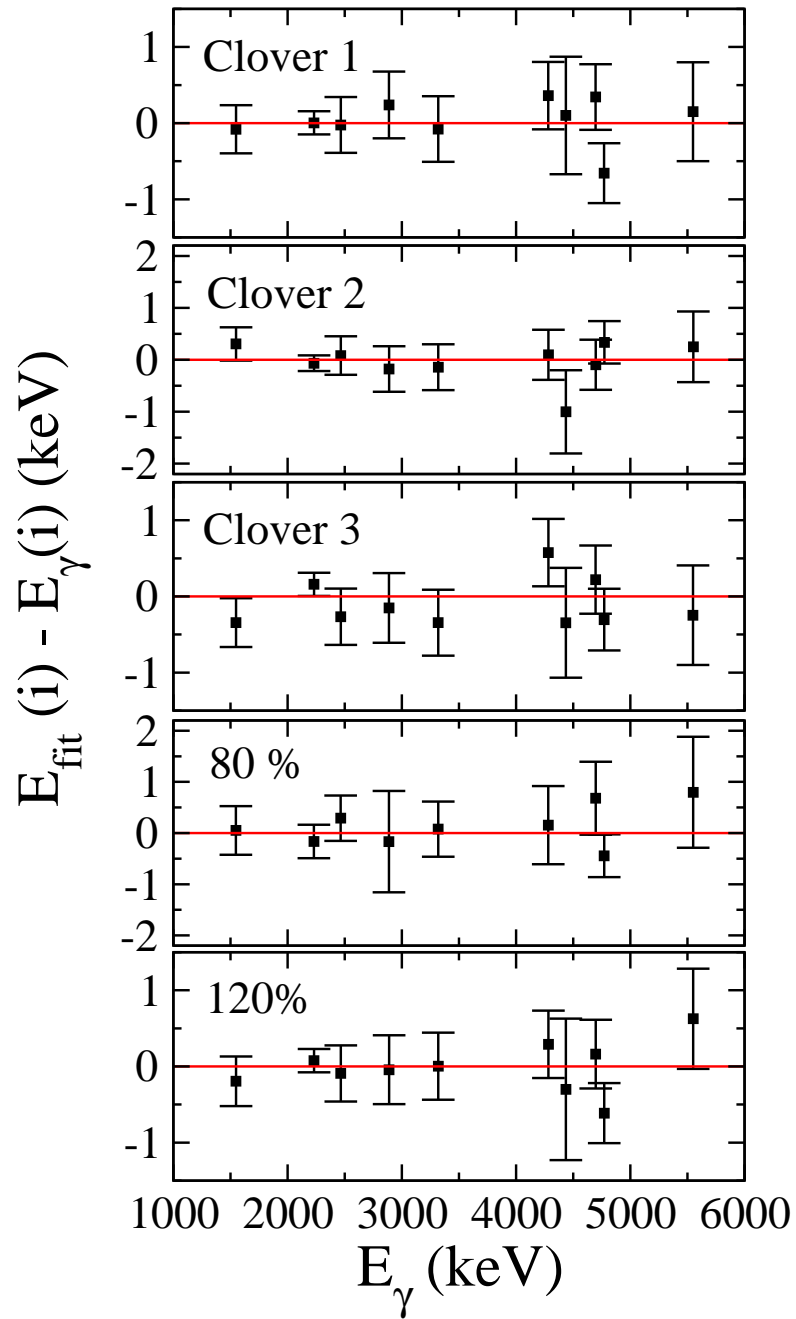


Figure 6.17. Residuals of linear fits. The energy calibration is largely linear for all detectors from 1 MeV to 6 MeV.

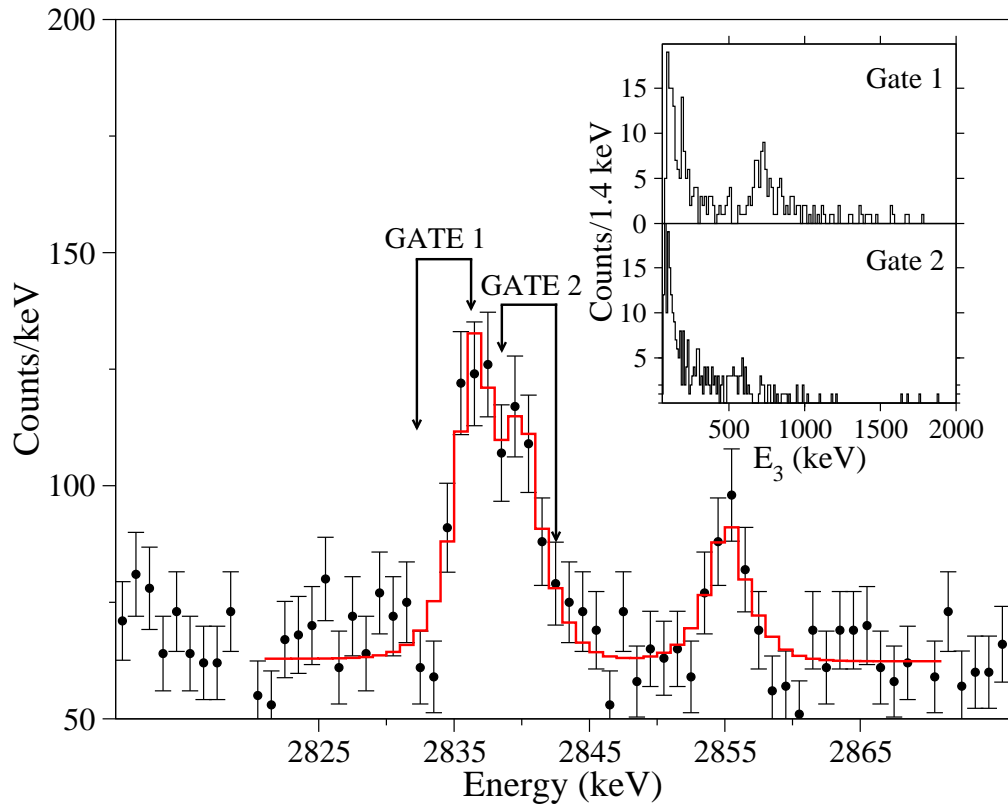


Figure 6.18. The 2836 and the 2839 keV γ -ray doublet. The insets show the proton spectrum gated with GATE 1 (which has a peak corresponding to 610-keV protons) and GATE 2 respectively. This shows that the 2836-keV component is followed by proton emission whereas the 2839-keV γ is not.

TABLE 6.4

ABSOLUTE $\beta\gamma$ BRANCHES FROM THE LOWEST
 $T = 2$ STATE IN ^{32}Cl

E_γ (keV)	$b_{\text{SA}}^{\beta\gamma}$
3877	1.69(9)
2836	0.25(4)
5046	0.09(2)

proton the Q_{EC} value for the transition is found to be

$$Q_{EC} = 6091.3 \pm 2.5 \text{ keV}, \quad (6.11)$$

which yields a statistical phase space factor of [78]

$$f = 3507.0 \pm 8.2. \quad (6.12)$$

The half-life of ^{32}Ar is obtained from the ISOLDE measurement [65]

$$t_{1/2} = 100.5 \pm 0.2 \text{ ms}, \quad (6.13)$$

from which the ft value of the superallowed decay to the IAS is determined to be

$$ft(^{32}\text{Ar}) = \left(\frac{ft_{1/2}}{b_{\text{SA}}^\beta} \right) = 1535 \pm 10 \text{ s}. \quad (6.14)$$

The isospin breaking corrections and the nucleus dependent radiative corrections

for the case of ^{32}Ar have been calculated [64, 78], $\delta_C = (2.0 \pm 0.4)\%$ and $\delta_R = (1.404 \pm 0.038)\%$. These yield the corrected ft value for the superallowed decay of ^{32}Ar to be

$$\mathcal{F}t = 1525 \pm 12 \text{ s.} \quad (6.15)$$

The isospin breaking correction is the determined experimentally from

$$\frac{\mathcal{F}t(T = 1)}{2ft(^{32}\text{Ar})} = (1 - \delta_C^{\text{exp}})(1 + \delta_R) , \quad (6.16)$$

where the factor of 2 corresponds to the ratio of squared matrix elements for $T = 2$ and $T = 1$ decays. The above equation yields

$$\delta_C^{\text{exp}} = (1.3 \pm 0.6)\% . \quad (6.17)$$

This result is in agreement with the theoretically calculated corrections from Ormand and Brown [64].

6.5.1 Widths and branches for γ -decays of the $T = 2$ state

Table. 6.5 compares the γ -ray branches of analogous decays of the lowest $T = 2$ states in the $A = 32$ multiplet. There is reasonable agreement with isospin conservation, which predicts that the branches should be independent of T_3 . On combining the value for the γ branch of the $T = 2$ state, and the superallowed beta branch b_{SA}^β with the total width $\Gamma = 20 \pm 5$ eV obtained from the ISOLDE data [65] the radiative width of the $T = 2$ state is found to be, $\Gamma_\gamma = 1.8 \pm 0.5$ eV. The shell-model prediction using the USD interaction [80] yields, $\Gamma_\gamma \approx 1.1 \pm 0.1$ eV.

TABLE 6.5

RELATIVE γ BRANCHES FROM THE LOWEST
 $T = 2$ STATES IN THE $A = 32$ MULTIPLY

E_γ (MeV)	Relative γ branch		
	^{32}Cl	^{32}S [79]	^{32}P [33]
3.9	84(2)	84.3(9)	85.7(8)
2.8	12(2)	9.4(7)	9.4(5)
5.1	4(1)	6.3(7)	4.7(6)

CHAPTER 7

CONCLUSIONS AND FUTURE DIRECTIONS

In conclusion, we have studied the effects of isospin symmetry breaking in $A = 32$ nuclei via two high-precision measurements:

We remeasured the excitation energy of the lowest $T = 2$ state in ^{32}S using the $^{31}\text{P}(p, \gamma)$ reaction. This measurement made the $A = 32$ quintet the most precisely measured multiplet to date. We observe a significant violation of the IMME for this multiplet which could indicate either an erroneous mass measurement of a member of the quintet or isospin mixing with other 0^+ levels in ^{32}S . The most suspect member of the quintet is ^{32}Si . Plans are underway to remeasure the ^{32}Si mass using an ion-trap (LEBIT) at NSCL (Michigan State University). In addition, investigations by B. A. Brown *et al.* [64] indicate that the d coefficient for the IMME is required due to isospin mixing in ^{32}Cl . Both of these issues need to be studied in detail before arriving at any conclusive evidence regarding the status of the IMME.

The ft value for the $0^+ \rightarrow 0^+$ superallowed decay of ^{32}Ar is the first such measurement for a $T = 2$ nucleus. The measured ft value provides a check of the calculated isospin-breaking corrections, which are important for tests of the CVC hypothesis and CKM unitarity. Our measured value agrees well with the theoretically calculated value. Analysis is ongoing to check and correct for systematic effects that could affect our measurement. An independent calculation

using the Woods-Saxon potential of Towner and Hardy will provide an additional check on the charge dependent correction. In addition, the $e^+ - \nu$ correlation data from ISOLDE can be used to determine the attenuation of the Fermi strength due to configuration mixing with non-analog states. This will help extract the δ_{CM} correction for ^{32}Ar decay experimentally and can be compared to shell model predictions.

Such measurements can be extended to other $A = 4n$, $T = 2$ nuclei whose decays can be used as a systematic check of the isospin breaking corrections. These $T = 2$ cases can be used to test the CVC hypothesis and place CKM unitarity tests on a secure footing.

APPENDIX A

DESCRIPTION OF THE LINESHAPE FUNCTION TO FIT GAMMA PEAKS

In the absence of statistical and electronic noise a γ peak will be a δ function at the energy of interest. To account for charge-collection effects in the HPGe detector, we add a low-energy exponential tail to this δ function such that the peak shape is of the form: (for a peak centered at $x = 0$)

$$L(x) = T(x) + \delta(x) , \quad (\text{A.1})$$

where $T(x)$ is an exponential tail.

Since the convolution of two functions $f(x)$ and $g(x)$ is defined as:

$$\int_{-\infty}^{\infty} f(x)g(x' - x)dx$$

For the functional form of the tail in the peak we want the convolution of an exponential and a Gaussian that results in the following integral,

$$\int_{-\infty}^{\infty} e^{x/l} e^{-\frac{(x'-x)^2}{2\sigma^2}} dx$$

For an exponentially decaying distribution below the peak centroid, we define $\Theta(x)$, such that $\Theta(x) = 1$ if $x \leq 0$ and $\Theta(x) = 0$ otherwise.

This results in a convolution integral

$$\begin{aligned} T(x') &= \int_{-\infty}^{\infty} \frac{1}{\sqrt{2\pi}\sigma} e^{x/l} \exp\left(\frac{-(x' - x)^2}{2\sigma^2}\right) \Theta(x) dx \\ &= \int_{-\infty}^0 \frac{1}{\sqrt{2\pi}\sigma} e^{x/l} \exp\left(\frac{-(x'^2 + x^2 - 2xx')}{2\sigma^2}\right) dx . \end{aligned}$$

Where x can take only negative values here on account of the step function.

$$= \frac{1}{\sqrt{2\pi}\sigma} e^{-x'^2/2\sigma^2} \int_{-\infty}^0 e^{-\left[\frac{x^2}{2\sigma^2} - x\left(\frac{x'}{\sigma^2} + \frac{1}{l}\right)\right]} dx$$

On substituting $\frac{x'}{\sigma^2} + \frac{1}{l} = \frac{b}{\sigma^2}$ and then adding and subtracting $\frac{b^2}{2\sigma^2}$ in the parentheses we get the expression

$$= \frac{1}{\sqrt{2\pi}\sigma} \exp\left(\frac{-(x'^2 - b^2)}{2\sigma^2}\right) \int_{-\infty}^0 \exp\left(\frac{-(x - b)^2}{2\sigma^2}\right) ,$$

which, on substituting for b^2 simplifies to

$$= \frac{1}{\sqrt{2\pi}\sigma} \exp\left(\frac{\sigma^2}{2l^2} + \frac{x'}{l}\right) \int_{-\infty}^0 \exp\left(\frac{-(x - b)^2}{2\sigma^2}\right)$$

The integral is now trivial, we make the substitution $t = \frac{x-b}{\sqrt{2}\sigma}$ and change the variables and limits to get

$$= \frac{1}{\sqrt{2\pi}\sigma} \exp\left(\frac{\sigma^2}{2l^2} + \frac{x'}{l}\right) \int_{-\infty}^{-b/\sqrt{2}\sigma} e^{-t^2} \sqrt{2}\sigma dt$$

Further using the definition that,

$$\operatorname{erfc} z = \frac{2}{\sqrt{\pi}} \int_z^\infty e^{-t^2} dt$$

and the following properties of the complementary error function,

$$\int_{-\infty}^z e^{-t^2} dt = \int_{-\infty}^\infty e^{-t^2} dt - \int_z^\infty e^{-t^2} dt$$

$$\operatorname{erfc}(-z) = 2 - \operatorname{erfc}(z)$$

we get

$$= \frac{1}{\sqrt{2\pi}\sigma} \exp\left(\frac{\sigma^2}{2l^2} + \frac{x'}{l}\right) \sqrt{2}\sigma \left[\sqrt{\pi} - \operatorname{erfc}\left(\frac{-b}{\sqrt{2}\sigma}\right) \frac{\sqrt{\pi}}{2} \right],$$

that results in a lineshape that has the generic form

$$T(x') = \frac{1}{2} \exp\left(\frac{\sigma^2}{2l^2} + \frac{x'}{l}\right) \operatorname{erfc}\left[\frac{1}{\sqrt{2}}\left(\frac{x'}{\sigma} + \frac{\sigma}{l}\right)\right]. \quad (\text{A.2})$$

If we want to generalize this for a peak centered at μ , normalized to unit area, the variable x' becomes $-(\mu - x)$ (the negative sign is added to maintain the sign of x') and the form of the tail becomes

$$T(x) = N \frac{1}{2} \exp\left(\frac{\sigma^2}{2l^2} + \frac{(x - \mu)}{l}\right) \operatorname{erfc}\left[\frac{1}{\sqrt{2}}\left(\frac{(x - \mu)}{\sigma} + \frac{\sigma}{l}\right)\right], \quad (\text{A.3})$$

where N is a normalization constant.

A.1 Normalization

We obtain the normalization factor for $T(x)$, so that the function has unit area, by integrating the function over all space. We define, $\Delta = x - \mu$, then

$$\int_{-\infty}^{\infty} T(x)dx = \frac{l}{2} \left[\operatorname{erf} \left(\frac{\Delta}{\sqrt{2}\sigma} \right) + \exp \left(\frac{\sigma^2}{2l^2} + \frac{\Delta}{l} \right) \operatorname{erfc} \left\{ \frac{1}{\sqrt{2}} \left(\frac{\sigma}{l} + \frac{\Delta}{\sigma} \right) \right\} \right]_{-\infty}^{\infty}$$

On evaluating this integral, we get the normalization constant to be $= 1/l$, such that the normalized $T(x)$ is

$$T(x) = \frac{1}{2l} \exp \left(\frac{\sigma^2}{2l^2} + \frac{(x - \mu)}{l} \right) \operatorname{erfc} \left[\frac{1}{\sqrt{2}} \left(\frac{(x - \mu)}{\sigma} + \frac{\sigma}{l} \right) \right] \quad (\text{A.4})$$

A.2 General functional form

We add two tails to the δ function, such that

$$L(x; \mu) = f_1 T_1(x) + f_2 T_2(x) + G(x) ,$$

where

$$G(x) = \frac{1}{\sqrt{2\pi}\sigma} \exp \left(\frac{-(x - \mu)^2}{2\sigma^2} \right) .$$

$G(x)$ is the direct result of folding the delta-function with a Gaussian spread. $T_1(x)$ is the low energy exponential tail attributed to charge collection effects, $T_2(x)$ is kept fixed for our data-analysis with a large decay-length. It represents the multiple Compton plateau below the peak centroid in the form of a smooth step-function.

Since $T_j(x)$ is normalized to unit-area, f_j provides the relative area under the particular tail with respect to the pure Gaussian. $L(x; \mu)$ is then normalized to

unit area in the following way;

$$L(x) = \left(1 - \sum_{j=1}^2 f_j\right) G(x) + \sum_{j=1}^2 f_j T_j(x) \quad (\text{A.5})$$

A.3 Binned Data

For binned data, if we are fitting the photopeak over a range of n bins, for a given bin-width ΔE keV, where $\Delta E = E_{high} - E_{low}$. We obtain the normalization constant for the tails by integrating Eq. A.3 from $x = 0$ to $x = \infty$, such that the normalized tail is of the form

$$T(x) = \frac{\frac{1}{l} \exp\left(\frac{\sigma^2}{2l^2} + \frac{(x-\mu)}{l}\right) \operatorname{erfc}\left[\frac{1}{\sqrt{2}}\left(\frac{(x-\mu)}{\sigma} + \frac{\sigma}{l}\right)\right]}{\left[1 + \operatorname{erf}\left(\frac{\mu}{\sqrt{2}\sigma}\right) - \exp\left(\frac{\sigma^2}{2l^2} - \frac{\mu}{l}\right) \operatorname{erfc}\left(\frac{(\frac{\sigma^2}{l}) - \mu}{\sqrt{2}\sigma}\right)\right]}. \quad (\text{A.6})$$

The fitting function (after adding additional background) is given by,

$$F(x) = \left(A \int_{E_{low}}^{E_{high}} L(x) dx + B + Cx + Dx^2\right) \quad (\text{A.7})$$

The χ^2 is defined as,

$$\chi^2 = \sum_{i=1}^{\text{nbins}} \left(\frac{F(x_i) - y(x_i)}{\Delta y(x_i)}\right)^2, \quad (\text{A.8})$$

where $y(x_i)$ is the number of counts in channel x_i and $\Delta y(x_i)$ is the uncertainty in $y(x_i)$.

The χ^2 was minimized by varying the parameters A , B , C , D , l_j , f_j , σ and μ using the Levenberg-Marquardt routine [81].

BIBLIOGRAPHY

1. W. Heisenberg. *Z. Phys.*, 77:1, (1932).
2. G. Breit, E. U. Condon, and R. D. Present. Theory of scattering of protons by protons. *Phys. Rev.*, 50:825–845, (1936).
3. G. Breit and E. Feenberg. The possibility of the same form of specific interaction for all nuclear particles. *Phys. Rev.*, 50:850–856, (1936).
4. E. P. Wigner. In *Proceedings of the Robert A. Welch Conferences on Chemical Research, Houston*, volume 1, page 67. Robert A. Welch Foundation, Houston, Texas, (1957).
5. S. Weinberg and S. B. Treiman. Electromagnetic corrections to isotopic spin conservation. *Phys. Rev.*, 116:465–468, (1959).
6. J. J. Sakurai. *Modern quantum mechanics*, page 239. Addison-Wesley, revised edition, 1994.
7. G. T. Garvey. Nuclear mass relations. *Annu. Rev. Nucl. Sci.*, 19:433–470, 1969.
8. E. M. Henley and C. E. Lacy. Simple model for corrections to the isobaric multiplet mass equation. *Phys. Rev.*, 184:1228–1229, (1969).
9. G. Bertsch and S. Kahana. T_z^3 term in the isobaric multiplet equation. *Phys. Lett*, B33:193–194, (1970).
10. W. Benenson and E. Kashy. Isobaric quartets in nuclei. *Rev. Mod. Phys.*, 51:527–540, (1979).
11. J. Britz, A. Pape, and M. S. Antony. Coefficients of the isobaric mass equation and their correlations with various nuclear parameters. *Atomic Data and Nuclear Data Tables*, 69:125–159, (1998).
12. W. E. Ormand. Mapping the proton drip line up to $A = 70$. *Phys. Rev. C*, 55:2407–2417, (1997).

13. I. S. Towner and J. C. Hardy. Calculated corrections to superallowed Fermi β decay: New evaluation of the nuclear-structure-dependent terms. *Phys. Rev. C*, 66:035501, (2002).
14. E. G. Adelberger, C. Ortiz, A. García, H. E. Swanson, M. Beck, O. Tengblad, M. J. G. Borge, I. Martel, H. Bichsel, and the ISOLDE Collaboration. Positron-neutrino correlation in the $0^+ \rightarrow 0^+$ decay of ^{32}Ar . *Phys. Rev. Lett.*, 83:1299–1302, 1999.
15. F. Herfurth, J. Dilling, A. Kellerbauer, G. Audi, D. Beck, G. Bollen, H.-J. Kluge, D. Lunney, R. B. Moore, C. Scheidenberger, S. Schwarz, G. Sikler, J. Szerypo, and ISOLDE Collaboration. Breakdown of the isobaric multiplet mass equation at $A = 33$, $T = 3/2$. *Phys. Rev. Lett.*, 87:142501, (2001).
16. M. C. Pyle, A. García, E. Tatar, J. Cox, B. K. Nayak, S. Triambak, B. Laughman, A. Komives, L. O. Lamm, J. E. Rolon, T. Finnessy, L. D. Knutson, and P. A. Voytas. Revalidation of the isobaric multiplet mass equation. *Phys. Rev. Lett.*, 88:122501, 2002.
17. S. Triambak, A. García, D. Melconian, M. Mella, and O. Biesel. Excitation energies in ^{33}Cl via $^{32}\text{S}(p, \gamma)$. *Phys. Rev. C*, 74:054306, 2006.
18. K. Blaum, G. Audi, D. Beck, G. Bollen, F. Herfurth, A. Kellerbauer, H.-J. Kluge, E. Sauvan, and S. Schwarz. Masses of ^{32}Ar and ^{33}Ar for fundamental tests. *Phys. Rev. Lett.*, 91:260801, 2003.
19. J. F. Wilkerson, T. M. Mooney, R. E. Fauber, T. B. Clegg, H. J. Karwowski, E. J. Ludwig, and W. J. Thompson. Isospin-nonconserving particle decays in light nuclei. *Nucl. Phys. A*, 549:223–253, 1992.
20. M. S. Antony, A. Huck, G. Klotz, A. Knipper, C. Miehé, and G. Walter. Mass measurements of the first $T = 2$ state in ^{32}S and ^{32}Si . In *Proceedings of the International Conference on Nuclear Physics, Berkeley, 1980*, volume 1, page 134. Lawrence Berkeley Laboratory, Berkeley, CA, (1980).
21. J. Vernotte, S. Gales, M. Langevin, and J. M. Maison. Investigation of the lowest $T = 2$ state of ^{32}S in the $^{31}\text{P} + p$ reactions. *Phys. Rev. C*, 8:178–187, 1973.
22. P. M Endt. Supplement to energy levels of $A = 21 - 44$ nuclei (VII). *Nucl. Phys. A*, 633:1–220, 1998.
23. <http://www.srim.org>.

24. P. M. Endt, C. Alderliesten, F. Zijderhand, A. A. Wolters, and A. G. M. Van Hees. Spectroscopic information on ^{24}Mg and ^{28}Si from proton capture. *Nucl. Phys. A*, 510:209–243, 1990.
25. W. Ratynski and F. Käppeler. Neutron capture cross section of ^{197}Au : A standard for stellar nucleosynthesis. *Phys. Rev. C*, 37:595–604, 1988.
26. B. Krusche, K. P. Lieb, H. Daniel, T. Von Egidy, G. Barreau, H. G. Börner, R. Brissot, C. Hofmeyr, and R. Rascher. Gamma ray energies and ^{36}Cl level scheme from the reaction $^{35}\text{Cl}(n, \gamma)$. *Nucl. Phys. A*, 386:245–268, 1982.
27. R. G. Helmer, J. E. Cline, and R. C. Greenwood. *The electromagnetic interaction in Nuclear Spectroscopy*, page 775. North-Holland Publishing Company, 1975.
28. Takeo Katou. Precise measurement of relative intensities of gamma-rays from ^{56}Co . *Nucl. Instrum. Methods*, 124:257–263, 1975.
29. J. Sempau, E. Acosta, J. Baro, J. M. Fernández-Varea, and F. Salvat. An algorithm for Monte Carlo simulation of coupled electron-photon transport. *Nucl. Instrum. and Methods. in Phys. Res. Section B*, 132:377–390, 1997.
30. R. G. Helmer, R. J. Gehrke, and R. C. Greenwood. Peak position variation with source geometry in Ge(Li) detector spectra. *Nucl. Instrum. and Methods*, 123:51–59, 1975.
31. M. Babilon, T. Hartmann, P. Mohr, K. Vogt, S. Volz, and A. Zilges. Dipole and electric quadrupole excitations in ^{32}S up to 9.9 MeV. *Phys. Rev. C*, 65:037303, 2002.
32. <http://www.nndc.bnl.gov>.
33. P. M. Endt. Energy levels of $A = 21-44$ nuclei (VII). *Nucl. Phys. A*, 521:1–400, 1990.
34. E. K. Warburton and J. Weneser. *Isospin in nuclear Physics (edited by D. H. Wilkinson)*, page 173. North-Holland publishing company, 1969.
35. K. A. Snover. *The study of high isospin states by isospin forbidden radiative capture reactions*. PhD thesis, Stanford University, 1969.
36. G. Audi, A. H. Wapstra, and C. Thibault. The AME2003 atomic mass evaluation (II): Tables, graphs and references. *Nucl. Phys. A*, 729:337–676, 2003.
37. A. Paul, S. Röttger, A. Zimbal, and U. Keyser. Prompt (n, γ) mass measurements for the AVOGADRO project. *Hyperfine Interactions*, 132:189–194, 2001.

38. S. Röttger, A. Paul, and U. Keyser. Prompt (n, γ) -spectrometry for the isotopic analysis of silicon crystals for the Avogadro project. *IEEE Transactions on Instrumentation and Measurement*, 46:560–562, 1997.
39. E. D. Commins and P. H. Bucksbaum. *Weak interactions of leptons and quarks*, page 33. Cambridge University Press, 1983.
40. Nicola Cabibbo. Unitary symmetry and leptonic decays. *Phys. Rev. Lett.*, 10:531–533, 1963.
41. M. Kobayashi and T. Maskawa. CP-violation in the renormalizable theory of weak interaction. *Prog. Theor. Phys.*, 49:652–657, 1973.
42. W.-M Yao *et al.* Review of particle physics. *Journal of Physics G*, 33:138–143, 2006.
43. M. A. B. Bég, R. V. Budny, R. Mohapatra, and A. Sirlin. Manifest left-right symmetry and its experimental consequences. *Phys. Rev. Lett.*, 38:1252–1255, 1977.
44. W. J. Marciano and A. Sirlin. Radiative corrections to β decay and the possibility of a fourth generation. *Phys. Rev. Lett.*, 56:22–25, 1986.
45. Paul Langacker and David London. Mixing between ordinary and exotic fermions. *Phys. Rev. D*, 38:886–906, 1988.
46. E. Hagberg, J. C. Hardy, V. T. Koslowsky, G. Savard, and I. S. Towner. Degree to which CVC is established through beta decay alone. nucl-ex/9609002, 1996.
47. J. C. Hardy. CVC tests and CKM unitarity. *Nucl. Phys. A*, 752:101–108, 2005.
48. R. P. Feynman and M. Gell-Mann. Theory of the Fermi interaction. *Phys. Rev.*, 109:193–198, 1958.
49. S. S. Gershtein and Ia. B. Zel’dovich. *JETP (USSR)*, 29:698, 1955.
50. I. S. Towner and J. C. Hardy. Calculated corrections to superallowed Fermi β decay: New evaluation of the nuclear-structure-dependent terms. *Phys. Rev. C*, 66:035501, 2002.
51. W. E. Ormand and B. A. Brown. Isospin-mixing corrections for fp-shell Fermi transitions. *Phys. Rev. C*, 52:2455–2460, 1995.
52. H. Sagawa, Nguyen Van Giai, and Toshio Suzuki. Effect of isospin mixing on superallowed Fermi β decay. *Phys. Rev. C*, 53:2163–2170, 1996.

53. P. Navrátil, B. R. Barrett, and W. E. Ormand. Large-basis shell-model calculation of the $^{10}\text{C} \rightarrow ^{10}\text{B}$ Fermi matrix element. *Phys. Rev. C*, 56:2542–2548, 1997.
54. A. Sirlin. General properties of the electromagnetic corrections to the beta decay of a physical nucleon. *Phys. Rev.*, 164:1767–1775, 1967.
55. J. C. Hardy and I. S. Towner. Superallowed $0^+ \rightarrow 0^+$ nuclear β decays: A critical survey with tests of the conserved vector current hypothesis and the standard model. *Phys. Rev. C*, 71:055501, 2005.
56. A. deShalit and H. Feshbach. *Theoretical Nuclear Physics Volume I*, page 853. John Wiley & Sons, 1974.
57. H. Abele, M. Astruc Hoffmann, S. Baeßler, D. Dubbers, F. Glück, U. Müller, V. Nesvizhevsky, J. Reich, and O. Zimmer. Is the unitarity of the quark-mixing CKM matrix violated in neutron β -decay? *Phys. Rev. Lett.*, 88:211801, 2002.
58. D. Počanić, E. Frlež, V. A. Baranov, W. Bertl, Ch. Brönnimann, M. Bychkov, J. F. Crawford, M. Daum, N. V. Khomutov, A. S. Korenchenko, S. M. Korenchenko, T. Kozłowski, N. P. Kravchuk, N. A. Kuchinsky, W. Li, R. C. Minehart, D. Mzhavia, B. G. Ritchie, S. Ritt, A. M. Rozhdestvensky, V. V. Sidorkin, L. C. Smith, I. Supek, Z. Tsamalaidze, B. A. VanDevender, Y. Wang, and H.-P. Wirtz. Precise measurement of the $\pi^+ \rightarrow \pi^0 e^+ \nu$ branching ratio. *Phys. Rev. Lett.*, 93:181803, 2004.
59. William J. Marciano and Alberto Sirlin. Improved calculation of electroweak radiative corrections and the value of V_{ud} . *Phys. Rev. Lett.*, 96:032002, 2006.
60. J. C. Hardy and I. S. Towner. New limits on fundamental weak-interaction parameters from superallowed β decay. *Phys. Rev. Lett.*, 94:092502, 2005.
61. A. Sher, R. Appel, G. S. Atoyan, B. Bassalleck, D. R. Bergman, N. Cheung, S. Dhawan, H. Do, J. Egger, S. Eilerts, H. Fischer, W. Herold, V. V. Issakov, H. Kaspar, D. E. Kraus, D. M. Lazarus, P. Lichard, J. Lowe, J. Lozano, H. Ma, W. Majid, S. Pislak, A. A. Poblaguev, P. Rehak, Aleksey Sher, J. A. Thompson, and P. Truöl. High statistics measurement of the $K^+ \rightarrow \pi^0 e^+ \nu$ (K_{e3}^+) branching ratio. *Phys. Rev. Lett.*, 91:261802, 2003.
62. T. Alexopoulos, M. Arenton, R. F. Barbosa, A. R. Barker, L. Bellantoni, A. Bellavance, E. Blucher, G. J. Bock, E. Cheu, S. Childress, R. Coleman, M. D. Corcoran, B. Cox, A. R. Erwin, R. Ford, A. Glazov, A. Golossanov, J. Graham, J. Hamm, K. Hanagaki, Y. B. Hsiung, H. Huang, V. Jejer, D. A. Jensen, R. Kessler, H. G. E. Kobrak, and K. Kotera. A determination of the Cabibbo-Kobayashi-Maskawa parameter $|V_{us}|$ using K_L decays. *Phys. Rev. Lett.*, 93:181802, 2004.

63. G. Savard, F. Buchinger, J. A. Clark, J. E. Crawford, S. Gulick, J. C. Hardy, A. A. Hecht, J. K. P. Lee, A. F. Levand, N. D. Scielzo, H. Sharma, K. S. Sharma, I. Tanihata, A. C. C. Villari, and Y. Wang. Q value of the superallowed decay of ^{46}V and its influence on V_{ud} and the unitarity of the Cabibbo-Kobayashi-Maskawa matrix. *Phys. Rev. Lett.*, 95:102501, 2005.
64. B. A. Brown. Private communication.
65. A. García *et. al.* Positron-neutrino correlations in ^{32}Ar and ^{33}Ar decays. In preparation.
66. C. Détraz, C. S. Zaidins, D. J. Frantsvog, R. L. Wilson, and A. R. Kunselman. Beta-decay of ^{32}Cl and ^{40}Sc . *Nucl. Phys. A*, 203:414–420, 1973.
67. R. E. Tribble, R. H. Burch, and C. A. Gagliardi. MARS: A Momentum Achromat Recoil Spectrometer. *Nucl. Instrum. and Meth. in Phys. Res. A*, 285:441–446, 1989.
68. L. Trache. Private communication.
69. R. E. Tribble, A. Azhari, C. A. Gagliardi, J. C. Hardy, A. Mukhamedzhanov, X. Tang, L. Trache, and S. J. Yennello. Radioactive beams at Texas A&M University. *Nucl. Phys. A*, 701:278–281, 2002.
70. J. C. Hardy. Private communication.
71. Anthony J. Armini, Jules W. Sunier, and J. Reginald Richardson. Masses and decay of Al^{24} , P^{28} , Cl^{32} , Sc^{40} , and their $T_z = 0$ analog states. *Phys. Rev.*, 165:1194–1202, 1968.
72. B. M. Sherrill, D. J. Morrissey, J. A. Nolen, and J. A. Winger. The A1200 projectile fragment separator. *Nucl. Instrum. and Meth. in Phys. Res. B*, 56:1106–1110, 1991.
73. G. Duchêne, F. A. Beck, P. J. Twin, G. de France, D. Curienea, L. Han, C. W. Beausang, M. A. Bentley, P. J. Nolan, and J. Simpson. The Clover: a new generation of composite Ge detectors. *Nucl. Instrum. and Meth. in Phys. Res. A*, 432:90–110, 1999.
74. O. B. Tarasov and D. Bazin. LISE++: design your own spectrometer. *Nucl. Phys. A*, 746:411–414, 2004.
75. D. Melconian. Private communication.
76. F. C. Barker. 2^+ states of ^8Be . *Aust. J. Phys.*, 22:293–316, 1969.

77. T. Björnstad, M. J. G. Borge, P. Dessagne, R.-D. Von Dincklage, G. T. Ewan, P. G. Hansen, A. Huck, B. Jonson, G. Klotz, and A. Knipper *et al.* Study of the giant Gamow-Teller resonance in nuclear β decay: The case of ^{32}Ar . *Nucl. Phys. A*, 443:283–301, 1985.
78. I. S. Towner. Private communication.
79. S. Triambak, A. García, E. G. Adelberger, G. J. P. Hodges, D. Melconian, H. E. Swanson, S. A. Hoedl, S. K. L. Sjue, A. L. Sallaska, and H. Iwamoto. Mass of the lowest $T = 2$ state in ^{32}S : A test of the isobaric multiplet mass equation. *Phys. Rev. C*, 73:054313, 2006.
80. B. A. Brown and B. H. Wildenthal. Status of the nuclear shell model. *Annual Review of Nuclear and Particle Science.*, 38:29–66, 1988.
81. W. H. Press, B. P. Flannery, S. A. Teukolsky, and W. T. Vetterling. *Numerical recipes in fortran 77: The art of scientific computing*, page 678. Cambridge University Press, second edition, 1999.